Institut für Theoretische Physik
Fakultät Mathematik und Naturwissenschaften
Technische Universität Dresden

Spectroscopy of Discrete Breathers

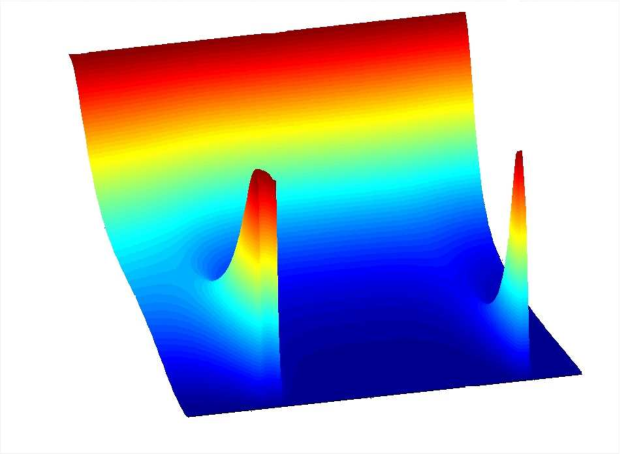

Dissertation
zur Erlangung des
Doktorgrades der Naturwissenschaften
(Doctor rerum naturalium)

vorgelegt von
Andrey Miroshnichenko
geboren am 5 November 1977 in Twer

Dresden 2003

To my wife Natalia and two sons Nikola and Danila

Eingereicht am 2 Juli 2003

1. Gutachter: Prof. Peter Fulde
2. Gutachter: Dr. Serge Aubry
3. Gutachter: Prof. Luis Mario Floria

Verteidigt am ______________________

Abstract

The interaction of small amplitude linear waves with nonlinear spatial localized and time-periodic excitations *discrete breathers* (DBs) is studied by means of spectroscopic methods.

In Hamiltonian systems, where linear waves can freely propagate through the system, the scattering problem is studied. Due to the time periodicity DBs generate *time-periodic* scattering potentials. The anharmonicity of DBs gives rise to the existence of higher harmonics. Each harmonic generates a scattering channel which could be *open* or *closed*. Closed channels are active only in the core of DBs, therefore, locally several channels can be active simultaneously. It leads to the possibility of interference phenomena. One of them is the *perfect reflection* of waves by DBs. This phenomenon is of a resonant nature and is similar to the Fano resonance in atomic systems.

Based on the experimental observations of various types of DBs in Josephson junction ladders, the interaction of DBs with plasmons is studied by means of resonances. Due to the presence of dissipation DBs can survive them. It gives us the possibility to study the medium, where DB is excited, by varying the DB in a controled way and using these resonances. Numerically resonances are monitored by jumps in the current-voltage characteristics and by the power of ac librations at the edge, while in the experiments only the first method is used. Both results are in a very good agreement.

Contents

II Inverse spectroscopy 53

List of abbreviations

DB - Discrete Breather
DNLS - Discrete NonLinear Schroedinger (equation)
EE - Electromagnetic Excitation
EW - Electromagnetic Wave
FPU - Fermi-Pasta-Ulam (system)
FT - Fourier Transformation
HWS - Homogeneous Whirling State
ILM - Intrinsic Localized Mode
JJA - Josephson Junction Array
JJL - Josephson Junction Ladder
RB - Rotobreather
SJJ - Single Josephson Junction

Introduction

Without sun no light
Without breath no life

The phenomenon of dynamical localization in nonlinear homogeneous lattices has been widely studied during the last decade. The interplay between nonlinearity and discreteness of space gives the possibility for the existence of spatial localized and time periodic excitations - *discrete breathers* (DBs). Discrete breathers are also known under different names - Intrinsic Localized Mode (ILM), Self-localized Anharmonic Mode (SLAM), Nonlinear Localized Excitation (NLE). The nonlinearity induces the frequency dependence of amplitudes of excitations. The discreteness is crucial in order to provide structural stability by preventing resonances between a DB and plane waves. DBs have been mathematically proven to be generic solutions for the dynamics of nonlinear coupled oscillators for any lattice dimension. In phase space DBs are *periodic orbits* which, in addition, localize in space. The spatial decay depends on the type of nonlinearity, range of interaction and could be algebraic, exponential or even superexponential.

Initially the concept of DBs was developed for conservative systems. But it can be extended to dissipative systems as well, where DBs become time-periodic spatially localized *attractors*. Spatial localization of DBs is predicted to persist under a spatially homogeneous driving force, which is introduced in order to compensate the dissipative losses.

DBs have been also observed experimentally in diverse systems such as coupled optical wave guides, low-dimensional crystals, anti-ferromagnetic materials, in photonic crystals with a nonlinear Kerr medium, networks of small Josephson junctions, micromechanical oscillator arrays and in biomolecules.

By definition a DB is a stationary state. But moving breather-like states have been observed numerically in different systems. They are not time-periodic anymore and the existence of moving DBs as exact solutions is still an open question. But there is one special case, where moving DBs are *exact* solutions. This is the Ablowitz-Ladik lattice, which is an integrable system.

Another interesting question is the localization of energy in quantum systems. If the Hamiltonian of a given system is invariant under spatial translations then all eigenstates are spatially *delocalized*. It means that such a quantum system does not allow for spatially localized states. But still there is a possibility for quantum analogues of classical DBs by taking many-phonon bound states which *tunnel* from site to site. Then in the classical limit the tunnelling rate will just vanish and a DB will be pinned at a certain site.

There are mathematical and numerical tools which allow to prove and find DBs in concrete systems and then check their stability. These tools are well developed due to some special properties of different systems. But, usually, in experiments it is impossible to resolve both the full dynamics and space structure. Thus, there is need to construct theoretical methods which can be used by experimentalists and are useful in order to determine the existence of DBs in the systems and examine their properties. Spatial localization allows to use spectroscopic methods. By spectroscopy we mean the interaction of DBs with plane waves. Moreover, plane waves can be easily generated and registered in experiments.

This work is devoted to the study of main properties of interaction between DBs and extended states. The first part is devoted to 1D Hamiltonian systems. The extended states are small amplitude linear waves, which can freely propagate in such systems. Thus we will consider the problem of interaction of localized and delocalized states in the framework of *transport spectroscopy* by sending the plane wave onto a DB. Due to the smallness of the amplitude of extended states this problem can be considered as a scattering problem, taking the DB as a scattering potential. We need to compute transmission and reflection coefficients. Due to their localization DBs usually generate *local* modes with the frequencies outside of the phonon bands. By changing the breather itself it is possible to vary these frequencies. For some cases *perfect transmission* was observed. But *perfect reflection* was observed as well. This is a characteristic property of time-dependent scattering potentials . It is similar to the Fano resonance in atomic systems. In this work the scattering process is considered for different types of DBs (optical and acoustic) in different Hamiltonian systems using an improved numerical scheme.

In the second part DBs in dissipative systems such as Josephson junction ladders (JJLs) are studied. Due to the presence of dissipation there are no freely propagating extended states in this system. By varying the control parameter (dc bias) the frequency of DB can match the plasmon spectrum and different types of resonances occur. Again due to the presence of dissipation not all resonances lead to the destruction of the DB (as in the Hamiltonian case), but to the excitation of librations in the DB tails. It gives the possibility to use an *inverse spectroscopy* method, which also allows to study the interaction between localized and delocalized states. It is possible to monitor this delocalization by measuring the power of ac libration at the edge of the ladder. The analysis of the peaks of the power of ac libration shows, that they correspond exactly to the *cavity* modes of the ladder. When the resonances become stronger and instabilities occur, the DB can switch to other states such as a resonant DB, the Homogeneous Whirling State (HWS) or the superconducting one. All of them are time periodic. By using the Floquet theory we found that such instabilities occur due to resonances between a DB and plasmons. In some special cases DBs can switch to *incommensurate* quasi-periodic states. These cases were studied separately numerically and experimentally and the results are in a very good agreement.

Any abbreviation in this these can be found in the List of Abbreviations.

1 Review of discrete breathers

Discreteness appears in systems of interacting 'objects', which are separated in space. In crystals these 'objects' are atoms with the distance between them about 7 Å, in photonic crystals the 'objects' are waveguides which are equally placed in space with the distance between them about $10\mu m$, in a network of Josephson junctions each junction is an 'object' and the characteristic linear scale between them is $\approx 50\mu m$, in a mechanical system of pendulums each of them can be considered as an 'object' and a characteristic distance could be order of 10 cm. The discreteness causes a cut-off of frequency (energy) spectrum. If, in addition to discreteness, the system is nonlinear there is a possibility to excite time periodic and spatially localized states - discrete breathers (DBs). They have been observed numerically and experimentally in a variety of systems.

In this chapter the key ideas on DBs and their applications are described.

1.1 Basic properties

1.1.1 Definitions

In order to describe the main properties of DBs a chain of coupled oscillators is used. The dynamics of such systems is characterized by time-dependent coordinates $x_n(t)$, where n numerates each particle. The Hamiltonian can be written in general form as

$$\mathrm{H} = \sum_n \left(\frac{\dot{x}_n^2}{2} + V[x_n] + W[x_n - x_{n-1}] \right) \quad . \tag{1.1}$$

Here $V[x]$ is an optional on-site (substrate) potential, which acts uniformly for each particle, and $W[x]$ is the nearest neighbor interaction. The equations of motion become

$$\ddot{x}_n = -W'[x_n - x_{n-1}] + W'[x_{n+1} - x_n] - V'[x_n] \quad . \tag{1.2}$$

Without loss of generality the following assumptions can be used: $V[0] = W[0] = V'[0] = W'[0] = 0$ and $V''[0] \geq 0$, $W''[0] > 0$ in order to satisfy the positive definiteness of the Hamiltonian. The ground state of the system (1.2) is $x_n(t) \equiv 0$ for all n.

This Hamiltonian supports the excitation of small amplitude linear waves. In order to find the frequency spectrum of such excitations, equations (1.2) should be linearized around the ground state

$$\ddot{\xi}_n(t) = W''(0)(\xi_{n-1} - 2\xi_n + \xi_{n+1}) - V''(0)\xi_n \tag{1.3}$$

and the ansatz for the plane wave $\xi_n(t) = A\mathrm{e}^{i(qn-\omega_q t)}$ gives the *dispersion relation*

$$\omega_q^2 = V''[0] + 4W''[0]\sin^2\left(\frac{q}{2}\right) \quad , \tag{1.4}$$

with q being the wave number.

The spectrum is bounded from below and from above. It is an important property of any discrete system. It means that only the waves with frequencies from some interval, which is determined by Eq. (1.4) can freely propagate through the system. Waves with frequencies outside of this interval will decay in space. The second note is that the frequency ω_q is symmetric and periodic in q. So it is enough to consider the range $q \in [0, \pi]$. When $V''(0) = 0$ the spectrum is gapless and is called *acoustic*, the value $\omega_q(0) = 0$ belongs to the spectrum. In the opposite case there is a gap between two branches $\omega_q^{\pm}$ and the spectrum is called *optical*.

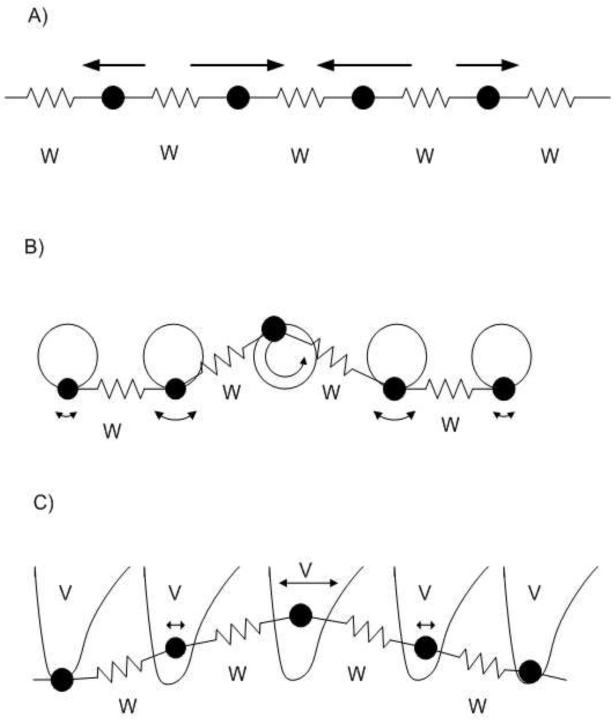

Figure 1.1: A schematic representation of different types of discrete breathers: a) acoustic breather; b) acoustic rotobreather; c) optical breather.

The competition between nonlinearity and discreteness in (1.2) can lead to the appearance of spatially localized time-periodic states: *discrete breathers* (DBs). Due to the nonlinearity the frequency of excitations depends on their amplitude and the discreteness leads to the existence of an upper bound of the phonon band. That is why spatially localized and time periodic states are not so common in continuous systems. Their unbounded spectrum leads to resonances of a localized state with phonons.

It was shown that DBs exist for different types of potentials $V[x]$ and $W[x]$, although at least one of the two functions ($V[x]$ and/or $W[x]$) has to be anharmonic.

DB solutions are characterized by being time-periodic $\hat{x}_n(t+T_b) = \hat{x}_n(t)$ and spatially localized $\hat{x}_{|n|\to\infty} \to 0$ (except one-dimensional systems with $V = 0$ where $\hat{x}_{n\to\pm\infty} \to \pm c$ with $c \geq 0$). If the Hamiltonian H is invariant under a finite translation (rotation) of any $x_n \to x_n + \lambda$, then discrete *rotobreathers* (RBs) may exist [110]. These excitations are characterized by one or several sites in the breather center evolving in a rotational state $\hat{x}_0(t+T_b) = \hat{x}_0(t) + \lambda$, while outside this center the lattice is governed again by time periodic spatially localized oscillations. Due to time periodicity the breather state can be expanded into a Fourier series

$$\hat{x}_n(t) = \sum_k A_{nk} \mathrm{e}^{ik\Omega_b t} \ . \tag{1.5}$$

DBs are represented by a closed path in the phase space. Each breather is characterized by its frequency $\Omega_b = 2\pi/T_b$. By varying the frequency one obtains families of breathers in the phase space. But breathers exist not for any frequency Ω_b. The necessary condition of existence is $k\Omega_b \neq \omega_q$ for all nonzero integers k. Due to the upper bound of the spectrum (1.4), breathers can exist, generally, for $\Omega_b > \omega_q$. The case of an acoustic spectrum is also interesting, because for any Ω_b there is $k = 0$, which fulfills the condition $k\Omega_b = \omega_q(0)$. But if the Hamiltonian is invariant under the parity transformation $x_n \to -x_n$, then the breather can be also invariant under this transformation. Therefore $A_{nk} \equiv 0$ for all even k, including $k = 0$ and this resonance does not manifest itself.

As ω_q^2 is an analytic function of q, DBs are exponentially localized on the lattice, but in general DBs can possess others spatial localization extension [42]. It was shown that a spatial localized state with time dependence, in general, should be periodic in time [43]. Indeed, consider the simple case of a state with two incommensurate frequencies Ω_1 and Ω_2. It can be expanded into a double Fourier series

$$\tilde{x}_n(t) = \sum_{k_1,k_2} A_{nk_1k_2} \mathrm{e}^{ik_1\Omega_1 t + ik_2\Omega_2 t} \, . \tag{1.6}$$

For this state the resonance condition is $k_1\Omega_1 + k_2\Omega_2 = \omega_q$. Following Ref. [31] one can conclude that for any incommensurate frequencies Ω_1 and Ω_2 there are always k_1 and k_2 such that the resonant condition is fulfilled and thus, it is impossible to construct a quasi-periodic in time and spatially localized state.

1.1.2 Proof of existence

For some potentials the existence of breathers can be proved analytically [77, 32, 8, 76, 5, 62].

The first approach is based on the *anticontinuous* limit [77]. It can be used when the interaction potential $W(y)$ is parameterized as $W(y) = \epsilon\Psi(y)$. For the case $\epsilon = 0$, the equations of motion are decoupled in space and each oscillator moves in its anharmonic potential $V(x) \neq 0$. Now it is possible to choose one (or several) oscillator(s) moving with the frequency Ω while the others are at rest. Then it is possible to find a periodic orbit of the lattice with $\epsilon \neq 0$ but close to zero such that the new periodic solution will have the same frequency Ω and will be close to the initial periodic orbit at $\epsilon = 0$. These periodic orbits will be exponentially localized in space and are thus discrete breathers.

The main idea is to find the zeros of an operator $\mathbf{F}(x;\epsilon) = (\ldots, F_1(x;\epsilon), F_2(x;\epsilon), \ldots)$, where

$$F_n(x;\epsilon) = \ddot{x}_n + \frac{\partial H(\epsilon)}{\partial x_n} \, . \tag{1.7}$$

The continuation for nonzero ϵ can be done by using the implicit function theorem for $\mathbf{F}(x(\epsilon);\epsilon) = 0$. This method is quite general and can be used for lattices of any dimension and numbers of sites.

This approach gives a key idea how to find numerically and even experimentally breathers in such systems. First, (if it is possible) switch off the coupling, excite several sites and then switch the coupling adiabatically on. Numerically it can be done by means of the Newton method (see Appendix A).

A modification of this method was used in order to prove the existence of discrete breathers in diatomic FPU chains with light and heavy masses [76]. As a small parameter the mass ratio was used. On the basis of the center manifold reduction [61], which does not use the concept of the anti-continuous limit, it was proven that discrete breathers exist in a diatomic FPU chain for arbitrary mass ratios [62].

As was shown in [32], it is possible to separate the time and space dependence in homogeneous FPU chains. It was proven that a discrete map for spacial amplitudes possesses a homoclinic orbit. Together with the periodicity of the time variable it constitutes a proof of existence of DBs in such systems.

A variational approach was applied for optical and acoustic systems in order to prove the existence of *hard* breathers with frequencies above the phonon band [5]. DBs are considered as loops in the phase space which maximize a certain average energy function for a fixed pseudoaction appropriately defined.

1.1.3 Stability of breathers

To study the stability of a DB the equations of motion (1.2) should be linearized around a breather solution $x_n(t) = \hat{x}_n(t) + \epsilon_n(t)$:

$$\begin{aligned} \ddot{\epsilon}_n \;&=\; -W''[\hat{x}_n(t) - \hat{x}_{n-1}(t)](\epsilon_n - \epsilon_{n-1}) \\ &\quad +W''[\hat{x}_{n+1}(t) - \hat{x}_n(t)](\epsilon_{n+1} - \epsilon_n) - V''[\hat{x}_n(t)]\epsilon_n \, . \end{aligned} \tag{1.8}$$

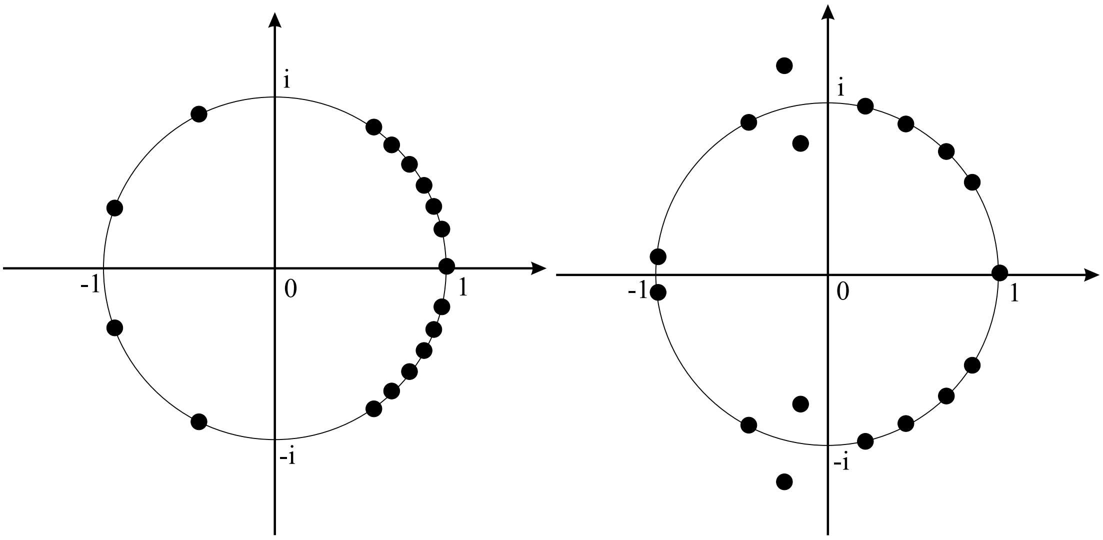

Figure 1.2: The schematic views of the positions of Floquet multipliers for a Hamiltonian system for two different values of a control parameter.
(Left): The generic situation is shown when there are some localized states.
(Right): The instability occurs by collision between the localized and delocalized eigenvalues. Note that there are always two eigenvalues at +1.

This is a set of coupled linear differential equations with time periodic coefficients of period T_b. Note that these coefficients are determined by the given DB solution $\hat{x}_n(t)$.

Eq. (1.8) determines the linear stability of the breather through the spectral properties of the Floquet matrix,[82, 84, 42, 19] which is given by a map over one breather period

$$\begin{pmatrix} \vec{\epsilon}(T_b) \\ \dot{\vec{\epsilon}}(T_b) \end{pmatrix} = \mathbf{F} \begin{pmatrix} \vec{\epsilon}(0) \\ \dot{\vec{\epsilon}}(0) \end{pmatrix} , \tag{1.9}$$

where $\vec{\epsilon} \equiv (..., \epsilon_{n-1}, \epsilon_n, \epsilon_{n+1}, ...)$. For marginally stable breathers all eigenvalues of the symplectic matrix $\mathbf{F}$ will be located on the unit circle and can be written as $e^{i\theta}$. The corresponding eigenvectors are the solutions of Eq.(1.8), and fulfill the Bloch condition

$$\epsilon_n(t + T_b) = e^{-i\theta}\epsilon_n(t) . \tag{1.10}$$

Because the DB solution is exponentially localized on the lattice, equation (1.8) will reduce to the usual small amplitude wave equation far away from the breather center. Thus, only a finite number of Floquet eigenvectors are spatially localized, while an infinite number of them (for an infinite lattice) are delocalized and these solutions correspond to plane waves with the spectrum (1.4) and the Floquet phases $\theta = \pm\omega_q T_b$. The remaining Floquet eigenvalues correspond to local Floquet eigenvectors and are separated from the plane wave spectrum on the unit circle. Note here, that two eigenvectors with the degenerated eigenvalue $e^{i\theta} = +1$ always exist and correspond to the perturbations tangent to the breather family of solutions (see Fig. 1.2(left)). By changing some control parameter of the system (1.2), Floquet multipliers will move on the unit circle and, therefore, can cross each other. It leads to possible collisions of them and subsequent resonances. As a result a DB will loose its stability. There are several typical scenarios of instability. One takes place when eigenvalues collide on the real axis at ±1, i.e. when one of the Floquet multipliers meets its complex conjugate partner. It can written as $\theta = n\pi$, where $n \subset \mathbb{N}$ or

$$\omega_q/\Omega_b = n/2 , \qquad n = 1, 2, 3, \ldots . \tag{1.11}$$

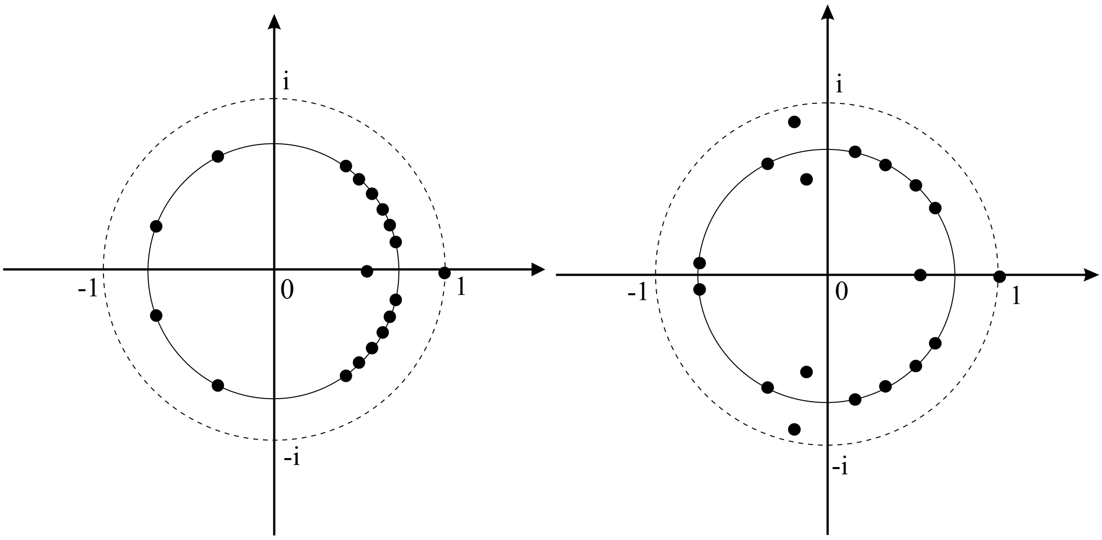

Figure 1.3: The same situation as on Fig. 1.2 but for a dissipative system. Even in the case of a collision between two eigenvalues the instability will not take place as long as one of the eigenvalues does not cross the unit circle.

Even n's correspond to collisions at $+1$ and odd n's to collisions at -1. The case of even n may lead to the disappearing of the breather as a solution and the odd one to the period doubling bifurcation, when the breather can still exist but becomes dynamically unstable.

Another possibility is to have a collision somewhere on the unit circle. In this case more Floquet eigenvalues take part in the collision. But not any two multipliers will collide. It was shown that they should have the same *Krein signatures* [2, 3, 83].

1.1.4 Dissipative systems

DBs exist not only in Hamiltonian systems, but in systems with dissipation and homogeneous bias as well [105]. The bias could be constant (dc bias) or periodic in time (ac bias). In terms of the phase space it means that after introducing a dissipation some periodic orbits (DBs) will be destroyed and others will become attractors. A DB in these systems retains all its properties such as exponential localization and linear stability. The Floquet eigenvalues lie not on the unit circle but inside on a circle with a smaller diameter, which is determined by the dissipation strength. It means that not all collisions of Floquet eigenvalues lead to the instability of the DB. If the collision is weak, eigenvalues can just deviate from the internal circle and return to it without crossing the unit circle (see Fig. 1.3). It gives a possibility to study the resonances between DBs and phonons in a different way and will be considered in part II of this work for a network of Josephson junctions.

1.2 Experimental observations

There are many recent experiments on the DB detection in various systems. Here only some of them will be briefly described.

1.2.1 Nonlinear optics

One of the first observations was made on weakly coupled waveguides with length of several mm in the presence of the nonlinear Kerr effect [25, 47]. They are equally positioned in space, which implies a constant coupling between them (see Fig. 1.4 (Left)). Characteristic diameters and distances between waveguides are of order of micrometers.

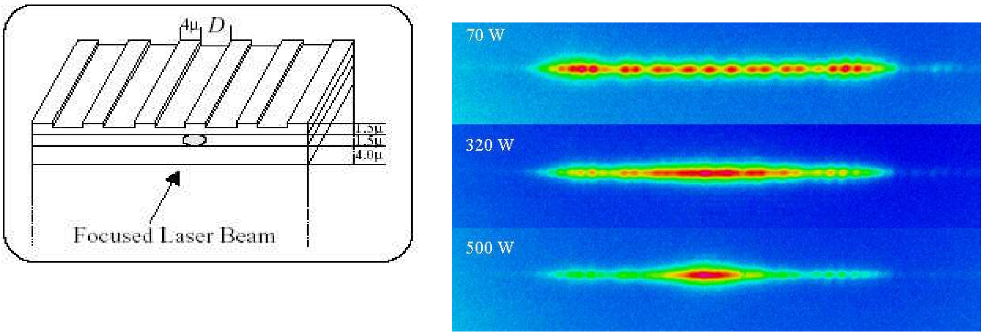

Figure 1.4: (Left): Schematic drawing of coupled waveguides (input facet). (Right): Images of the output facet of a sample for different powers: a) weak power ($70W$) demonstrates linear feature, b) intermediate power ($320W$), the distribution is narrowing, and c) strong power ($500W$), discrete soliton is formed. This is a colored version of the same figure in [25] and has been taken from the web-site of one of the authors.

In this experiment a focused laser beam is injected into the central waveguide on one side and the way how this beam is spreading out among other waveguides during its propagation is observed on the opposite side. The images of outcome are shown in Fig. 1.4 (Right). When the power of the laser beam is rather small and the nonlinearity can be neglected light disperses to the neighboring coupled waveguides and is equally distributed among them ($70W$). By increasing the power, light is localizing around the input waveguide ($320W$) and when sufficient power is injected, a discrete soliton is formed ($500W$).

Due to a band structure a beam can be launched in gaps. By injecting two beams in different gaps it is possible to observe an interference pattern along the propagation direction. As it was shown in Ref. [81], the beams can form an *optical breather* with periodically varying intensity during the propagation which was monitored in an experiment by collecting multiphoton fluorescence (see Fig. 1.5) .

Quite recently, *two-dimensional* discrete solitons were observed in optically induced photonic lattices [24, 46]. This is the first experimental observation of 2D discrete breathers. A 2D array of waveguides is induced in a photosensitive material by interfering two or more plane

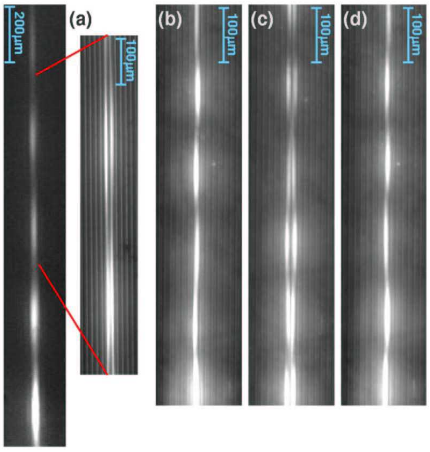

Figure 1.5: Top view of waveguide arrays. In all cases the array period is $11\mu m$. These photographs show the multiphoton fluorescence by the optical breathers along their propagation. Light is injected at the bottom. This figure is taken from [81].

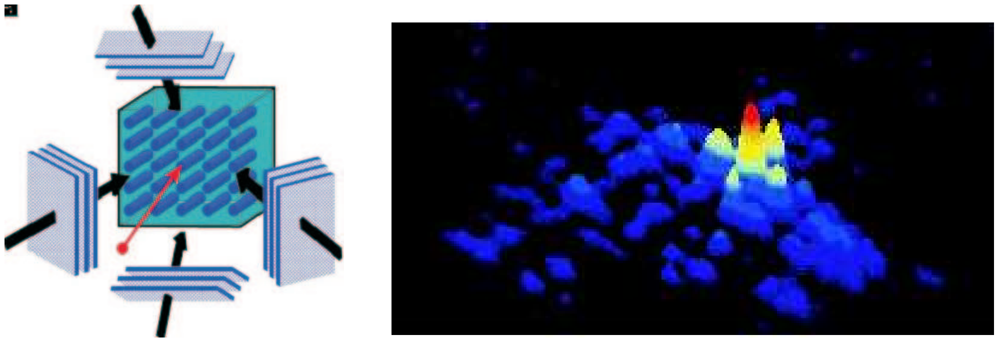

Figure 1.6: (Left): Diagram of the experimental set-up. The photosensitive crystal with electro-optic anisotropy is used (green). Two interfering pairs of ordinarily polarized plane waves (black arrows) induce the photonic array. An additional polarized probe beam (red) is focused into a single waveguide. (Right): Intensity structure of the probe beam at the exit face of a crystal at strong nonlinearity. This figures are taken from [46].

waves. In addition to this, a voltage is applied in order to control the focusing (or defocusing) photorefractive screening nonlinearity. The probe beam is injected into a central waveguide.

The formation of a 2D discrete soliton at high voltage (strong nonlinearity) is observed (see Fig. 1.6 (Right)).

1.2.2 Discrete low-dimensional materials

As another example, the localization of vibrational energy in the halide-bridged transition metal complex PtCl was observed [108].

This material possesses a highly one-dimensional crystal structure. Moreover, very strong coupling between the lattice and the electronic motions provides for large nonlinearity. The experiment was done by means of resonance Raman spectroscopy. The spectra are shown on

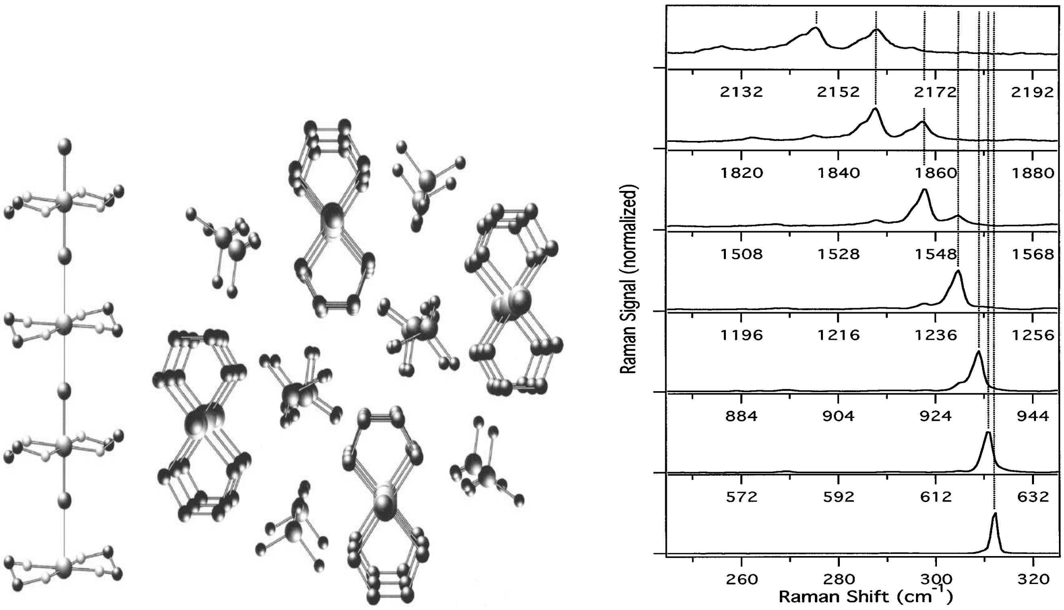

Figure 1.7: (Left): Structure of PtCl crystal. (Right): Raman spectra of a PtCl crystal. Each peak in the spectra corresponds to a phonon bound state. This figures are taken from [108].

Fig. 1.7, where the data are presented in a stack plot with successively traced offsets along the horizontal axis by increasing multiples of the fundamental frequency (321 cm^{-1}).

Each peak corresponds to an n-phonon bound state. The shift is due to the binding energy of phonons. As much as seven-phonon bound states were observed experimentally. One can also see a well pronounced peak which corresponds to the mixture of a six-phonon bound state and one additional phonon.

All these bound states can be interpreted as *quantum discrete breathers* (QDBs) [104, 3, 48, 22].

1.2.3 Josephson junctions

A much more investigated system is a network of biased Josephson junctions. Each junction can be either in a superconducting or in a resistive state. Geometrical structures of a network (ladder) were proposed which possess discrete breathers, i.e. several junctions are in resistive states and all others are in the superconducting one. A large variety of DBs was observed experimentally [115, 13, 12]. Several examples of a system of coupled Nb-based Josephson junctions with localized states corresponding to discrete breathers are shown in Fig. 1.8. These states of the ladder are visualized by using low temperature scanning laser microscopy.

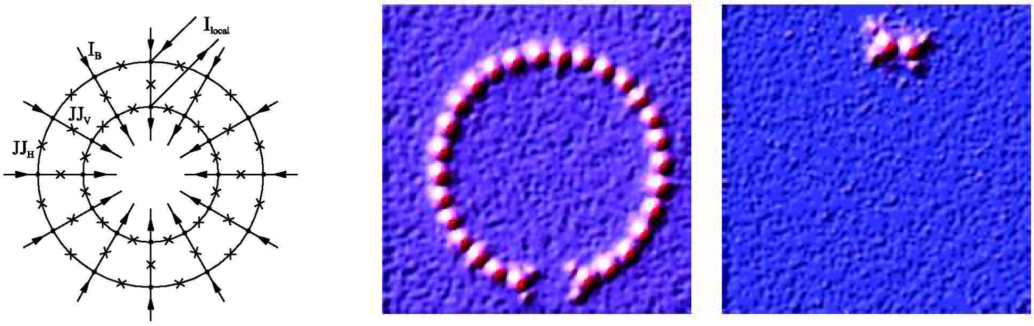

Figure 1.8: Two types of DBs in a system of coupled Josephson junctions are shown. (Left): Schematic view of an annular ladder. Crosses mark the individual junctions. Arrows indicate the direction of external current flow. (Middle): Almost all junctions are in the resistive state. (Right): Only few junctions are in the resistive state. This figures are taken from [13].

The second part of this work is devoted to a detailed description of DBs in Josephson junction ladders.

1.2.4 Micromechanical oscillator arrays

The cantilever array is produced from a photoresistive mask over a silicon nitride layer on a silicon substrate. Cantilevers are made from 300nm thick Si_3N_4 film. The average length of cantilevers is $\approx 53\mu m$. Width and pitch are $15\mu m$ and $40\mu m$, respectively. Such cantilevers have a hard nonlinearity. Following the method described in Ref. [93], in order to produce ILMs, a large amplitude uniform mode instability should be achieved. It can be done by driving the system with the highest frequency of the uniform mode.

Fig. 1.9 shows the room temperature cantilever excitation pattern versus time for a 248-element array. The dark regions versus time identify the trajectories of large amplitude localized excitations.

1.2.5 Other proposals

In addition to the above described examples two more experiments will be discussed.

The first of them is the observation of intrinsic localized spin waves in the quasi-1D biaxial antiferromagnent $(C_2H_5NH_3)_2CuCl_4$ [103]. A microwave pulse was applied in order to create

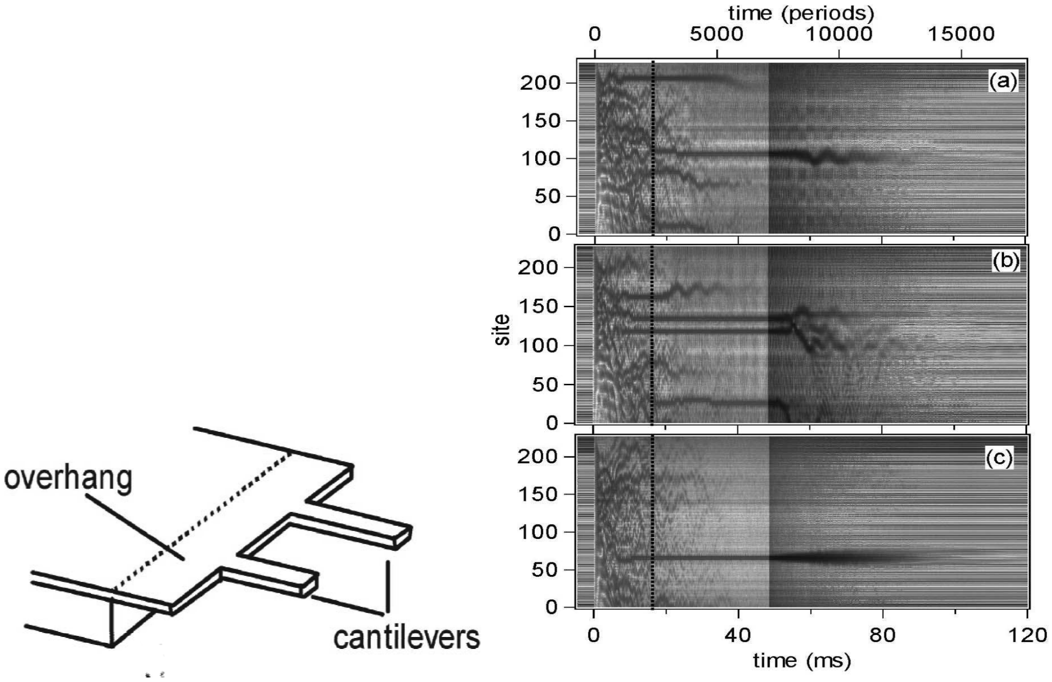

Figure 1.9: (Left): Schematic view of a cantilever array. (Right): Excitation of cantilevers versus time. The regions with bright background correspond to the time where the pulse is on. The dark trajectories indicate localized excitations. This figure is taken from [98].

intrinsic localized modes (ILMs) via the modulational instability [93]. This antiferromagnet is a layered organic material with a strong ferromagnetic coupling of the magnetic Cu^{2+} ions within a layer and with a weak antiferromagnetic coupling between the layers. The size of the sample is $3 \times 3 \times 0.5mm^3$.

The driving pulse excites spin waves and its frequency is lowered due to the intrinsic nonlinearity of the spin Hamiltonian. This allows to study the absorption by the spin system for different power levels of the driving pulse. Experimentally the formation of the broad asymmetric spectral band below the antiferromagnetic resonance with increasing power levels was observed. Following the authors of Ref. [103] this is the signature of localized mode generation.

The other experiment is the observation of self-trapping of the amide I band in a peptide mode crystal [23]. The crystal consists of quasi-1D dimensional chains of hydrogen bonded peptide units (-CO-NH-). The length of this hydrogen bond modulates the transition frequency of the amide I mode of the peptide unit. In this experiment the *nonlinear* spectroscopy was used. A small fraction of the infrared pulses was split off in order to obtain broadband probe and reference pulses, which were spectrally dispersed after interaction with the sample. Pump and probe pulses were polarized about the NH bond. The formation of an anomalous peak in the absorption spectra was observed with decreasing temperature. This peak is not due to the disorder-induced Anderson localization, which should increase in strength with rising temperature. Therefore, the increasing intensity of this peak at low temperature indicates a self-trapped state formation. This state exists on an ultrafast time scale of less then 400 fs.

There are also several theoretical predictions of observation of localized states in other systems. In Refs. [116, 64] it is shown that there is a possibility for discrete breather existence in a Bose-Einstein condensate (BEC) loaded into one- and two-dimensional optical lattices. The condensate is trapped in the potential minima and can coherently tunnel between them. The heights of the barriers can be tuned by the intensity of the laser beam. The interaction within the BEC gives rise to a nonlinearity and the full dynamics of the system is governed by the Discrete NonLinear Schrödinger (DNLS) equation.

Part I

Transport spectroscopy

Motivation

In Hamiltonian systems the small amplitude plane waves with frequencies from the phonon band can freely propagate in the absence of any inhomogeneities. The space localization of the DB implies that such plane waves can also propagate at the tails of DB, far from it's core, where the system is almost at rest. It leads to the possibility to consider the *transport spectroscopy* method by sending phonons with different frequencies to the DB and measure the scattering outcome. Due to the smallness of the amplitude of the phonons it is enough to take into account only the linear approximation of the interaction between phonons and the DB. It will reduce the problem to the scattering setup, where the results of interaction will be also plane waves moving in opposite directions from the DB core. From this point of view the DB is a *time-periodic scattering potential.* The most interesting question is about new features of time-periodic scattering potentials compared to the static ones. One of them is the resonant suppression of the transmission or *perfect reflection* , which was observed already numerically in optical systems and in the DNLS equation [19, 68].

In this part, by using a generalized numerical scheme, the transmission problem is studied for the optical and acoustic systems as well. In both cases zeros of transmission were observed. As it follows from the detailed analysis these zeros *exactly* correspond to Fano resonances known for atomic systems.

In addition to this, the scattering of a soliton by two different defects is considered. The defects are chosen such that both lead to resonant scattering. One of them provides for a resonant transmission while the other provides for a perfect reflection. A question of interest is the role of nonlinearity in the scattering of solitons.

1 The scattering process

In this part only 1D Hamiltonian systems

$$\mathrm{H} = \sum_n \left(\frac{\dot{x}_n^2}{2} + V[x_n] + W[x_n - x_{n-1}] \right) \tag{1.1}$$

with the nonlinear potentials $V[x]$ and/or $W[x]$ will be considered. These systems support time-periodic $\hat{x}_n(t + t_b) = \hat{x}_n(t)$ and spatially localized $\hat{x}_{|n| \to \infty} \to 0$ states - *discrete breathers* (DBs).

1.1 One channel scattering

In order to study the scattering problem, the equations of motion $\ddot{x}_n = -\frac{\partial \mathrm{H}}{\partial x_n}$ should be linearized around the breather solution $x_n(t) = \hat{x}_n(t) + \epsilon_n(t)$:

$$\begin{aligned} \ddot{\epsilon}_n &= -W''[\hat{x}_n(t) - \hat{x}_{n-1}(t)](\epsilon_n - \epsilon_{n-1}) \\ &\quad + W''[\hat{x}_{n+1}(t) - \hat{x}_n(t)](\epsilon_{n+1} - \epsilon_n) - V''[\hat{x}_n(t)]\epsilon_n \ . \end{aligned} \tag{1.2}$$

This is a set of linear equations with time-periodic coefficients. By using Bloch's theorem the solutions of (1.2) can be represented in the form

$$\epsilon_n(t) = \sum_{k=-\infty}^{\infty} e_{nk} \mathrm{e}^{-\mathrm{i}(\omega_q + k\Omega_b)t} \ . \tag{1.3}$$

Each harmonic of a DB generates a *channel*. Generally there is an infinite number of these channels. There are two types of channels: one of them are *open* conducting channels, where plane waves can freely propagate. Others are *closed* channels which are active inside the breather core, i.e., the spatial amplitudes e_{nk} are localized in space (see Fig. 1.1).

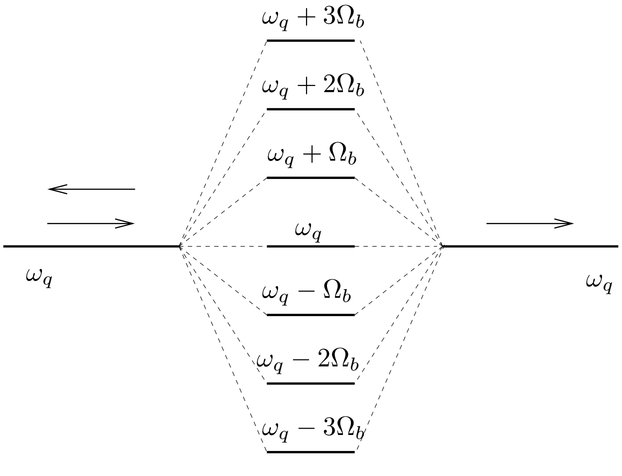

Figure 1.1: Schematic representation of the one-channel scattering of a wave by a discrete breather.

If $\Omega_b > 2|\omega_\pi|$ then there is only one open channel $k = 0$ and all channels with nonzero k are closed. The frequencies of transmitted and reflected waves are equal and coincide with the the frequency of the incoming wave, since they all belong to the open channel with $k = 0$.

In the case $|\omega_0| + |\omega_\pi| < \Omega_b < 2|\omega_\pi|$ a q' exists such that the equality $\omega_{q'} = \Omega_b - \omega_q$ is fulfilled. This implies that in this case *two* channels are open and the frequencies of incoming and outcoming waves may not coincide. Note here, that for acoustic systems $\omega_0 \equiv 0$. For optical systems the frequency of the breather may lie in a gap $\Omega_b < |\omega_0|$. It leads to the additional (and more general) condition for the multi-channel scattering

$$\omega_{q'} = \omega_q + k\Omega_b \ . \tag{1.4}$$

The one-channel scattering is more common and the only one which will be considered.

For harmonic interaction potentials W it was shown in Ref. [19] that the momentum

$$J = -W''[0]\langle \mathrm{Im}\epsilon_n^* \epsilon_{n-1} \rangle \tag{1.5}$$

is independent of the lattice site. Here the averaging is meant with respect to time. In a similar way it is straightforward to show that the quantity

$$\tilde{J} = -\langle W''[\hat{x}_n(t) - \hat{x}_{n-1}(t)] \mathrm{Im}\epsilon_n^* \epsilon_{n-1} \rangle \tag{1.6}$$

is independent of the lattice site (see Appendix B). Since the breather solution $\hat{x}_n(t)$ is spatially localized, at large distances from the breather it is found again that the momentum J is independent of the lattice site. Especially, it is the same for $n \to \pm\infty$. Following Ref. [19] it is possible to conclude that the one-channel scattering case is *elastic*, i.e., the energy of an incoming wave equals the sum of the energies of the outgoing (reflected and transmitted) waves.

Assuming that the breather is located around the central site $n = 0$, the one-channel scattering problem can be written as

$$\begin{aligned} \epsilon_n(t) &= A_I e^{-i(\omega_q t + qn)} + A_R e^{-i(\omega_q t - qn)}, \quad n \ < \ 0 \,, \\ \epsilon_n(t) &= A_T e^{-i(\omega_q t - qn)} \quad , n \ > \ 0 \end{aligned} \tag{1.7}$$

for

$$|n| \gg \sup[\xi_b(0), \xi_b(\omega_q)] \tag{1.8}$$

where $\xi_b(\omega) = \sup \xi(\omega + k\Omega_b)$ and

$$\begin{array}{ll} \sinh^2 \xi(\nu)/2 = \frac{V''[0] - \nu^2}{4W''[0]} \ , & |\nu| < \omega_q(0) \\ \cosh^2 \xi(\nu)/2 = \frac{\nu^2 - V''[0]}{4W''[0]} \ , & |\nu| > \omega_q(\pi) \end{array} \tag{1.9}$$

Here ξ measures the characteristic localization length of a closed channel at frequency ν (note that for $\nu = k\Omega_b$ the localization length is that of the breather itself, see also [19]). The incoming wave has amplitude A_I, and the reflected and transmitted wave amplitudes are given by A_R and A_T, respectively. The transmission coefficient $t_q = |A_T/A_I|^2$.

For further considerations the notation of the Bloch functions $\zeta_n(t)$ defined as

$$\epsilon_n(t) = \zeta_n(t) e^{-i\omega_q t} \tag{1.10}$$

will be used.

In order to estimate the relative strength of closed channels with $k \neq 0$ the time-periodic coefficients of (1.2) are expanded in a Fourier series with respect to time:

$$\begin{aligned} W''[\hat{x}_n(t) - \hat{x}_{n-1}(t)] &= \sum_{k=-\infty}^{\infty} w_{n,k} \mathrm{e}^{\mathrm{i}k\Omega_b t} \ , \\ V''[\hat{x}_n(t)] &= \sum_{k=-\infty}^{\infty} v_{n,k} \mathrm{e}^{\mathrm{i}k\Omega_b t} \ . \end{aligned} \tag{1.11}$$

Firstly, the case of a strongly localized optical breather located at site $n = 0$ with $W(y) = \frac{c}{2}y^2$ is considered. By inserting (1.11) and (1.3) into (1.2) and taking into account a single closed channel with some value of k at the breather center $n = 0$, we get

$$\begin{aligned} \omega_q^2 e_{0,0} &= -e_{00} + C(e_{1,0} + e_{-1,0} - 2e_{0,0}) - (v_{0,0} - 1)e_{0,0} - v_{0,-k}e_{0,k} \ , \\ (\omega_q + k\Omega_b)^2 e_{0,k} &= C(e_{1,k} + e_{-1,k} - 2e_{0,k}) - v_{0,0}e_{0,k} - v_{0,k}e_{0,0} \ . \end{aligned} \tag{1.12}$$

Assuming that $e_{1,k} \approx e_{-1,k}$, one can extract e_{nk} from the second equation in (1.12) and substitute it into the first one

$$\begin{aligned} \omega_q^2 e_{0,0} &= -e_{00} + C(e_{1,0} + e_{-1,0} - 2e_{0,0}) - (v_{0,0} - 1)e_{0,0} \\ &\quad + \frac{|v_{0,k}|^2}{(\omega_q + k\Omega_b)^2) - v_{0,0} - 2c(1 - \eta_k)} e_{0,0} \ , \end{aligned} \tag{1.13}$$

where η_k is the relative amplitude

$$\eta_k = \pm \frac{e_{1,k}}{e_{0,k}} = \mathrm{e}^{-1/\xi(\omega_q + k\Omega_b)} \ . \tag{1.14}$$

It has a positive sign for $\omega_q + k\Omega_b$ located inside the phonon gap and a negative sign otherwise.

The relative strength s_k of the closed channel with respect to the open one can be estimated through the competition between the fourth and the third terms in (1.13)

$$s_k = \frac{|v_{0,k}|^2}{|(v_{0,0} - 1)(v_{0,0} + 2c(1 - \eta_k) - (\omega_q + k\Omega_b)^2)|} \ . \tag{1.15}$$

For $s_k \ll 1$ there is no significant contribution from the given closed channel, while $s_k \geq 1$ indicates a strong influence of the closed channel on the scattering process. Note that the expression $\sqrt{v_{00} + 2c(1 - \eta_k)}$ in the denominator of (1.14) is just a frequency ω_{L0} of a *local phonon mode* of the time-average scattering potential. Notice that in discrete systems these local phonon modes may be located below or above the phonon band. The denominator of (1.14) may vanish for certain wave numbers, which would imply a resonance-like enhancement of the closed channel contribution (for certain wave numbers q). Such a resonant enhancement of a closed channel amplitude acts as a huge effective scattering potential to the open channel, and therefore a *resonant suppression of transmission* is expected. Thus, qualitatively such a complete suppression of transmission (Fano-like resonance [26, 66], discussed below) is explained by a resonant interaction of the propagating phonon with the specific local phonon mode. However in order to quantitatively analyze this effect the renormalization of the value of ω_{L0} due to all nonresonant processes has to be taken into account.

In a similar way an estimate of the closed channel contribution of acoustic breathers may be obtained, which gives the following expression for the relative strength r_k

$$r_k = \frac{|w_{0,k}|^2}{|(w_{0,0})(w_{0,0} - (\omega_q + k\Omega_b)^2)|} \ . \tag{1.16}$$

Thus, again a resonant suppression of transmission is found, when the presence of acoustic DB leads to a local *increase* in the nearest neighbor interaction and to a corresponding local phonon mode. However, this case is much more involved as compared to an optical DB case, and Eq. (1.16) may serve only as a qualitative tool to check whether or not a closed channel is strongly contributing to the transmission.

1.2 Time-averaged scattering potential

In order to understand the importance of the time dependence of the scattering potential, a comparison of the numerical results with those obtained by time-averaging the DB scattering potential must be made. This time-averaging can be done numerically and Eq. (1.2) becomes

$$\begin{aligned} \ddot{\tilde{\epsilon}}_n &= -\langle W''[\hat{x}_n - \hat{x}_{n-1}]\rangle(\tilde{\epsilon}_n - \tilde{\epsilon}_{n-1}) + \\ &\quad \langle W''[\hat{x}_{n+1} - \hat{x}_n]\rangle(\tilde{\epsilon}_{n+1} - \tilde{\epsilon}_n) - \langle V''[\hat{x}_n]\rangle\tilde{\epsilon}_n \end{aligned} \tag{1.17}$$

Since in this case all inhomogeneities are time-independent the standard scattering matrix method can be used. With $\tilde{\epsilon}_n(t) = \tilde{\zeta}_n e^{-i\omega_q t}$ Eq. (1.17) is rewritten as

$$\begin{pmatrix} \tilde{\zeta}_{n+1} \\ \tilde{\zeta}_n \end{pmatrix} = \mathbf{M}_n \begin{pmatrix} \tilde{\zeta}_n \\ \tilde{\zeta}_{n-1} \end{pmatrix}, \tag{1.18}$$

with

$$\mathbf{M}_n = \begin{pmatrix} 1 + \frac{E_n + c_{n,n-1} - \omega_q^2}{c_{n+1,n}} & -\frac{c_{n,n-1}}{c_{n+1,n}} \\ 1 & 0 \end{pmatrix} \tag{1.19}$$

where $E_n = \langle V''(\hat{x}_n)\rangle$ and $c_{n,n-1} = \langle W''(\hat{x}_n - \hat{x}_{n-1})\rangle$. It follows that

$$\begin{pmatrix} \tilde{\zeta}_{N+1} \\ \tilde{\zeta}_N \end{pmatrix} = \mathbf{M} \begin{pmatrix} \tilde{\zeta}_{-N} \\ \tilde{\zeta}_{-N-1} \end{pmatrix}, \tag{1.20}$$

with

$$\mathbf{M} = \prod_{i=N}^{-N} \mathbf{M}_i \tag{1.21}$$

The expression for the transmission coefficient $\tilde{t}_q$ for the time averaged scattering potential is then given by [112]

$$\tilde{T}_q = \frac{4\sin^2 q}{|M_{11}(q)e^{-iq} + M_{12}(q) - M_{21}(q) - M_{22}(q)e^{iq}|^2} \tag{1.22}$$

where M_{ij} are the four matrix elements of the 2 × 2 matrix $\mathbf{M}$.

2 Acoustic lattices

In this chapter wave scattering by so-called *acoustic breathers* is studied. The corresponding systems are characterized by a gapless spectrum ω_q of propagating linear waves, and by a conservation of the total mechanical momentum.

2.1 Scattering by acoustic breathers

The generic choice for the potentials in the Eq. (1.2) is

$$V(y) \equiv 0\ , \quad W(y) = \frac{1}{2}y^2 + \frac{\beta}{3}y^3 + \frac{1}{4}y^4\ . \tag{2.1}$$

This choice leads to the well known Fermi-Pasta-Ulam (FPU) system [82].

2.1.1 Case $\beta = 0$

First the case $\beta = 0$ is considered. It implies even parity of the interaction potential W. We will comment on the influence of an odd parity contribution for $\beta \neq 0$ later on. The dispersion relation of phonons is given by

$$|\omega_q| = 2\sin\frac{q}{2} \tag{2.2}$$

A breather solution with frequency $\Omega_b = 4.5$ and the corresponding Fourier components of the scattering potential are plotted in Fig. 2.1.

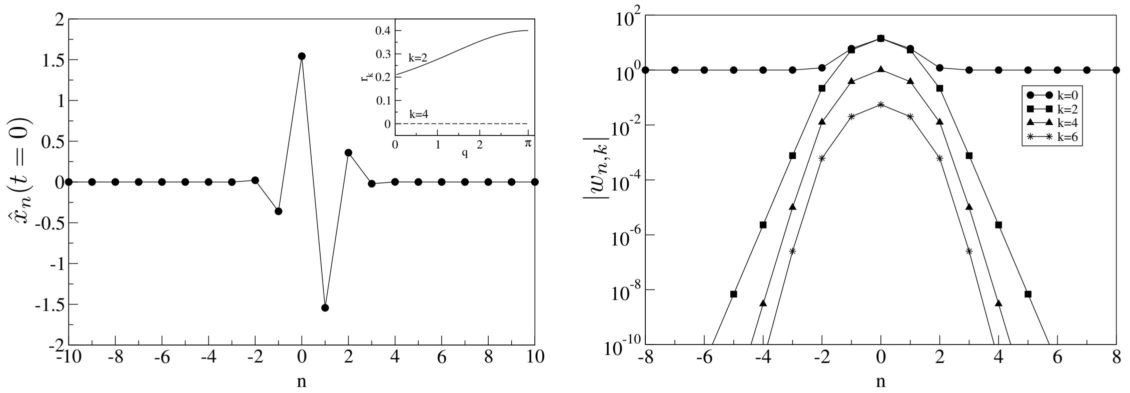

Figure 2.1: (Left): Displacements of an acoustic breather with zero velocity at $t = 0$ and $\Omega_b = 4.5$. Inset: Relative strength r_k for the second and fourth closed channels versus q. (Right): Fourier components w_{nk} for different k versus n for the breather

Acoustic breathers can be found with frequencies above the phonon band $|\Omega_b| > \max|\omega_q|$. However, here the following condition $|\Omega_b| > 2\max|\omega_q|$ should be used, which implies $|\Omega_b| > 4$. This condition is needed to realize the one-channel scattering case of linear waves. For $\beta = 0$ the ac part of the interaction potential W contains even harmonics only. The closed channels in this case are weak and play no important role in the scattering process. As a consequence

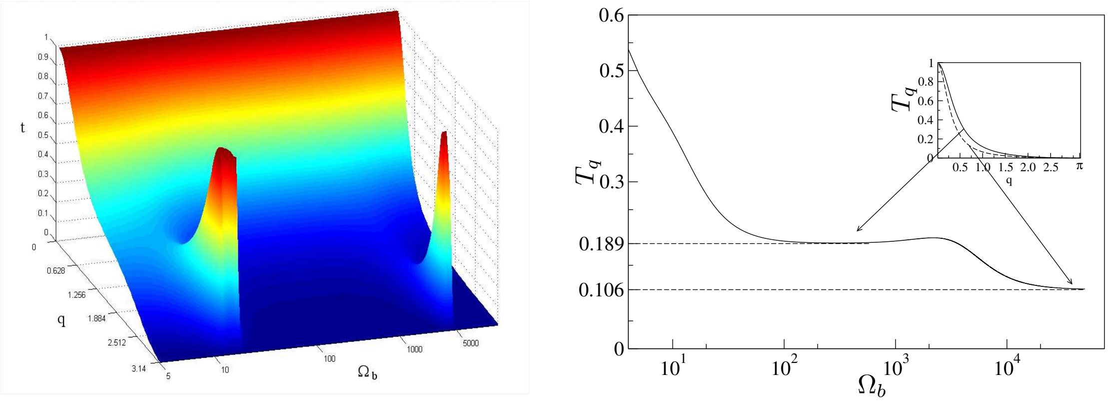

Figure 2.2: (Left): The dependence of the transmission coefficient on q and Ω_b.
(Right): The dependence of the transmission coefficient on Ω_b for a particular value of $q = \frac{\pi}{4}$. The dashed lines show the predicted plateau heights (see text). The inset shows the dependence of the transmission on q for the two observed plateau regions.

wave scattering by acoustic breathers is practically identical with scattering by the time-averaged potential. Indeed, numerical computations do not show any relevant difference between the linear wave propagation in the presence of time-dependent and static (time-averaged) potentials. Yet there is a number of interesting features of the scattering which deserve to be exploited.

For $V = 0$ the lattice conserves the total mechanical momentum $P = \sum_n \dot{x}_n$ in addition to the energy. Without loss of generality P can be chosen zero here. From this conservation law it follows that the total mechanical momentum of the linearized problem $\Pi = \sum_n \dot{\epsilon}_n$ is also conserved. This implies that for any solution $\epsilon_n(t)$ the shift $\epsilon(t) + C$ is also a solution. In particular $\epsilon_n = C$ is a solution, which corresponds to a wave with $q = 0$ and therefore $t_{q=0} = 1$. It follows, that the transmission of waves by a breather for acoustic systems at $q = 0$ is always perfect, no reflection occurs. This is in sharp contrast to systems without conservation of total mechanical momentum.

The peculiar dependence of the transmission coefficient T_q on the wave number q and the breather frequency Ω_b is shown in Fig. 2.2. The breather frequency is varying over nearly three decades. We indeed observe perfect transmission at $q = 0$, and zero transmission at $q = \pi$. However, in the studied breather frequency range, two rather narrow peaks around $q = \pi$ appear with perfect transmission. These structures are due to the detachment of localized Floquet eigenvectors from the continuum of extended Floquet eigenstates.

A surprising result is shown in Fig. 2.2. The transmission t_q at $q = \pi/4$ as a function of the breather frequency Ω_b is plotted. There are plateaus and crossovers at certain breather frequencies. The crossover positions clearly correlate with the appearance of localized Floquet states, which are traced through the perfect transmission close to $q = \pi$ in Fig. 2.2. The dependence of the transmission on q for the two observed plateaus is shown in the inset of Fig. 2.2. The plateaus range over several decades in Ω_b, and the q-dependence of t_q is rather similar on different plateaus.

To understand this feature one should keep in mind that large breather frequencies imply that the breather energy and its amplitude in the breather center are large as well. Thus it is possible to neglect the harmonic part of the interaction potential W inside the breather core. The resulting amplitude distribution of the breather core is characterized by a superexponential decay $\hat{x}_n(t) = A_n G(t)$, $A_n \sim A_{n-1}^3$, where $G(t)$ is an oscillatory master function [31, 21]. Due to the symmetry of the breather solution the spatial profile is described by $A_{-n} = -A_{n+1}$, $n \leq 0$. The amplitudes A_n have been computed: $A_1 = 1$, $A_2 \simeq -0.166$, $A_3 \simeq 4.796\ 10^{-4}$, $A_4 \simeq -1.15\ 10^{-11}$, and so on [82]. The overall amplitude of the oscillations $\hat{x}_n(t)$ is tuned by the amplitude of the master function $G(t)$. The scattering is essentially described *only* by the time-averaged scattering potential. This potential corresponds to a large *increase* in the

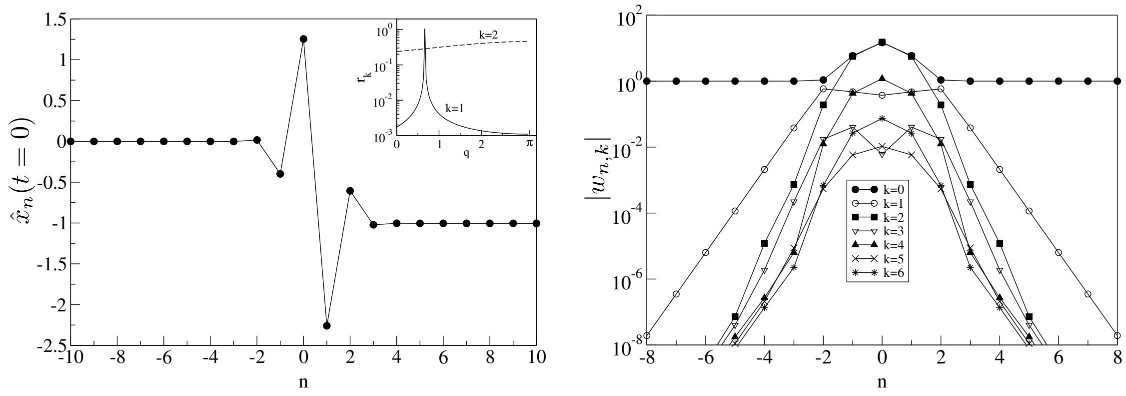

Figure 2.3: (Left): Displacements of an acoustic breather with zero velocities at $t = 0$ and $\Omega_b = 4.5$ for the case $\beta = 1.$. Inset: Relative strength r_k for the second and fourth closed channels versus q.
(Right): Fourier components w_{nk} for different k versus n for the breather.

nearest neighbor coupling terms. In the breather center it is

$$\langle W''[\hat{x}_1(t) - \hat{x}_0(t)]\rangle = 1 + 3\langle(\hat{x}_1(t) - \hat{x}_0(t))^2\rangle \ . \tag{2.3}$$

This time average coupling term is proportional to the square of the frequency of the breather (see Appendix C.1)

$$3\langle(\hat{x}_1(t) - \hat{x}_0(t))^2\rangle \equiv X^2 \approx \frac{2}{3\pi}\Omega_b^2 \ . \tag{2.4}$$

Due to the large value of X for large Ω_b it becomes evident that time-dependent corrections to the scattering potential are negligible. By making use of the distribution of oscillation amplitudes in the lattice it is found that

$$3\langle(\hat{x}_n(t) - \hat{x}_{n-1}(t))^2\rangle \approx A_n^2 X^2. \tag{2.5}$$

The scattering on a plateau in Fig. 2.2 is due to a finite number of matrices $\mathbf{M}_n$ which should be taken into account in Eq. (1.21). Qualitatively the crossover threshold can be defined as

$$A_n^2 X^2 \simeq 1 \quad . \tag{2.6}$$

Thus it produces the two crossover frequencies $\Omega_{b1} = 13.1$ and $\Omega_{b2} = 4527$, which match with the observed crossover positions. For $4 < \Omega_b < \Omega_{b1}$ only 4 matrices $\mathbf{M}_n$ are needed, for $\Omega_{b1} < \Omega_b < \Omega_{b2}$, 6 matrices $\mathbf{M}_n$ and so on. The transmission at $q = \pi/4$ using the corresponding reduced set of relevant matrices was computed too. The obtained limiting values of t_q are shown as a dashed line in Fig. 2.2.

One can see a very good agreement between the predicted plateau heights and the actual data obtained in direct numerical simulations.

The acoustic breather presents an *effective potential well* for the propagating phonons. The width of this well increases with the breather frequency, and the number of possible localized Floquet states also increases. Such a periodic appearance of perfect transmission is similar to the quantum mechanical scattering by a potential well in the presence of *quasi-discrete* levels [90].

2.1.2 Case $\beta \neq 0$

Finally, the influence of $\beta \neq 0$ was checked. With respect to the breather the presence of cubic terms in the interaction potential leads to the generation of a kink-shaped dc lattice distortion Fig. 2.3(left). The corresponding scattering potential becomes asymmetric in space and odd

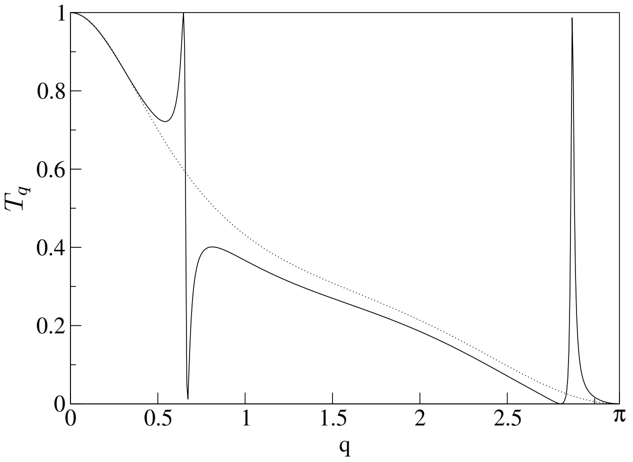

Figure 2.4: The dependence of the transmission coefficient on q for an acoustic breather with $\Omega_b = 4.5$ and $\beta = 1$. The dashed line is the result for the time-averaged scattering potential. Two transmission zeros are observed at corresponding values of q.

harmonics in the ac scattering potential appear Fig. 2.3(right). This immediately leads to the possibility of matching between the frequency of a propagating phonon in a closed channel $\Omega_b - \omega_q$ (see Fig. 2.3(inset)) and several local modes of the time-averaged scattering potential.

Thus, a resonant suppression of a transmission appears in this case. Indeed, this effect can be observed by direct numerical simulations as shown in Fig. 2.4, where two transmission zeros are found. One of them at $q \approx 0.7$ corresponds to the sharp peak on the relative strength of the channel $k = 1$ on Fig. 2.3(inset).

Moreover, this figure shows the existence of perfect transmissions also. This is due to local levels generated by the DB itself.

2.2 Scattering by acoustic rotobreathers

Remarkable differences to the results of the preceding Section are obtained if the interaction potential W is chosen to be a periodic one (the potential V is still zero in this Section):

$$W(y) = 1 - \cos(y). \tag{2.7}$$

With such an interaction potential the nonlinear chain allows for the existence of *rotobreathers* (RB) (cf. Fig. 1b). In the simplest case a rotobreather consists of one particle being in a rotating (whirling) state and all others particles oscillating with spatially decaying amplitudes from the center of DB:

$$\begin{aligned} \hat{x}_0(t + t_b) &= \hat{x}_0(t) + 2\pi, \\ \hat{x}_{n\neq 0}(t + t_b) &= \hat{x}_{n\neq 0}(t), \\ \hat{x}_{|n|\to\infty} &\to 0. \end{aligned} \tag{2.8}$$

To excite such a rotobreather the central particle needs to overcome the potential barrier generated by its two nearest neighbors. The rotobreather energy is thus bounded from below by $E_b > 4$. At sufficiently large energies $E_b \gg 4$ the central particle will perform nearly free rotations $\hat{x}_0(t) = \Omega_b t + \delta(t)$ with $\delta(t + t_b) = \delta(t)$ being a small correction. The time-averaged off-diagonal hopping terms between site $n = 0$ and $n = \pm 1$ are then given by

$$\langle \cos(\hat{x}_0(t) - \hat{x}_1(t)) \rangle \approx -\langle \sin(\Omega_b t)(\delta(t) - \hat{x}_1(t)) \rangle \tag{2.9}$$

where $\hat{x}_1(t)$ is also a small function and can be written as (see Appendix C.2)

$$\langle \cos(\hat{x}_0(t) - \hat{x}_1(t)) \rangle \approx -\frac{3}{2\Omega_b^2}. \tag{2.10}$$

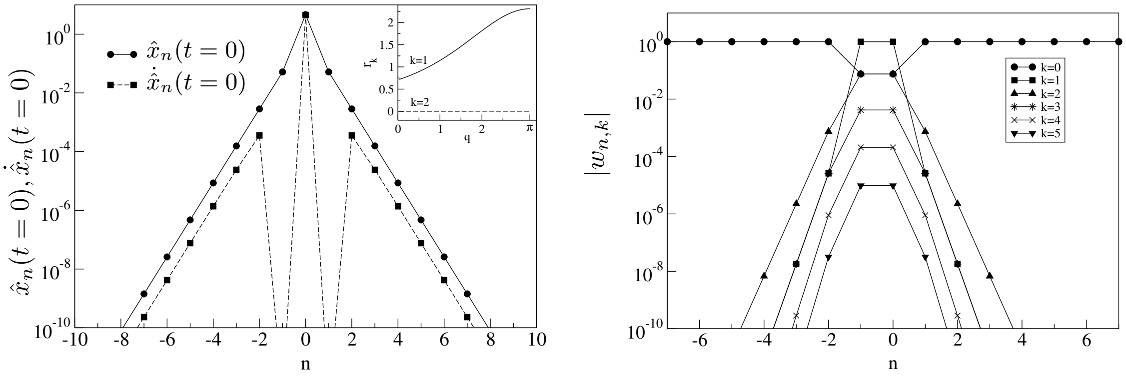

Figure 2.5: (Left): Displacements (solid line) and velocities (dashed line) of an acoustic rotobreather at $t = 0$ with $\Omega_b = 4.5$. Inset: Relative strength r_k of the first and second closed channel versus q.
(Right): Fourier components w_{nk} for different k versus n for the rotobreather

Thus the time-averaged scattering potential of a rotobreather cuts the chain into nearly non-interacting parts, contrary to the previous case of an acoustic breather. Therefore it becomes extremely difficult for waves to penetrate across the rotobreather. The rotobreather solution with $\Omega_b = 4.5$ is shown in Fig. 2.5.

The corresponding Fourier components of the scattering potential are shown in Fig. 2.5. In Fig. 2.6 the q-dependence of the transmission for a rotobreather with $\Omega_b = 4.5$ is shown and compared to the corresponding curve of an acoustic breather from the preceding section. On can see a dramatic decrease of the transmission at all q-values for the rotobreather, in agreement with the above analysis.

The time-averaged scattering potential for large Ω_b corresponds to two neighboring weak links of strength (2.10) inserted in a linear acoustic chain. Three matrices $\mathbf{M}_n$ are enough to compute the transmission. Two of them involve matrix elements which are proportional to Ω_b^2. The elements of the product will thus contain terms proportional to Ω_b^4, and according to (1.22) the result is

$$\tilde{T}_q \sim \Omega_b^{-8}. \tag{2.11}$$

This is precisely what was found in a numerical evaluation of the transmission for the time-averaged scattering potential in Fig. 2.6. However, although the transmission coefficient T_q for the full time-dependent scattering potential also drastically decreases with q and Ω_b, the dependence is weaker than for the case of the time-averaged rotobreather potential. It scales as

$$T_q \sim \Omega_b^{-4} \tag{2.12}$$

(see also Fig. 2.6). The reason is that besides a weak static link the rotobreather scattering potential has an ac term with frequency Ω_b of amplitude one (see Fig. 2.5). Thus an alternative route for the wave is to approach the rotobreather, to be excited into the first closed channel, to pass the breather and to relax back into the open channel. The corresponding scattering process of "virtual" absorption and emission of phonons from the rotobreather can be also represented by three matrices as it happens for the dc analysis. However, now there are two weak links in open channel and there are links of order one in closed channels with a frequency change at site $n = 0$ from ω_q to $\omega_q + \Omega_b$. This occurs in exactly one of the three matrices. Consequently the product matrix will contain elements proportional to Ω_b^2 and the transmission will scale as (2.12).

To conclude this section it should be stressed that *wave scattering by an acoustic rotobreather is essentially relying on the time-dependence of the scattering potential.* The rotobreather effectively cuts the chain into weakly interacting parts and thus hinders strongly waves from propagating.

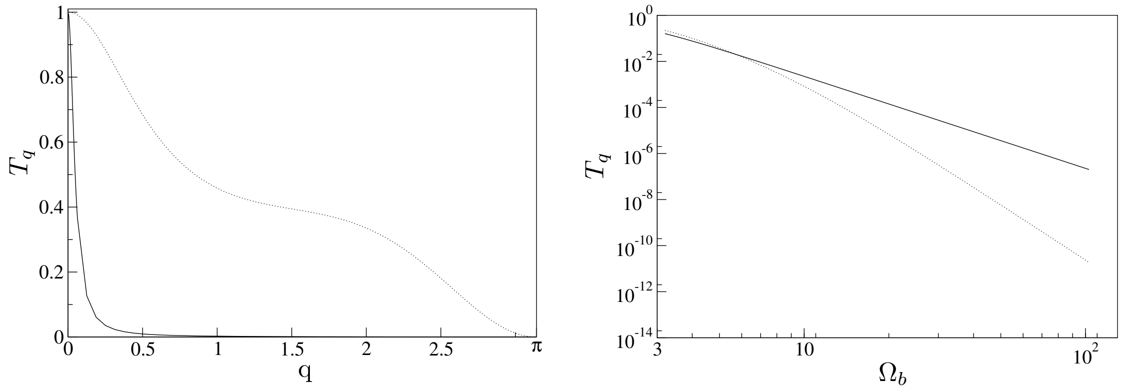

Figure 2.6: (Left): The dependence of the transmission coefficient on q for $\Omega_b = 4.5$. Data for acoustic rotobreather and acoustic breather are shown correspondingly by solid and dashed lines.
(Right): The dependence of the transmission coefficient on the frequency of the breather Ω_b at fixed $q = 0.21$. Scattering by "real" rotobreather and a static part of DB are shown correspondingly by solid and dashed lines.

3 Optical lattices

In this chapter systems with a nonvanishing on-site potential $V[x_n] \neq 0$ (see Fig. 1c) are considered. The difference of such systems to acoustic models is the existence of a gap in the spectrum of phonons $|\omega_{q=0}| = V''[0]$. As a consequence the total mechanical momentum is not conserved, and the transmission coefficient vanishes not only at $q = \pi$ but also at $q = 0$. An exception is the case when a localized Floquet eigenstate bifurcates from the corresponding band edge for some special parameters [19, 68, 67]. Because of the presence of a gap in the plane wave spectrum there are now two different cases of interest - the breather frequency being located outside the spectrum $|\Omega_b| > \max|\omega_q|$ or inside the gap $|\Omega_b| < \min|\omega_q|$.

Scattering on some of these systems was already considered in Ref. [19, 68]. The aim of this chapter is to compare the results of time-averaged and time-periodic scattering potentials in optical systems.

3.1 The case $|\Omega_b| > \max|\omega_q|$.

Here the particular potentials $V(y) = \frac{1}{2}y^2 + \frac{1}{3}y^3 + \frac{1}{4}y^4$ and $W(y) = \frac{c}{2}y^2$ are chosen.

In this case the spectrum of phonons is

$$\omega_q^2 \;=\; 1 + 4c\sin^2(\frac{q}{2}) \quad . \tag{3.1}$$

The breather profile for $\Omega_b = 1.5$ and $c = 0.05$ and the corresponding Fourier components of the scattering potential are plotted in Fig. 3.1.

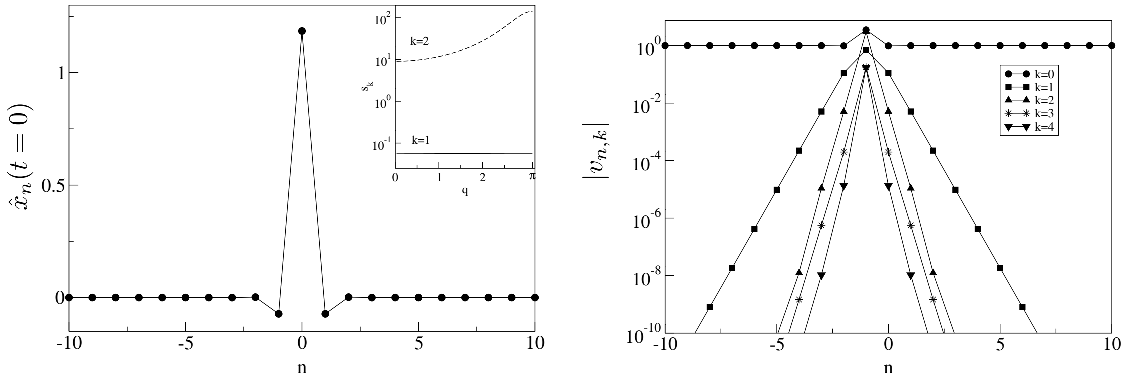

Figure 3.1: (Left): The initial displacements of an optical breather with $\Omega_b = 1.5$ and $c = 0.05$ (velocities are zero). Inset: $s_{k=1,2}$ versus q.
(Right): Fourier components v_{nk} for different k versus n for the breather.

It should be noted that the DB scattering potential perturbs the diagonal terms and in this particular case ($\Omega_b > \omega_q$) presents a *barrier* for propagating phonons. For large breather frequencies the breather is strongly localized, i.e., essentially only one central oscillator is excited. It is straightforward to observe that the transmission coefficient will thus scale as (see Eq.(2.12))

$$\tilde{T}_q \sim \Omega_b^{-4}. \tag{3.2}$$

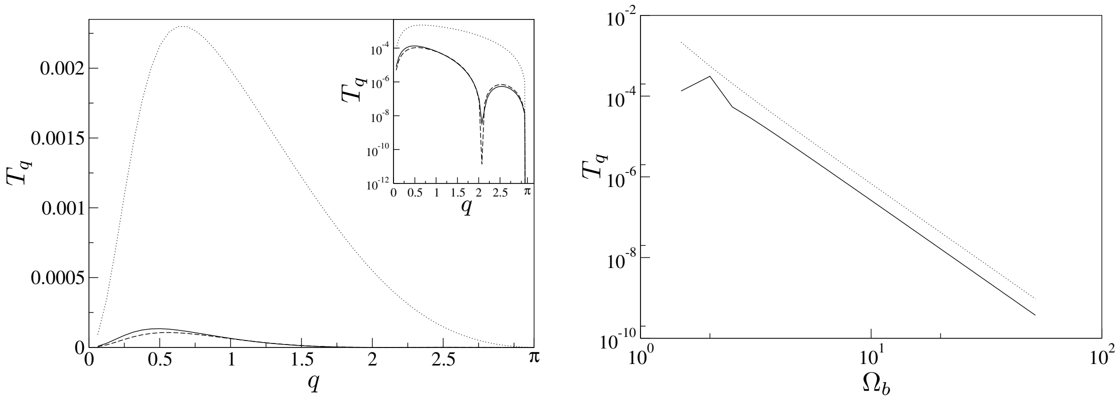

Figure 3.2: (Left): The dependence of the transmission coefficient T_q on the wave number q. The optical breather frequency is $\Omega_b = 1.5$ and the coupling $c = 0.05$. The results are shown for the time-averaged DB scattering potential (dotted line); the time averaged part and the second harmonic of the DB scattering potential (dashed line); the full DB scattering potential (solid line).
Inset: same with t_q on a logarithmic scale. Note the resonant suppression around $q = 2.1$.
(Right): The dependence of the transmission coefficient T_q on the optical breather frequency Ω_b for a particular value of wave number $q = 0.5$. The dashed line corresponds to the scattering by a time-averaged DB scattering potential.

Due to the fact that the transmission vanishes exactly for both $q = 0$ and $q = \pi$ we conclude that for large breather frequencies transmission is suppressed in general.

However, in the case of an optical DB the time-dependent part of the DB scattering potential (more precisely its second harmonic, see Fig. 3.1) is also large. Thus, the time-dependent part of the DB potential can be rather important. Indeed, for the breather from Fig. 3.1 the obtained transmission as a function of q shows that $\tilde{T}_q$ (see Fig. 3.2, dashed line) is at least one order of magnitude larger than T_q (see Fig. 3.2, solid line). In addition T_q shows a resonant minimum around $q = 2.1$ (see inset). Let us use the estimation (1.15) for $k = 1, 2$. The parameters are $v_{0,0} = 3.5$, $v_{0,1} = 0.69$, $v_{0,2} = 3$. First one can find that $s_1 \approx 0.05$ for all q implying that the $k = 1$ closed channel does not participate in the transmission process. At the same time $s_2 > 10$ for all q and thus, the $k = 2$ closed channel strongly participates in the transmission process. It is because the frequency of the propagating phonon $2\Omega_b - \omega_q \simeq 1.92$ is close to a localized eigenmode of the time-averaged scattering potential $\omega_L = 1.9$.

Notice here that the frequency of this local mode is above the phonon band. Thus the suppression of transmission can be interpreted as a strong coupling between the propagating wave and a localized mode of the time-averaged scattering potential, mediated by the ac terms of the scattering potential (the $k = 2$ channel in this case). But this description is valid only for weak coupling between open and closed channels and was already discussed for the oscillating δ-function potential, see [7, 111, 74, 86]. The whole true picture is quite surprising and will be described in details in the next chapter.

Note here, that taking into account the static part and the second harmonic of the DB potential allows to obtain a good agreement with the direct numerical simulations of a scattering by the "full" DB (compare solid and dashed lines in Fig. 3.2). It is also interesting to mention that the static part and the first harmonic of the DB potential ($k = 1$) lead to an *increase* of the transmission coefficient compared to the scattering by the time-averaged DB potential. It is just due to the interplay between the strengths of different channels of the scattering potential (see Eq. (1.15)).

Thus, in the presence of a closed channel the absorption and emission of phonons around the center of the breather leads to strong interference effects which are of destructive nature in the given example of an optical breather.

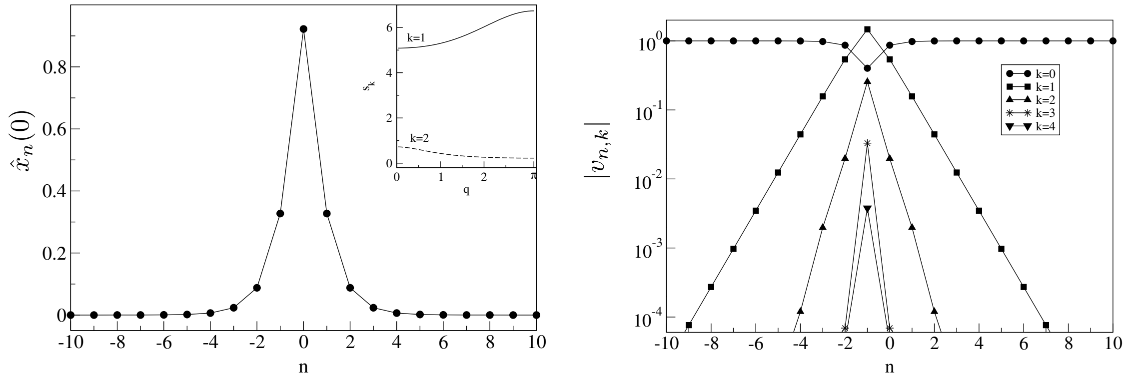

Figure 3.3: (Left): The initial displacements of an optical breather with $\Omega_b = 0.85$ and $c = 0.15$ (velocities are zero). Inset: $s_{k=1,2}$ versus q.
(Right): Fourier components v_{nk} for different k versus n for the breather.

3.2 The case $|\Omega_b| < \min|\omega_q|$

In this case the on-site potential is chosen in the form $V(y) = \frac{1}{2}y^2 - \frac{1}{3}y^3$ (note here that the results do not change if the cubic term has a positive sign) and the interaction term as berfore $W(y) = \frac{c}{2}y^2$. The breather profile for $\Omega_b = 0.85$ and $c = 0.15$ is shown in Fig. 3.3.

The corresponding Fourier components of the scattering potential are plotted in Fig.3.3. In this case the time-averaged DB scattering potential corresponds to a *potential well* in the diagonal terms. In distinction to the optical DB with high frequency (preceding subsection), the number of active closed channels may now increase substantially. This leads to a more complicated interference scenario between the open channel and several closed channels. Indeed, an estimate of $s_{k=1,2}$ shows that the first channel is strongly contributing, and the second closed channel can not be neglected either. In distinction to the previous case for all propagating phonon frequencies the $k = 1$ closed channel has a much stronger contribution than the $k = 2$ one.

In Fig. 3.4 the time-averaged DB scattering potential shows perfect transmission at a certain wave number due to the presence of a quasi-bound state in the static scattering potential. At the same time the transmission for the full dynamical problem shows a maximum value of 0.1, and an additional minimum in $t(q)$ with vanishing transmission. These patterns are entirely absent in the scattering by the time-averaged potential.

We conclude that the presence of active closed channels inside the breather core leads to strong interference effects. In the next chapter, by using a simple model an improved understanding of such phenomena will be provided.

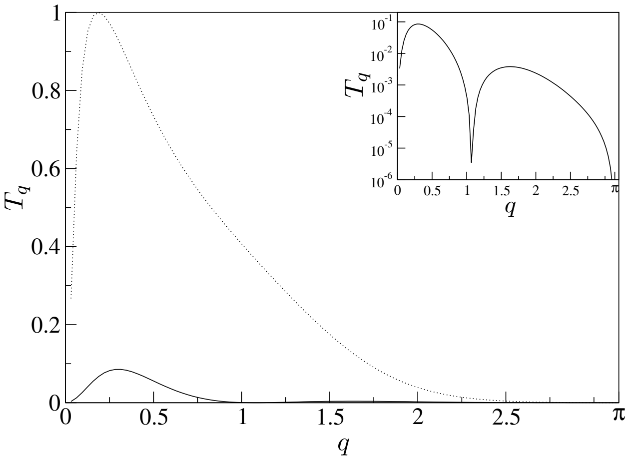

Figure 3.4: The numerically calculated dependence of the transmission coefficient T_q (solid line) on q for the breather frequency $\Omega_b = 0.85$ and $c = 0.15$. The dashed line shows the scattering by the time-averaged DB scattering potential. Inset: The same on a logarithmic scale.

4 Perfect reflections and Fano resonance

The previous results show that vanishing transmissions are quite general in scattering by DBs. This is a crucial difference between static and time-periodic scattering potentials. In Ref. [68] the similarity between perfect reflection in the transmission through a DB and *Fano resonance* was discussed. Fano [26] has shown that in an atomic system under proper conditions the transition probability to an additional energy level, which is coupled to a continuum vanishes. It produces an asymmetric line shape in the transmission. This phenomenon was observed in different experiments, mostly in quantum systems.

The aim of this chapter is to provide a full understanding of the appearance of the zeros of transmission concerning breathers. Firstly, the DNLS equation will be considered, where zeros of transmission were observed as well [68]. A DBs in this model generates only two channels - one of them is open and the other one is closed. Due to this tractable form it is possible to do an analytical approach in the limit of weak coupling. Keeping in mind the understanding of the mechanism for the total reflection, this will be used to *predict* the Fano resonance position for wave scattering by breathers in weakly coupled anharmonic oscillator chains. Analytical results will be compared with numerical data.

4.1 Discrete nonlinear Schrödinger equation

The discrete nonlinear Schrödinger equation (DNLS) has been frequently used to study breather properties due to its tractable form. Wave scattering by breathers in the DNLS has been already studied numerically in [68], where again resonant total reflection has been observed.

The equations of motion for the DNLS are given by

$$i\dot{\Psi}_n = C(\Psi_{n+1} + \Psi_{n-1}) + |\Psi_n|^2\Psi_n \ , \tag{4.1}$$

where n is an integer labelling the lattice sites, Ψ_n is a complex scalar variable and C describes the nearest-neighbor interaction (hopping) on the lattice. The last term in (4.1) yields the requested nonlinearity. For small amplitude waves $\Psi_n(t) = \epsilon e^{-i(\omega_q t - qn)}$ the dispersion relation

$$\omega_q = -2C\cos q \tag{4.2}$$

follows from Eq.(4.1).

Breather solutions have the form

$$\hat{\Psi}_n(t) = \hat{A}_n e^{-i\Omega_b t} \ , \ \hat{A}_{|n|\to\infty} \to 0 \ , \tag{4.3}$$

where the time-independent amplitudes $\hat{A}_n$ can be taken real valued, and the breather frequency $\Omega_b \neq \omega_q$ is some function of the maximum amplitude $\hat{A}_0$. The spatial localization is given by an exponential law $\hat{A}_n \sim e^{-\lambda|n|}$ where $\cosh\lambda = |\Omega_b|/2C$. Thus the breather can be approximated by a single-site excitation if $|\Omega_b| \gg C$. In this case the relation between the single-site amplitude $\hat{A}_0$ and Ω_b becomes $\Omega_b = \hat{A}_0^2$. In the following breather amplitudes for $n \neq 0$ will be neglected, i.e., $\hat{A}_{n\neq 0} \approx 0$. In fact $\hat{A}_{\pm 1} \approx \frac{C}{\hat{A}_0}$. Correction effects will be discussed later.

Perturbing the breather by small fluctuations $\phi_n(t)$

$$\Psi_n(t) = \hat{\Psi}_n(t) + \phi_n(t) \tag{4.4}$$

and substituting this into (4.1) gives, after linearization, the following set of equations:

$$i\dot{\phi}_n = C(\phi_{n+1}+\phi_{n-1}) + \Omega_b\delta_{n,0}(2\phi_0 + e^{-2i\Omega_b t}\phi_0^*) \tag{4.5}$$

with $\delta_{n,m}$ being the usual Kronecker symbol. The general solution to this problem is given by the sum of two channels

$$\phi_n(t) = X_n e^{i\omega t} + Y_n^* e^{-i(2\Omega_b+\omega)t} \ , \tag{4.6}$$

where X_n and Y_n are complex numbers satisfying the following algebraic equations:

$$\begin{aligned} -\omega X_n &= C(X_{n+1}+X_{n-1}) + \Omega_b\delta_{n,0}(2X_0+Y_0) \\ (2\Omega_b+\omega)Y_n &= C(Y_{n+1}+Y_{n-1}) + \Omega_b\delta_{n,0}(2Y_0+X_0) \ . \end{aligned} \tag{4.7}$$

When treating Eqs. (4.7) as an eigenvalue problem the corresponding matrix is nonhermitian due to the nonzero coupling between the variables X_0 and Y_0. This is a consequence of the fact that the linearized phase space flow around a time-periodic orbit of a general Hamiltonian is characterized by a Floquet matrix, which is symplectic. As a result the orbit may be either marginally stable or unstable, i.e., ω may be real or complex. In the following attention will be paid to the transmission properties only, leaving aside the issue of linear dynamical stability. Note here, that in the considered limit of a nearly single-site localized breather solution of the DNLS it is well known that the solution *is* linearly stable [3].

Away from the breather center $n=0$ Eq. (4.5) allows for the existence of plane waves with spectrum ω_q. This spectrum will be dense for an infinite chain. Therefore for propagating waves ω should be set as $\omega \equiv \omega_q$ with some value of q. Then it follows that the X-channel is open and guides propagating waves, while the Y-channel is closed, i.e., its frequency $-(2\Omega_b+\omega_q)$ does not match with the spectrum ω_q.

Instead of solving (4.7) directly, it is better to consider a slightly more general set of equations

$$\begin{aligned} -\omega_q X_n &= C(X_{n+1}+X_{n-1}) - \delta_{n,0}(V_x X_0 + V_a Y_0) \\ (\Omega+\omega_q)Y_n &= C(Y_{n+1}+Y_{n-1}) - \delta_{n,0}(V_y Y_0 + V_a X_0) \ , \end{aligned} \tag{4.8}$$

which reduces to (4.7) for $\Omega = 2\Omega_b$ and $V_x = V_y = 2V_a = -2\Omega_b$.

Note, that for $V_a = 0$ the closed Y channel possesses exactly one localized eigenstate due to a nonzero value of V_y and can be found by assuming that

$$Y_n = Y \mathrm{e}^{-\lambda|n|} \ . \tag{4.9}$$

Using the notation $\omega_L = \Omega + \omega_L^{(y)}$, it is possible to write for $n \neq 0$

$$\omega_L = 2C\cosh\lambda \tag{4.10}$$

and for $n=0$

$$\omega_L = 2C\mathrm{e}^{-\lambda} + V_y \ . \tag{4.11}$$

Taking the difference of these two expressions, we obtain

$$\lambda = \operatorname{arcsinh}\frac{V_y}{2C} \ . \tag{4.12}$$

Substitution this Eq. (4.12) into (4.11) gives

$$\omega_L = \sqrt{V_y^2 + 4C^2} \tag{4.13}$$

and finally

$$\omega_L^{(y)} = -\Omega + \sqrt{V_y^2+4C^2} \ . \tag{4.14}$$

To compute the transmission coefficient the transfer matrix method is used. The boundary conditions are:

$$X_{N+1} = te^{iq} \ , \ X_N = t \ , \ Y_{N+1} = D/\kappa \ , \ Y_N = D \tag{4.15}$$

for the right end of the chain and

$$\begin{aligned} X_{-N-1} = 1 + r \;,\; X_{-N} = e^{iq} + re^{-iq} \;, \\ Y_{-N-1} = F \;,\; Y_{-N} = \kappa F \end{aligned} \tag{4.16}$$

for the left one. Here t and r are the transmission and reflection amplitudes. F and D describe the exponentially decaying amplitudes of the closed Y-channel, where the degree of localization is connected with the coefficient $\kappa \equiv e^{\lambda}$, and λ is defined by the Eq. (4.12)

$$\kappa = \frac{1}{2C}\left[\Omega + \omega_q + \sqrt{(\Omega + \omega_q)^2 - 4C^2}\right] \;. \tag{4.17}$$

The transfer matrix is a 4×4 matrix which is defined by (4.8) at $n = 0$. After finding the solutions for the corresponding four linear equations, the transmission coefficient can be written as

$$\begin{aligned} T = \frac{4\sin^2 q}{\left(2\cos q - a - \frac{d^2\kappa}{2 - b\kappa}\right)^2 + 4\sin^2 q} \;, \\ a = \frac{-\omega_q + V_x}{C} \;,\; b = \frac{\Omega + \omega_q + V_y}{C} \;,\; d = \frac{V_a}{C} \;. \end{aligned} \tag{4.18}$$

This central result allows to conclude that total reflection is obtained when the condition

$$2 - b\kappa = 0 \tag{4.19}$$

is realized. It is equivalent to the condition

$$\omega_q = \omega_L^{(y)} \;, \tag{4.20}$$

which has a very clear physical meaning: perfect reflection takes place when a local mode, originating from the closed Y-channel, is resonating with the spectrum ω_q of plane waves from the open X-channel. The only condition is that the interaction between these channels is nonzero $V_a \neq 0$. Remarkably, the resonance position is not depending on the actual value of V_a, so there is no renormalization. The existence of local modes which originate from the X-channel for nonzero V_x and possibly resonate with the closed Y-channel is evidently *not of any importance*. This resonant total reflection is very similar to the Fano resonance effect, as it is unambiguously related to a local state resonating and interacting with a continuum of extended states. The fact that the resonance is independent of V_a is due to the assumed local character of the coupling between the local mode (originating from the Y-channel) and the open channel. If this interaction has some finite localization length by itself, then the resonance condition (4.20) may be renormalized.

Returning to the case of a DNLS breather at weak coupling, substituting Ω , V_x ,V_y and V_a into (4.18), the expression for the transmission T_b is:

$$T_b = \frac{4\sin^2 q}{\left(\frac{2\Omega_b}{C} - \frac{\Omega_b^2}{2C^2}\frac{\kappa_b}{2C - \cos q\kappa_b}\right)^2 + 4\sin^2 q} \tag{4.21}$$

with

$$\kappa_b = \frac{1}{2C}\left(2\Omega_b + \omega_q + \sqrt{(2\Omega_b + \omega_q)^2 - 4C^2}\right) \;. \tag{4.22}$$

The result is that any breather solution of the DNLS close to the anticontinuous limit provides with perfect reflection close to $q = \pi/2$. In the very anticontinuous limit perfect reflection is obtained precisely at $q = \pi/2$. Indeed, expanding (4.21) in $\frac{C}{\Omega_b}$ and taking into account the lowest order, gives (provided $\frac{C}{2|\Omega_b|} \ll |\cos q|$)

$$T_b \approx \frac{4C^4}{\Omega_b^4}\sin^2 2q \;. \tag{4.23}$$

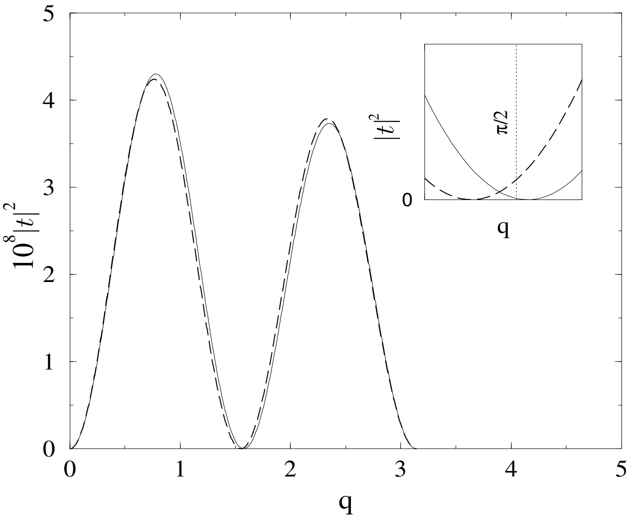

Figure 4.1: Squared transmission amplitude $|t|^2 = T$ for DNLS breather with $C = 0.01$ and $\Omega_b = -1$ versus q. Dashed line: numerically exact result, solid line: analytical result (4.21). Inset - zoom around perfect reflection, where dotted line marks $q = \pi/2$.

At the same time the DNLS breather is linearly stable, so another conclusion is that total reflection is not related to stability or instability of the scattering periodic orbit. The reason for the appearance of total reflection at the anticontinuous limit is that the energy of the closed channel differs by $2\Omega_b$ from the open channel, but the local state of the closed channel differs also by $2\Omega_b$ from the energy of the closed channel, leading to a resonance with the open channel.

In Fig. 4.1 the numerically obtained dependence of the transmission coefficient on q is compared with (4.21) for $C = 0.01$. There is very good agreement, except for a small shift of the true perfect reflection position as compared to $q = \pi/2$.

There are three possibilities to be considered. First, assuming that the single site approximation for the breather solution is correct, one may examine (4.19) or (4.20) which leads in the lowest order to the following shift of the perfect transmission resonance

$$q_{T_b=0} = \frac{\pi}{2} + \frac{C}{2\Omega_b} . \tag{4.24}$$

This shift is solely due to the shift of the local mode (4.14) with C. The predicted shift in q is positive as one sees in the inset of Fig. 4.1, which is opposite to what we observe from numerical simulations (see again inset in Fig. 4.1). Thus the small but nonzero amplitudes $\hat{A}_{\pm 1}$ of the breather solution should be taken into account. A second possibility is that the corrections to the local mode frequency (4.14) coming from the nearest neighbor sites are responsible for the observed discrepancy. It is straightforward to find that these corrections are of order C^4 for the local mode frequency. Thus there is again no way to explain the observed discrepancy. Finally, the only possible explanation is that it is the *nonlocality* of the scattering potential due to the nearest neighbor contribution, which leads to a spread of the interaction between the local mode and the open channel, being responsible for the observed discrepancy. In other words, this nonlocality leads to a shift of the perfect reflection resonance away from the original resonance condition (4.20). This result was tested numerically by reducing the scattering potential originating from the breather to just the central and the two neighboring sites and obtain the correct renormalization values for the resonance position. Indeed such renormalization effects have been discussed for the conductance properties of quantum dots [92].

4.2 Klein-Gordon chain

Now it is possible to apply the same procedure for weakly coupled anharmonic oscillators.

$$\ddot{X}_n = -V'(X_n) + C(X_{n-1} + X_{n+1} - 2X_n) \ , \tag{4.25}$$

where the oscillator potential V possesses one minimum, $V'(0) = 0$ and $V''(0) = 1$. The spectrum of small amplitude plane waves is given by $\omega_q^2 = 1+4C\sin^2(q/2)$ and discrete breather solutions are time-periodic spatially localized solutions of (4.25) with frequency $\Omega_b \neq \omega_q/m$ and nonzero integer m. Again, the weak coupling limit is considered and thus it is possible to assume that the breather is essentially a single-site excitation $\hat{X}_0(t) = \hat{X}_0(t + 2\pi/\Omega_b) \neq 0$ and $\hat{X}_{n\neq 0}(t) \approx 0$. The equations for the linearized phase space flow around the breather solution are then given by

$$\ddot{\epsilon}_n = C(\epsilon_{n-1} + \epsilon_{n+1} - 2\epsilon_n) - \delta_{n,0}V''(\hat{X}_0(t))\epsilon_0 \ . \tag{4.26}$$

By putting $C = 0$ Eq. (4.26) reduces to the Hill equation $\ddot{\epsilon} = -V''(\hat{X}_0(t))\epsilon$. There are two Floquet multipliers for this equation. Due to the fact that $\hat{X}_0(t)$ is time-periodic and satisfies the equation of motion $\ddot{\hat{X}}_0 = -V'(\hat{X}_0)$, both Floquet multipliers are equal to +1.

It is better to rewrite this equation by using the Fourier expansion $V''(\hat{X}_0(t)) = \sum_k v_k e^{ik\Omega_b t}$ and the Floquet representation $\epsilon_0(t) = \sum_k e_k e^{i(\omega+k\Omega_b)t}$ and to arrive at the set of equations

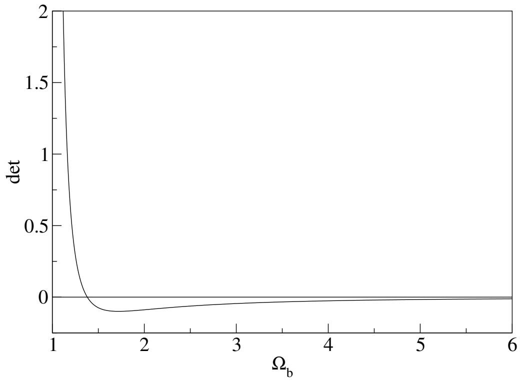

Figure 4.2: Determinant of the system (4.27) without open channel versus frequency Ω_b for $\omega \equiv 1$ and the given potential (4.29). The determinant is equal to zero at $\Omega_b \approx 1.38$.

$$-(\omega + k\Omega_b)^2 e_k = -\sum_{k'} v_{k-k'}(\Omega_b)e_{k'} \ . \tag{4.27}$$

In order to find a nonzero solution of the system (4.27), its determinant should be equal to zero. Following the above results for the DNLS the open channel mode e_0 should be dropped out from (4.27). To solve the remaining homogeneous set of equations, the corresponding determinant has to vanish. For the case $C = 0$ the frequency ω should be equal to one $\omega = 1$. It will lead to a resonance between a local mode of the closed channel with the open one (at zero coupling). It is evident that such a case will not be realized for an arbitrary value of Ω_b. But assuming $\omega = 1$ and scanning Ω_b for a given potential V, it is possible to find a discrete set of Ω_b values for which the resonance occurs.

If the strength of all harmonics is weak, except the zeroth one, then the matrix will be a diagonal one and the resonant condition is $(\omega + m\Omega_b)^2 \approx v_0$. It means that the resonance occurs when the difference between incoming frequency ω and the frequency of the local level $\omega_L = \pm\sqrt{v_0}$ of the *static* potential (open channel) is equal to the multiple breather frequency $m\Omega_b$, i.e.,

$$\omega - \omega_L = m\Omega_b \ . \tag{4.28}$$

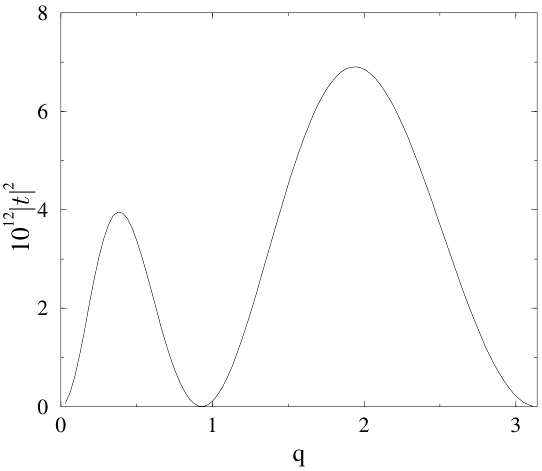

Figure 4.3: Squared transmission amplitude $|t|^2 = T$ versus q for a Klein-Gordon chain breather with $\Omega_b = 1.38$ and $C = 0.001$.

This is exactly the case that was considered in the Refs. [7, 111, 74, 86] with a $\delta-$oscillating potential and, therefore, explains their results, which are valid only in the limit of the weak coupling between the open and closed channels.

Thus in dinstintion to the DNLS case, a Klein-Gordon chain at infinitesimally weak coupling will lead to perfect reflection of waves by breathers only for a selected discrete set of breather frequencies. However, increasing the coupling C will transform each of these values into stripes on the real axis, which will continue to increase. This follows from the fact that the width of ω_q increases linearly with C because it belongs to a continuous part of the spectrum, but the renormalization of eigenvalues belonging to some discrete part of the spectrum will be proportional to C^2.

In order to demonstrate the validity of our approach, the following potential is chosen

$$V(x) = \frac{1}{2}x^2 + \frac{1}{3}x^3 + \frac{1}{4}x^4 \tag{4.29}$$

and we search for frequencies Ω_b of oscillations in $V(x)$ such that $\omega = 1$ makes the determinant corresponding to (4.27) vanishing. The result is $\Omega_b \approx 1.38$ (see Fig. 4.2). The prediction then is that for small C a breather with Ω_b close to this value yields perfect reflection. The numerical result for the transmission is shown in Fig 4.3 for $C = 0.001$.

Indeed, there is a perfect reflection around $q \approx 1$, as was expected.

5 Resonant soliton scattering

Concerning the previous chapters, a DB can be represented in the scattering problem as a set of open and closed channels. There are only two important things which can affect the transmission by a DB. One of them are local levels, generated by the DB itself, which lead to the possibility of *perfect transmission*. And others are local levels, generated by the subset of closed channels, which manifest themselves through the *perfect reflection*. All these phenomena were observed numerically for the scattering of small amplitude monochromatic plane waves by DBs in the linear limit.

The next step is to study the influence of nonlinearity. It becomes important when the amplitude of incoming waves is sufficiently large. But due to the nonlinearity there is a possibility to form a small amplitude moving *soliton* in some systems. And this immediately leads to the *soliton-soliton* interaction problem . There are many effects of this interaction such as full and partial propagation and reflection and pinning of solitons. But they are not fully understood.

Here the attempt to study soliton-soliton (or better to say 'mode-mode') interaction is made by taking, instead of the DB itself, different scattering centers, which model the desired level structure.

One of the systems, which supports the small amplitude travelling soliton solution, is the DNLS model. In the previous chapter it was shown, that the DB in this model generates one open and exactly one closed channels. From this point of view a Fano-Anderson impurity (see Appendix D) can be used instead of the DB in the scattering problem. The presence of such an impurity leads to the *resonant backscattering* of solitons. When the role of closed channels is not so important, the DB can be considered similar to the static scattering potential. Then it is possible to observe the perfect transmission. The replacement of a DB by a two sites defect allows to observe the *resonant transmission* of soliton.

5.1 Soliton backscattering

Let us add a Fano-Anderson impurity (see Appendix D) to the DNLS equation

$$\begin{aligned} i\dot{\phi}_n &= C(\phi_{n-1}+\phi_{n+1}) + \lambda|\phi_n|^2\phi_n + \epsilon\varphi\delta_{n0} \ , \\ i\dot{\varphi} &= -E\varphi + \epsilon\phi_0 \ . \end{aligned} \tag{5.1}$$

For $\epsilon = 0$, the first equation in (5.1) is the DNLS equation. It supports the small amplitude moving soliton solution of the continuous NLS for sufficiently large time

$$\phi_n(t) \approx \frac{\eta}{2}\sqrt{\frac{\lambda}{2C}}\exp\left[i(\frac{V}{2C}n - (\omega_s+2)Ct)\right]\operatorname{sech}\left[\frac{\eta\lambda}{4C}(n-Vt)\right] \ , \tag{5.2}$$

where V is the velocity of the soliton, $\omega_s = \left(4C^2\right)^{-1}(V^2 - \eta^2\lambda^2/4)$ is its intrinsic frequency, and η is the amplitude [70]. The velocity of soliton V determines the effective wave number $q_s = \frac{V}{2C}$ of its spectral decomposition. The soliton solution can be considered as a weighted superposition of linear waves with the wave numbers from some interval centered around q_s. The width of this interval in q-space is given by

$$\Delta q_s = \frac{\eta\lambda \operatorname{arccosh}(2)}{\pi C} \ . \tag{5.3}$$

There are two characteristic time scales, which describe the scattering of the soliton (5.2) by a Fano-Anderson impurity. One of them is the time of interaction of the soliton and the impurity,

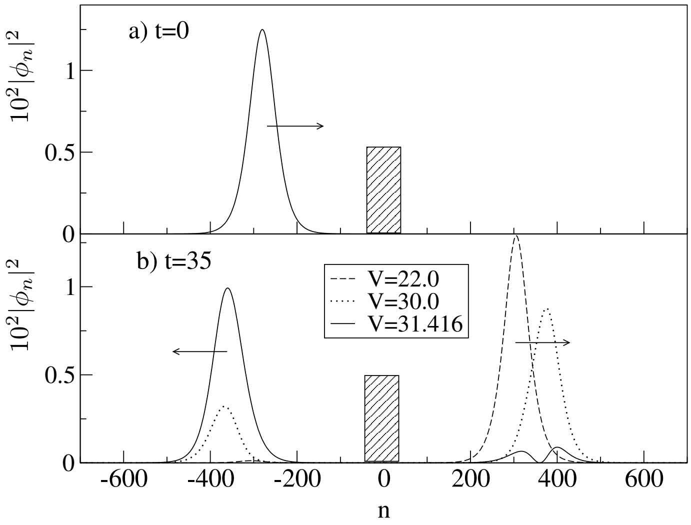

Figure 5.1: Initial (a) and after interaction (b) profiles for three values of velocities are shown. The chosen parameters are: $q_F = \frac{\pi}{2}$, $C = 10.0$, $\epsilon = 4.0$, $\eta = \lambda = 1.0$ After interaction there are two soliton-like excitations, which move in opposite direction with the same velocity.

which is given by the ratio between the width of the soliton in real space $1/\Delta q_s$ and its velocity V

$$\tau_{int} = \frac{1}{\Delta q_s V} \ . \tag{5.4}$$

The mode-mode interaction of the waves composing the soliton is defining the second time scale. It can be obtained from the time of the dispersion of the wave packet (5.2) in the linear system (5.1), when $\lambda = 0$. Using the representation of the soliton as a bunch of phonons, this time can be estimated, in analogy with the previous one (5.4), as

$$\tau_{dis} = \frac{1}{\Delta q_s \Delta v_q} \ , \tag{5.5}$$

where v_g is a group velocity $v_g(q) = 2C \sin q$ and $\Delta v_g = v_g(q_s + \Delta q_s/2) - v_g(q_s - \Delta q_s/2) = 4 \sin \frac{\Delta q_s}{2} \cos q_s$ is the relative velocity between the faster and slower waves composing the soliton. When $\tau_{int} \ll \tau_{dis}$, the mode-mode interaction does not play a significant role during the scattering of the soliton. The soliton can be thus considered as a set of noninteracting plane waves. The transmission of each wave is given by (see Appendix D)

$$T = \left[1 + \frac{1}{4C^2 \sin^2 q} \frac{\epsilon^4}{(E + \omega_q)^2} \right]^{-1} \ . \tag{5.6}$$

If now the condition

$$\Delta q_s < \Delta q \ , \tag{5.7}$$

where $\Delta q = \frac{\epsilon^2}{2C^2 \sin^2 q_F}$ (see Appendix D), is satisfied, i.e. essentially all the waves in the soliton reflect nearly totally, then we expect that the soliton itself will be totally reflected. To check this statement, numeric simulations were done. The transmission coefficient can be computed by using the conservation laws. In this case the conservation law of number of particles $\sum_n |\phi_n|^2$ is used. The soliton is put from the left hand side with some positive velocity V. After the interaction the soliton is split into two soliton-like parts which move in opposite directions from the defect (see Fig. 5.1).

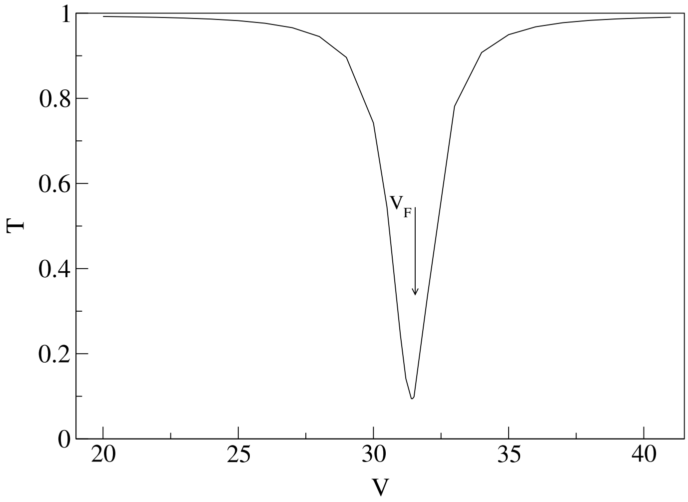

Figure 5.2: This figure represents the dependence of transmission of soliton on its velocity V through the local defect for parameters as in Fig. 5.1. The minimum locates at $V_F = 2Cq_F$.

The transmission coefficient is then defined as the ratio between the norm of the transmitted part and the initially launched soliton:

$$T = \frac{\sum\limits_{n>0} |\phi_n(t^*)|^2}{\sum\limits_{n} |\phi_n(0)|^2} \tag{5.8}$$

where $t^* \gg \tau_{int}$.

The energy E_F is chosen such, that $q_F = \frac{\pi}{2}$. For this value of wave number the τ_{dis} goes to infinity and the soliton does not disperse at all in the linear system. The condition (5.7) can be written as

$$\eta\lambda < \frac{\epsilon^2}{C \sin^2 q_F} \ . \tag{5.9}$$

In order to satisfy this condition other parameters were taken as $\eta = \lambda = 1.$, $C = 10.$ and $\epsilon = 4.$ The result is shown in Fig. 5.2

There is a minimum in the dependence of the transmission on soliton velocity exactly at $V_F = 2Cq_F$ as predicted. The minimum does not reach total zero value. It is due to the finite width Δq_s, i.e. there are always some plane waves which form the soliton but do not fully backscatter.

But mode-mode interactions become important when $\tau_{int} \geq \tau_{dis}$. By shifting q_F to the spectrum edge it is possible to vary τ_{dis}, preserving all other parameters. The Fano resonance is observable until $\tau_{int} \approx \tau_{dis}$. Decreasing τ_{dis} more, the Fano minimum in the $T(V)$ curve becomes less and less pronounced and disappears at some critical value of the wave number. As an example, we found numerically that for $C = \eta = \lambda = \epsilon = 1.0$, when the condition of smallness τ_{dis} is fulfilled, the Fano resonance disappears at $q \approx 1.0$.

This result implies that the plane wave modes which make up the soliton, loose their resonant backscattering features. This is not unexpected, as the interaction of many modes with each other can be interpreted as a many channel scattering problem (as opposed to many single channel scattering problems in the absence of mode-mode interaction). Many channel scattering problems are known to have less pronounced Fano resonance features, since Fano resonances are inherently based on keeping phase coherence in order to provide with destructive interference. This phase coherence is of course less pronounced due to the mode-mode interaction, which leads to a *dephasing*.

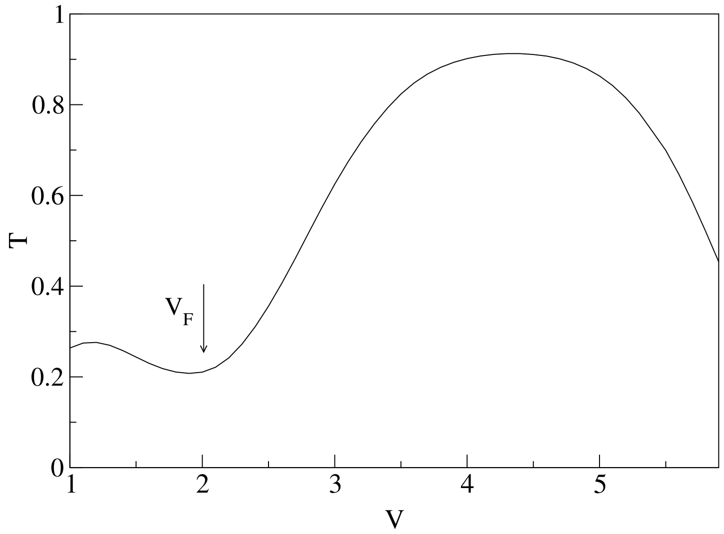

Figure 5.3: The dependence of the transmission of the soliton on its velocity V through the Fano defect for the following parameters $C = \eta = \lambda = \epsilon = 1.0$ and $q = 1$. The minimum at $V_F = 2Cq_F$ does not reach zero and is rather smooth.

5.2 Soliton resonant transmission

The propagation of the soliton through a single site defect has been already studied in many papers [60, 50, 16, 59, 20]. This type of defect provides a maximum of transmission of linear waves at $q = \frac{\pi}{2}$ being always less then one. By increasing the size of the defect up to two there is a possibility for perfect transmission. Indeed, the transmission coefficient for the system

$$i\dot{\phi}_n \quad = \quad C(\phi_{n-1} + \phi_{n+1}) + \delta_{n,0}\epsilon_0\phi_n + \delta_{n,1}\epsilon_1\phi_n \tag{5.10}$$

for the case when $\epsilon_0 = \epsilon_1 \equiv \epsilon$ is given by

$$T = \frac{4C^4 \sin^2 q}{\epsilon^2(\epsilon - 2C\cos q)^2 + 4C^4\sin^2 q} \; . \tag{5.11}$$

The perfect transmission exists when $\epsilon \leq 2C$ at $q' = \arccos(\frac{\epsilon}{2C})$. For the small value of the strength of the impurity $\epsilon \ll 2C$ the perfect transmission takes place around $q = \frac{\pi}{2}$. By increasing $\epsilon \to 2C$ the value of q' moves towards zero. When $\epsilon = 2C$ perfect transmission occurs at the edge of the phonon band at $q' = 0$ and disappears for larger values. Therefore, it is possible to vary the width of the resonance by using the strength of the impurity ϵ.

The transmission of the soliton (5.2) through such a defect

$$i\dot{\phi}_n \quad = \quad C(\phi_{n-1} + \phi_{n+1}) + \lambda|\phi_n|^2\phi_n + \delta_{n,0}\epsilon_0\phi_n + \delta_{n,1}\epsilon_1\phi_n \tag{5.12}$$

was computed numerically for different values of parameters. The results are in a very good agreement with the formula (5.11). The only difference is the value of the maximum. When the parameters are chosen such that $\tau_{int} \ll \tau_{dis}$ and it is possible to neglect the mode-mode interaction, there is a perfect transmission of the soliton, as predicted by the formula (5.11). And when the mode-mode interaction becomes stronger $\frac{\tau_{int}}{\tau_{dis}} \geq 1$, the maximum of transmission does not reach unity, but its position locates *exactly* at q'. Far from the resonance value q', the transmission coefficient is the same as given by (5.11).

The above considerations show that it is possible to observe *resonant transmission* (as opposed to backscattering) of solitons with specific velocity values. Moreover, the mode-mode interaction does not destroy this resonance (as it happens for the backscattering).

Finally, such special properties of the propagation of a soliton through different defects as resonant backscattering and resonant transmission are understood by analyzing the scattering

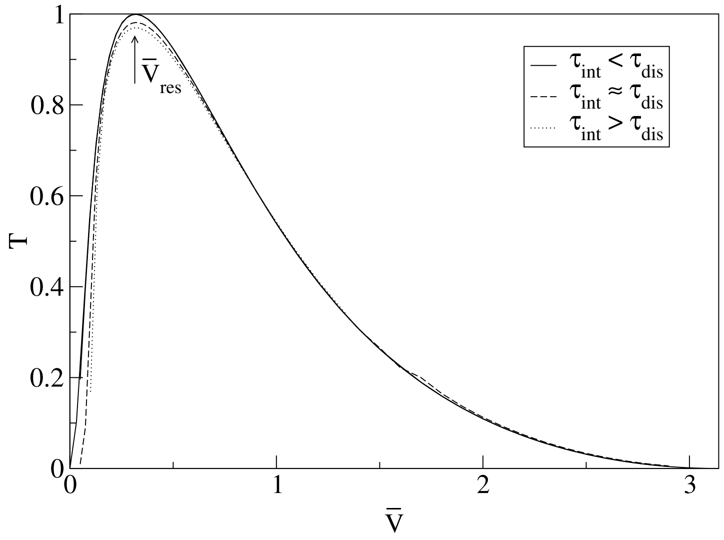

Figure 5.4: A typical dependence of the transmission coefficient T for the soliton in the model (5.12) on V for $\eta = \lambda = 1.$ and (a) $\epsilon = 19$ and $C = 10$ (solid line); (b) $\epsilon = 3.8$ and $C = 2$ (dashed line); (c) $\epsilon = 2.85$ and $C = 1.5$ (dotted line) In this figure the normalized velocity $\bar{V} = \frac{V}{2C}$ is used. In all the cases, the position of the resonance is fixed at $\bar{V}_{res} \approx 0.318$. Note here, that the solid line is *exactly* described by formula (5.11)

.

of plane waves by these defects. It gives a very good description for weak mode-mode interaction. When the interaction becomes stronger one of these phenomena (resonant backscattering) disappears due to dephasing while the other still survives.

Summary of Part I

Discrete breathers can be represented in the scattering problem by a set of open and closed channels, due to time periodicity. Plane waves can freely propagate in open channels only. Closed channels become active at the core of DBs and interference phenomena can take place. In general this leads to a suppression of transmission, compared to a static scattering potential. Moreover, in some cases a *destructive* interference (perfect reflection) was observed. It happens when local levels, generated by a subset of closed channels, are inside the phonon band. These have a resonant behavior and are similar to the Fano resonance, but the position of zeros does not coincide with the positions of local levels. There are renormalizations due to the finite size of DBs. In the case of weak coupling, these renormalizations can be neglected and it is possible to *predict* the appearance of Fano resonance in a transmission line by using the method described in Chapter 5. This type of resonances does not affect the stability of breathers. At the same time, DBs are fully transparent for some plane waves. This is due to the existence of local levels of the DB itself.

All above phenomena are valid for soliton scattering on defects similar to DBs in the presence of nonlinearity. But in this case mode-mode interaction should be taken into account. When it is weak resonant backscattering and resonant transmission of solitons are observed. For strong interaction only resonant transmission occurs, while backscattering looses its resonant feature. By increasing the mode-mode interaction, phase coherence becomes less pronounced and destructive interference does not take place. This picture is helpful in order to understand a realistic soliton-soliton interaction.

Part II

Inverse spectroscopy

Motivation

The concept of DBs is valid for dissipative systems as well. Breathers preserve their main properties such as time periodicity and spatial localization. In the phase space they are still periodic orbits, which become attractors. Each breather possesses a basin of the attraction and therefore is separeted from other breather solutions.

One of the most investigated dissipative systems is a network of coupled Josephson junctions. DBs were observed numerically and experimentally in the ladder geometry [115, 13]. This type of geometry implies a plasmons multiband structure. There are many different types of DBs in Josephson junction ladders [12] for certain boundary conditions. Due to exponential localization and presence of the dissipation it is possible to assume that the tails of DBs are almost at rest and analyze the properties of DBs by paying attention to the core only. It was done in Ref. [11], were the whole ladder was reduced to a single plaquette. Such a small size system allows to do some analytical investigation for regions of the existence and stability, different types of resonances and their dependence on a magnetic field [27]. This consideration is in a very good agreement with experimental observations [94].

The second part of the present work is devoted to the analysis of the properties of DBs in large Josephson junction ladders, where the dynamics of the tails can be important. The interaction between DBs and phonons is analyzed by tuning the frequency of DBs exactly into resonances. The analysis shows that there are three types of resonances: primary, parametric and combinational ones, which were also observed and classified in experiments [102]. Due to the presence of the dissipation DBs can survive resonances and generate extended excitations, which can be detected at the edge, for example, by measuring the power. This is the so-called *inverse spectroscopy* method. When these resonances are very strong, DBs become unstable. By loosing the stability the DB switches to other attractors, which can be different DBs again.

1 Josephson junctions: basic facts

There are different models of the single Josephson junction [75]. Here only the Resistively Shunted Junction model will be used. A comparison of different models can be found in Ref. [114].

1.1 Josephson's laws

A Josephson junction manifests the superconductivity phenomenon - the existence of nonzero current without a voltage drop. The physical origin of the effect lies in the quantum nature of the superconducting state, where electrons form a condensate of Cooper pairs. Each Cooper pair consists of two electrons of opposite spins and momenta. It obeys the Bose-Einstein statistics and at low temperatures the ground state has a macroscopic occupation number. All the Cooper pairs in this state are described by one macroscopic wave function $|\phi >= \sqrt{n}e^{i\theta}$, where $\sqrt{n}$ is the particle density of the Cooper pairs.

A Josephson junction consists of two superconductors which are connected via a *weak link*. Therefore two wave functions may overlap and generate a tunnelling current. Josephson found that the *supercurrent* I_s is a function of the phase difference $\varphi = \theta_1 - \theta_2$ of the two superconductors

$$I_s = I_c \sin(\varphi), \tag{1.1}$$

where I_c is the critical value of current, above which there is no supercurrent. Josephson also predicted that a finite voltage drop across the tunnel junction induces a time-varying phase difference described by the ac Josephson equation as

$$\frac{d\varphi}{dt} = \frac{2eV}{h} \; . \tag{1.2}$$

From this equation (1.2) one can see that φ could be a nonzero constant for $V = 0$ and, therefore, generates some value of $I_s \neq 0$. These are the two basic equations which describe the Josephson effect.

1.2 Single Josephson junction

The whole current which flows through a single Josephson junction, in the frame of Resistively Shunted Junction (RSJ) model, can be divided into three parts

$$I = C\frac{dV(t)}{dt} + \frac{V(t)}{R} + I_s \sin(\varphi), \tag{1.3}$$

where CdV/dt is the displacement current through the capacitor C, $V(t)/R$ is the current through the resistor R and $I_s \sin(\varphi)$ is the Josephson supercurrent. $V(t)$ is the actual voltage drop across the junction. By using Eq. (1.2) the expression (1.3) can be transformed into an equation for the phase φ

$$I = \frac{Ch}{2e}\frac{d^2\varphi}{dt^2} + \frac{h}{2eR}\frac{d\varphi}{dt} + I_s \sin(\varphi). \tag{1.4}$$

It is convenient to introduce the dimensionless variables:

$$\tau = \omega_J t \; , \quad \alpha = 1/(\omega_J RC) \; , \tag{1.5}$$

where

$$\omega_J = \sqrt{\frac{2eI_s}{hC}} \tag{1.6}$$

is the plasma frequency. By this choice Eq. (1.4) can be written as

$$\ddot{\varphi} + \alpha\dot{\varphi} + \sin(\varphi) = \gamma, \tag{1.7}$$

where $\gamma = I/I_s$ is the normalized dc bias.

1.2.1 Mechanical model

Formally φ can be treated as the angle of the pendulum in the gravitation field with damping α under the influence of an external constant torque γ. Therefore a mechanical analog can be used in order to gain better insight into the behavior of the Josephson device.

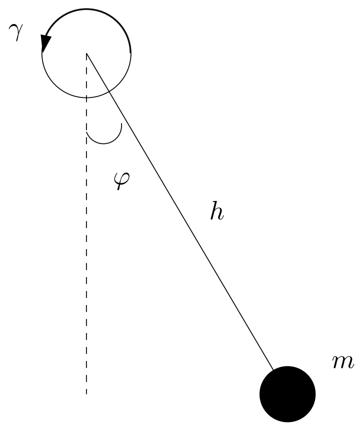

Figure 1.1: Schematic view of a pendulum model.

1.2.2 Overdamped limit

Let us consider the case of small capacitance $C << 1$. It means that $\alpha >> 1$ and we can neglect the term with the second derivative on time

$$\alpha\dot{\varphi} + \sin(\varphi) = \gamma. \tag{1.8}$$

This equation can be solved explicitly. For the case $\gamma > 1$ we obtain one attractor

$$\varphi(\tau) = 2\arctan\left[\sqrt{\frac{\gamma^2-1}{\gamma^2}}\tan(\frac{\pi\tau}{T}) - \gamma\right]. \tag{1.9}$$

It is a periodic solution with the period T

$$T = \frac{2\pi\alpha}{\sqrt{\gamma^2-1}}. \tag{1.10}$$

Thus, the first derivative on time $d\varphi(t)/dt$ is also a periodic function with the same period T. By using the ac Josephson effect $V(t) \propto \frac{d\varphi(t)}{dt}$, one can conclude that if an external dc bias γ through the junction exceeds the critical current $\gamma > 1$, it causes the voltage $V(t)$ to appear across the junction, which periodically oscillates in time around a nonzero mean value. This phenomenon is called Josephson radiation [91]. The dc voltage drop V across the Josephson junction is proportional to the time average of $d\varphi/dt$

$$\bar{\dot{\varphi}} = \frac{1}{T}\int_0^T \frac{d\varphi}{dt}\,dt = \frac{1}{T}(\varphi(T) - \varphi(0)) = \frac{2\pi}{T} \tag{1.11}$$

or in other words $V = \bar{\dot{\varphi}} = \Omega$, where $\Omega = 2\pi/T$ is the frequency of the solution (1.9). Therefore

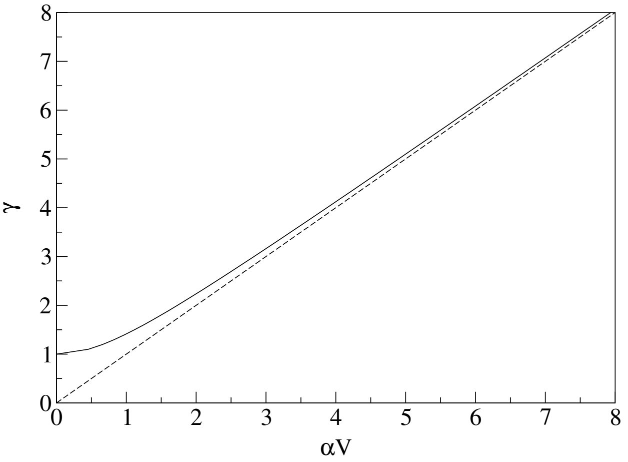

Figure 1.2: $I - V$ characteristic for overdamped case.

the relation between current and voltage is

$$V = \frac{\sqrt{\gamma^2 - 1}}{\alpha} \tag{1.12}$$

For large values of the current $\gamma >> 1$ it shows the normal Ohm's law $V \approx \gamma/\alpha$. When the dc bias $\gamma \to 1$, the dc voltage drop disappears: $V \to 0$ and $\varphi = \frac{\pi}{2}$. It means that in this limit there is only a supercurrent flowing through the junction, which equals to 1.

1.2.3 Phase space structure

For intermediate values of α solutions of the Eq. (1.7) can not be written explicitly and it is more convenient to study it by analyzing the phase space structure. To do this let us replace Eq. (1.7) by two equivalent equations of the first order

$$\left\{ \begin{array}{l} \dot{\varphi} = p \\ \dot{p} = \gamma - \alpha p - \sin\varphi \end{array} \right. , \tag{1.13}$$

The state of the system (1.13) is represented for any given time by a point in the $\varphi - p$ plane. For a particular initial condition, the system (1.13) generates a trajectory. For different initial conditions $\varphi(0)$ and $p(0)$ there are different trajectories which do no intersect at any time. A closed curve corresponds to a periodic solution, a point at which $\dot{\varphi} = \dot{p} = 0$ is an equilibrium point (constant solution). By linearizing the phase space flow around a certain solution we can obtain information about the linear stability of this solution.

Note here that all points which differ by 2π in the variable φ are equivalent. Therefore, it is more convenient to consider the phase space on a *cylinder*. Each closed trajectory can be characterized by a *winding number* m, which counts how many times a trajectory is encircling the cylinder $\varphi(T) = \varphi(0) + 2\pi m$.

Therefore there are two types of closed trajectories with zero and nonzero winding number. In terms of mechanical analogy a trajectory with zero winding number corresponds to an oscillatory motion of the pendulum and a trajectory with nonzero winding number corresponds to a rotary motion.

One restriction is that only positive values of the dc bias $\gamma > 0$ will be considered, because for negative values of γ we can apply the transformation $\gamma \to -\gamma$, $\varphi \to -\varphi$ and $p \to -p$ which does not change the system (1.13). It means that for negative dc bias it is enough just to change the sign of the solution $\varphi(\gamma) = -\varphi(-\gamma)$.

Now, let us find the equilibrium points of the system (1.13). The are determined by the set of equations

$$p = 0, \quad \gamma - \alpha p - \sin(\varphi) = 0. \tag{1.14}$$

For $0 < \gamma < 1$ there are two solutions $\varphi_1 = \varphi^*$ and $\varphi_2 = \pi - \varphi^*$, where $\varphi^* = \arcsin(\gamma)$. One of them is stable and another is not. The system under consideration is dissipative, non-conservative. It means that the stable equilibrium point is a stable *focus* and therefore there is no closed trajectory with zero winding number. When $\gamma > 1$ there are no solutions of Eq. (1.14). From this fact we can conclude that again for $\gamma > 1$ there is no closed trajectory with zero winding number. Hence, there is no closed path with zero winding number at all in this system. Therefore, there are only closed trajectories with *nonzero* winding numbers. It was shown, that they exist always when $\gamma > 1$ [1]. For $0 < \gamma < 1$ there is a threshold α_0 such that for $\alpha < \alpha_0$ there is a unique periodic solution and for $\alpha > \alpha_0$ no periodic motions. The closed trajectory disappears for $\alpha = \alpha_0$ when it merges with the separatrix loop that encircles the cylinder.

It is possible to estimate the value of α_0 by the means of the energy balance consideration. Let us multiply Eq.(1.7) with $\dot\varphi$ and integrate over time. It gives

$$\frac{1}{2}\dot\varphi^2 + (1 - \cos\varphi) - E = \gamma \int d\varphi - \alpha \int \dot\varphi \, d\varphi \, . \tag{1.15}$$

The energy balance assumes that the r.h.s. of eq.(1.15) should vanish after integrating over one period T or over φ from 0 to 2π

$$\alpha \int_0^{2\pi} \dot\varphi \, d\varphi = 2\pi\gamma \, . \tag{1.16}$$

The l.h.s. of eq.(1.15) can be treated as the energy of a nonlinear oscillator. Using the fact that for the separatrix $E = 2$, we find

$$\dot\varphi = \sqrt{2(1 + \cos\varphi)}. \tag{1.17}$$

Substituting (1.17) into (1.16) and taking the integral gives

$$8\alpha_0 = 2\pi\gamma. \tag{1.18}$$

Usually, when the $I - V$ characteristics is scanned, the dc bias γ is changed and all other parameters are fixed, i.e. $\alpha = const$ and the expression (1.18) can be rewritten as

$$\gamma_r = \frac{4\alpha}{\pi} \, , \tag{1.19}$$

which is called *retrapping* current and has a very physical meaning - it is the current when the junction switches from the resistive state to the superconducting one ($V \to 0$). If α is chosen such that the relation $\frac{4\alpha}{\pi} < 1$ is valid, there is an interval for γ where two stable attractors, a limit cycle and a fixed point, coexist. For $\gamma > 1$ there is a limit cycle and for $\gamma < \gamma_r$ there is a fixed point only. The existence of the bistable region leads to the appearance of the hysteresis loop in the $I - V$ curve.

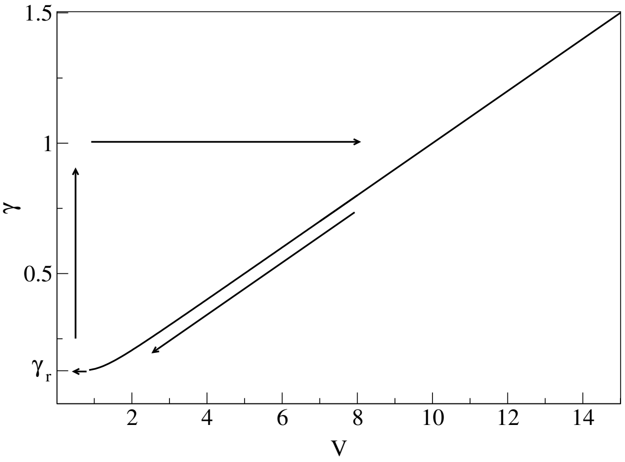

Figure 1.3: $I - V$ characteristics for a SJJ for the damping $\alpha = 0.1$ (underdamped case). Arrows show the hysteresis in the region of bistability.

1.3 Josephson junction ladders

Taking a single Josephson junction as a basic element it is possible to construct different circuits. On of the simplest is a dc SQUID (*Superconducting Quantum Interference Device*) - a cell which consists of two junctions which are connected in parallel. Another possibility is to take N junctions instead of two. This structure is called a Josephson junction *array* (JJA). All junctions are assumed to be equivalent and under the same dc bias I_b. Josephson junction arrays show different dynamics: phase locking of moving fluxons with plasma waves, parametric instabilities, Fiske modes and Eck peaks.

In this section the dynamics of Josephson junction ladders (JJLs) is considered. It has a slightly different geometry compared to the array with additional horizontal junctions. The critical current of the horizontal junction I_c^H may be different from I_c^V. The value $\eta = I_c^H / I_c^V$ is the anisotropy parameter of the ladder.

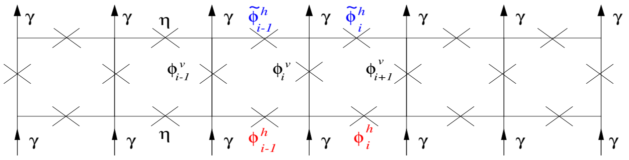

Figure 1.4: Josephson junction ladder. Crosses mark the individual junctions. Arrows indicate the direction of external current flow (dc bias γ).

1.3.1 Dynamics

The dynamics of each junction is described by

$$\begin{aligned}
\ddot{\phi}^v_n + \alpha\dot{\phi}^v_n + \sin\phi^v_n &= I^v_n, \\
\ddot{\phi}^h_n + \alpha\dot{\phi}^h_n + \sin\phi^h_n &= \frac{1}{\eta} I^h_n, \qquad (1.20) \\
\ddot{\tilde{\phi}}^h_n + \alpha\dot{\tilde{\phi}}^h_n + \sin\tilde{\phi}^h_n &= \frac{1}{\eta}\tilde{I}^h_n,
\end{aligned}$$

where ϕ^v_n, ϕ^h_n and $\tilde{\phi}^h_n$ are the vertical, upper and lower horizontal junctions in the nth cell. Currents I^v_n, I^h_n and $\tilde{I}^v_n$ are measured in units of the critical current of the vertical junction

I_c^V. The positive current direction is chosen to be directed from bottom to top and from left to right. The currents flowing through Josephson junctions are governed by the Kirchhoff laws

$$\begin{aligned}\gamma &= I_n^v + I_n^h - I_{n-1}^h,\\ \gamma &= I_n^v - \tilde{I}_n^h + \tilde{I}_{n-1}^h\end{aligned} \tag{1.21}$$

and the flux quantization law in each cell

$$-\beta_L I_n^m = \phi_n^h + \phi_{n+1}^v - \tilde{\phi}_n^h - \phi_n^v, \tag{1.22}$$

where the mesh current I_n^m and the normalized inductance of the cell β_L are introduced.

By subtracting Kirchhoff equations (1.21) from each other, one obtains

$$I_n^h + \tilde{I}_n^h = I_{n-1}^h + \tilde{I}_{n-1}^h \equiv C, \tag{1.23}$$

where C is a constant for a whole ladder. This constant corresponds to the net difference between the currents flowing through the upper and lower horizontal junctions. For an open ladder of finite size, C is zero. For a ladder of annular geometry with periodic boundary conditions C may be nonzero and corresponds to the flux "trapped" by the ladder ring. In the following we will consider the case of a finite open ladder with $C = 0$. It implies that $\tilde{I}_n^h = -I_n^h$. More over, it gives the following relation between mesh and horizontal currents

$$I_n^m = I_n^h. \tag{1.24}$$

The Kirchhoff law can be rewritten now as

$$I_n^v = \gamma - I_n^m + I_{n-1}^m. \tag{1.25}$$

Inserting relation (1.25), (1.24) and (1.22) into Eq. (1.20) we get the set of coupled differential equations

$$\begin{aligned}\ddot{\phi}_n^v + \alpha\dot{\phi}_n^v + \sin\phi_n^v &= \gamma + \frac{1}{\beta_L}(\triangle\phi_n^v + \nabla\phi_{n-1}^h - \nabla\tilde{\phi}_{n-1}^h)\\ \ddot{\phi}_n^h + \alpha\dot{\phi}_n^h + \sin\phi_n^h &= -\frac{1}{\eta\beta_L}(\nabla\phi_n^v + \phi_n^h - \tilde{\phi}_n^h)\\ \ddot{\tilde{\phi}}_n^h + \alpha\dot{\tilde{\phi}}_n^h + \sin\tilde{\phi}_n^h &= \frac{1}{\eta\beta_L}(\nabla\phi_n^v + \phi_n^h - \tilde{\phi}_n^h)\,,\end{aligned} \tag{1.26}$$

where the notations $\triangle f_n \equiv f_{n-1} - 2f_n + f_{n+1}$ and $\nabla f_n \equiv f_{n+1} - f_n$ are used. It is a quasi 1D system with three degrees of freedom per cell.

The ground state of the system (1.26) is when all horizontal junctions are at rest with zero current and all vertical junctions are in the superconducting state (similar to a single junction)

$$\phi_n^{*h} = \tilde{\phi}_n^{*h} \equiv 0\,, \quad \phi_n^{*v} = \arcsin\gamma\,. \tag{1.27}$$

1.3.2 Dispersion relation

The next step of the analysis is to get the spectrum of small amplitude electromagnetic waves (EW's) which can propagate through the ladder. To find it the Eqs. (1.26) should be linearized around the ground state (1.27) by decomposing the Josephson phases into the particular form:

$$\phi_n^v = \phi_n^{*v} + \varphi_n^v\,,\ \phi_n^h = \phi_n^{*h} + \varphi_n^h\,,\ \tilde{\phi}_n^h = \tilde{\phi}_n^{*h} + \tilde{\varphi}_n^h\,, \tag{1.28}$$

where φ_n^v, φ_n^h and $\tilde{\varphi}_n^h$ describe the small amplitude EWs. Substituting these expressions into system (1.26) and using the smallness of the amplitude of EWs, gives

$$\begin{aligned}\ddot{\varphi}_n^v + \alpha\dot{\varphi}_n^v + \sqrt{1-\gamma^2}\varphi_n^v &= \frac{1}{\beta_L}(\triangle\varphi_n^v + \nabla\varphi_{n-1}^h - \nabla\tilde{\varphi}_{n-1}^h)\\ \ddot{\varphi}_n^h + \alpha\dot{\varphi}_n^h + \varphi_n^h &= -\frac{1}{\eta\beta_L}(\nabla\varphi_n^v + \varphi_n^h - \tilde{\varphi}_n^h)\\ \ddot{\tilde{\varphi}}_n^h + \alpha\dot{\tilde{\varphi}}_n^h + \tilde{\varphi}_n^h &= \frac{1}{\eta\beta_L}(\nabla\varphi_n^v + \varphi_n^h - \tilde{\varphi}_n^h)\,.\end{aligned} \tag{1.29}$$

In order to get dissipationless propagation one should assume that the damping is rather small $\alpha \ll 1$, therefore it can be can neglected. By taking the Josephson phases φ_n^v, φ_n^h and $\tilde{\varphi}_n^h$ in the form

$$\begin{pmatrix} \varphi_n^v \\ \varphi_n^h \\ \tilde{\varphi}_n^h \end{pmatrix} = e^{i(qn+\omega t)} \begin{pmatrix} A_v \\ A_h \\ \tilde{A}_h \end{pmatrix} , \tag{1.30}$$

by substituting them into (1.29) provides with the set of three algebraic equations

$$\begin{aligned} -\omega^2 A_v + \sqrt{1-\gamma^2} A_v &= \frac{1}{\beta_L}((2\cos q - 2)A_v + (1-e^{-iq})(A_h - \tilde{A}_h)) \\ -\omega^2 A_h + A_h &= -\frac{1}{\eta\beta_L}((e^{iq}-1)A_v + A_h - \tilde{A}_h) \\ -\omega^2 \tilde{A}_h + \tilde{A}_h &= \frac{1}{\eta\beta_L}((e^{iq}-1)A_v + A_h - \tilde{A}_h) \, . \end{aligned} \tag{1.31}$$

It is more convenient to introduce new variables

$$\begin{aligned} A^+ &= \frac{1}{2}(A_h + \tilde{A}_h) \, , \\ A^- &= \frac{1}{2}(A_h - \tilde{A}_h) \end{aligned} \tag{1.32}$$

and rewrite (1.31)

$$\begin{aligned} -\omega^2 A_v + \sqrt{1-\gamma^2} A_v &= \frac{1}{\beta_L}((2\cos q - 2)A_v + (1-e^{-iq})A^-) \\ -\omega^2 A^- + A^- &= -\frac{1}{\eta\beta_L}((e^{iq}-1)A_v + 2A^-) \\ -\omega^2 A^+ + A^+ &= 0 \, . \end{aligned} \tag{1.33}$$

At last the system of three linear homogeneous equations (1.33) is obtained. One can see that A^+ is decoupled from A_v and A^-.

This system possesses the trivial solution $A_v = A^- = A^+ \equiv 0$. In order to find a nonzero solution we put the determinant of the system (1.33) to zero. As a result it will give a dispersion relation $\omega(q)$. As was mentioned above there are three degrees of freedom per cell. It leads to the existence of the three dispersion curves. One of them can be immediately obtained from (1.33)

$$\omega_0^2 = 1 \, , \quad A_v = A^- = 0. \tag{1.34}$$

This branch is dispersionless and EWs corresponding to this branch are characterized by non-active vertical junctions and in phase $A_h = \tilde{A}_h$ (symmetric) librations of the upper and lower horizontal junctions.

The two others solutions are

$$\begin{aligned} \omega_\pm^2 &= F \pm \sqrt{F^2 - G} \, , \\ F &= \frac{1}{2} + \frac{1}{\beta_L \eta} + \frac{1}{2}\sqrt{1-\gamma^2} + \frac{1}{\beta_L}(1-\cos q) \, , \\ G &= (1 + \frac{2}{\beta_L \eta})\sqrt{1-\gamma^2} + \frac{2}{\beta_L}(1-\cos q) \, . \end{aligned} \tag{1.35}$$

Both branches have a nonzero dispersion.

The branch ω_+ is characterized by $A^+ = 0$ for all wave vectors q, i.e. the upper and lower horizontal phases are antisymmetric $A_h = -\tilde{A}_h$. The frequency range of the branch is above the degenerate branch ω_0, i.e. $\omega_+(q) > \omega_0$ and it depends strongly on β_L. As the parameter β_L increases, the width of $\omega_+(q)$ decreases and the branch approaches the dispersionless one, ω_0. In the opposite case of small β_L, the frequencies $\omega_+(q)$ increase as $1/\sqrt{\beta_L}$. For zero wave

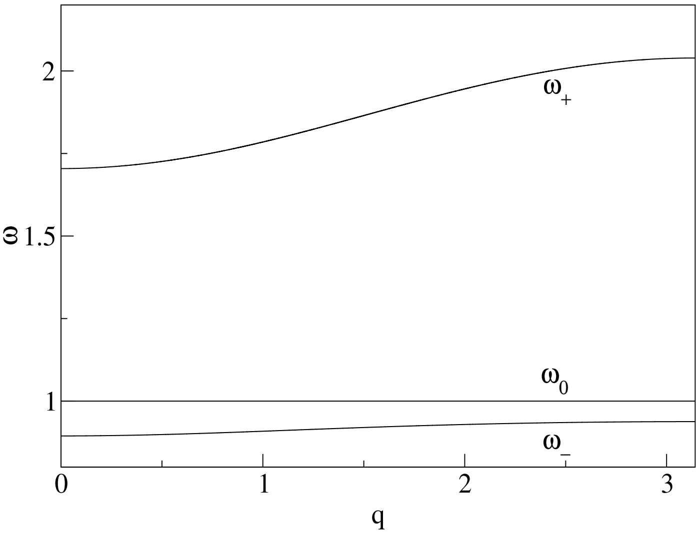

Figure 1.5: Typical spectrum of EW's for $\beta_L = 3.0$ and $\eta = 0.35$

number $q = 0$, the amplitudes of EWs in this branch are characterized by $A_v = 0$ and $A^+ = 0$, which means that only horizontal junctions are excited.

The branch ω_- becomes dispersionless for the particular case of $\gamma = 0$. The frequency range of this branch is located below ω_0, i.e. $\omega_-(q) < \omega_0(q)$. For zero wave number $q = 0$ the horizontal junctions are not active ($A^+ = A^- = 0$) and only vertical junctions are excited.

For a finite-size ladder the wave number q can take only a discrete set of values. The exact values are determined by the boundary conditions. As was mentioned above, the system under consideration possesses N cells and open boundary conditions. Therefore, it is possible to add fictive cells to the left $n = 0$ and to the right $n = N + 1$ edges and assume that the mesh currents in these cells are absent $I_0^m = I_{N+1}^m \equiv 0$. By using (1.20) and (1.24), this leads to

$$\begin{aligned} \phi_0^h &= \tilde{\phi}_0^h = 0 \,, \\ \phi_{N+1}^h &= \tilde{\phi}_{N+1}^h = 0. \end{aligned} \tag{1.36}$$

and substituting these relations into (1.22) we find

$$\begin{aligned} \phi_0^v - \phi_1^v &= 0 \,, \\ \phi_{N+1}^v - \phi_N^v &= 0. \end{aligned} \tag{1.37}$$

This result implies that a ladder consists of three subchains with different boundary conditions: horizontal subchains with *fixed* boundaries (1.36) and vertical one with *free* boundaries (1.37). Both boundaries give us the following wave numbers

$$q_l = \frac{l\pi}{N+1} \,, \tag{1.38}$$

where $l = 0, 1, \ldots N$ for vertical junctions and $l = 1, 2, \ldots N$ for horizontal ones.

1.3.3 Homogeneous whirling state

Josephson junction ladders and arrays possess another homogeneous state, when all vertical junctions are in a resistive state with the same voltage drops across them. In addition to this, in the case of a ladder geometry all horizontal junctions are at rest. Therefore the dynamics is similar in each vertical junction and the $I - V$ curve characteristics is similar to the $I - V$ curve for a single Josephson junction except for some regions which will be discussed later.

The HWS possesses a maximum voltage drop across the whole ladder. Due to its homogeneity it is possible to obtain the spectrum of small amplitude oscillations around it. It can be done in the same way as before. The spectrum also can be obtained from Eq. (1.35) by putting $\gamma = 1$.

2 Discrete breathers in Josephson junction ladders

Dynamical localized excitations persist in a JJL due to the intrinsic bistability property of a single small underdamped Josephson junction. A breather state in a JJL is characterized by few junctions being in the resistive state, while the rest of the junctions is in the superconducting state. The average voltage drop for any type of the breather due to its localization in space lies between zero and the one of the HWS, and exists only for the following range of dc bias $\gamma_r < \gamma < 1$. The Josephson phases of resistive junctions are unbounded in time and the Josephson phases of superconducting junctions display small amplitude librations with a frequency Ω. This frequency is called the *breather frequency.* The presence of breather states may be verified by measurements of a total dc voltage drop across the ladder and plotting the current-voltage $(I - V)$ characteristics. It has been successfully combined with snapshots made using low-temperature laser microscopy techniques, which allow for a spatial resolution of the dc voltage drop. Both methods provide only with time-averaged voltage drop data and the internal dynamics is so far not accessible in experiments.

Experimentally different types of breathers were observed. The aim of this chapter is to describe the main properties of breathers in JJLs and to study the resonant interaction between the breathers and electromagnetic excitations (EE's).

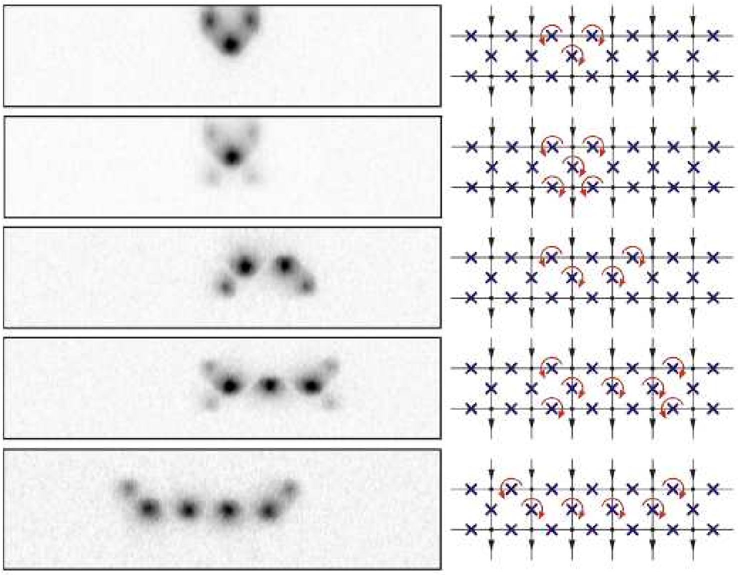

Figure 2.1: The experimental (left) and schematic (right) view of different types of DBs in JJLs. This picture is taken from from[12]

.

2.1 Symmetries of breathers

Different types of breathers in JJLs can be classified into three symmetry types using the reflection symmetries of the JJL. Some possible realizations are presented schematically in Fig. 2.2 Breathers from the first group reveal an **'up-down' reflection symmetry** $\hat{S}_{ud}$ (see, Fig. 2.2a), i.e. they are invariant under exchange of upper and lower horizontal junctions. The second group consists of breathers invariant under a **'left-right' reflection symmetry** $\hat{S}_{lr}$ (see, Fig. 2.2b), i.e. they are invariant under a reflection at a vertical line cutting the ladder (this line is located either in the middle between two vertical junctions, or passes directly through one vertical junction). A third distinct group of breathers possesses an **'inversion' symmetry** $\hat{S}_{in}$ (Fig. 2.2c), i.e. these breathers are invariant under a reflection at a point which is either located on a vertical junction or in the center of a plaquette. A fourth group of breathers has **no symmetries** at all and does not belong to any of the three listed symmetry types. A particular example of a breather without symmetry is shown in Fig. 2.2d. All of these types of breather excitations have been observed experimentally and numerically [115, 13, 12, 114]. Each group of breathers can also have a different number of vertical junctions in the resistive state. Note that the particular example in Fig. 2.2a possesses not only $\hat{S}_{ud}$ symmetry, but also $\hat{S}_{lr}$ and $\hat{S}_{in}$ symmetries. However it is also possible to construct more complex breather states which display $\hat{S}_{ud}$ symmetry only.

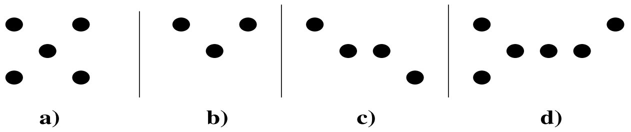

Figure 2.2: Examples of different types of breathers: a) up-down symmetry, b) left-right symmetry, c) inversion symmetry, d) no symmetry. Black spots indicate the positions of resistive junctions.

It is possible to derive the average voltage drop across a resistive vertical junction $V = \langle \dot{\phi}^v \rangle$ for different breather types. For the particular case of a breather with up-down symmetry $\hat{S}_{ud}$, there are k resistive vertical junctions in cells $(i+1)..(i+k)$ and two resistive horizontal junctions in the (i)th and $(i+k)$th cells respectively. Voltage drops across the vertical junctions in the resistive state are identical due to the flux quantization law (1.22). For the same reasons the voltage drops across the horizontal junctions are two times smaller. Neglecting nonlinear contributions from the time average of $\sin\phi$ on resistive junctions gives:

$$\begin{array}{l} \alpha\frac{V}{2} = \frac{1}{\eta}\langle I_i^m \rangle \\ \alpha V = \gamma + \langle I_{i+1}^m \rangle - \langle I_i^m \rangle \\ \ldots \\ \alpha V = \gamma + \langle I_{i+k}^m \rangle - \langle I_{i+k-1}^m \rangle \\ \alpha\frac{V}{2} = -\frac{1}{\eta}\langle I_{i+k}^m \rangle \ . \end{array} \tag{2.1}$$

Thus, the voltage drop across a resistive vertical junction that corresponds to the experimentally measured voltage drop across the ladder, is given by

$$V = \frac{k\gamma}{\alpha(k+\eta)} \ . \tag{2.2}$$

A breather with left-right symmetry $\hat{S}_{lr}$ and with inversion symmetry $\hat{S}_{in}$ can be analyzed in a similar way, but taking into account that in these cases the voltage drops across resistive horizontal and vertical junctions are identical

$$V = \frac{k\gamma}{\alpha(k+2\eta)} \ . \tag{2.3}$$

In a similar manner the result for a breather which has no symmetry (cf. Fig. 2.2d) reads

$$V = \frac{k\gamma}{\alpha(k+\frac{3}{2}\eta)} \; . \tag{2.4}$$

The above results for the dependence of the average voltage drop on the dc bias may be combined in a single expression

$$V = \frac{k\gamma}{\alpha[k+(3-\frac{1}{2}\delta)\eta]} \; , \tag{2.5}$$

where k is the number of vertical resistive junctions and δ denotes the number of resistive horizontal junctions. Note that $\delta = 4$ for breathers with up-down symmetry, $\delta = 2$ for left-right or inversion symmetry, and $\delta = 3$ for no symmetry.

The breather frequency is given by the lowest realized voltage drop across a resistive junction
1) up-down symmetry

$$\Omega = \frac{k\gamma}{2\alpha(k+\eta)} \; , \tag{2.6}$$

2) left-right symmetry and inversion symmetry

$$\Omega = \frac{k\gamma}{\alpha(k+2\eta)} \; , \tag{2.7}$$

3) no symmetry

$$\Omega = \frac{k\gamma}{\alpha(2k+3\eta)} \; . \tag{2.8}$$

2.2 Spatial tails of breathers

Far from the breather center Josephson phases librate with small amplitudes. These amplitudes decay exponentially and can be represented in the following form

$$\begin{pmatrix} \varphi_n^v \\ \varphi_n^h \\ \tilde{\varphi}_n^h \end{pmatrix} = e^{\lambda n + i\Omega t} \begin{pmatrix} A_v \\ A_h \\ \tilde{A}_h \end{pmatrix} \; . \tag{2.9}$$

As before, it is more convenient to introduce new variables

$$A_h^- = \frac{1}{2}(A_h - \tilde{A}_h) \;\; , \;\; A_h^+ = \frac{1}{2}(A_h + \tilde{A}_h) \; . \tag{2.10}$$

Substituting (2.9) and (2.10) into Eq. (1.29) gives the following set of equations

$$\begin{aligned} (C - \frac{2}{\beta_L}\cosh\lambda)A_v - \frac{2}{\beta_L}(1-e^{-\lambda})A_h^- &= 0 \; , \\ -\frac{1}{\beta_L\eta}(1-e^{\lambda})A_v + DA_h^- &= 0 \; , \\ (-\Omega^2 + i\alpha\Omega + 1)A_h^+ &= 0 \; , \end{aligned} \tag{2.11}$$

where the frequency dependent parameters C and D are

$$\begin{aligned} C &= -\Omega^2 + i\alpha\Omega + \sqrt{1-\gamma^2} + \frac{2}{\beta_L} \\ D &= -\Omega^2 + i\alpha\Omega + 1 + \frac{2}{\beta_L\eta} \; . \end{aligned} \tag{2.12}$$

From (2.11) it follows that $A_h^+ = 0$ and hence $A_h = -\tilde{A}_h$. Therefore $\varphi_n^h = -\tilde{\varphi}_n^h$, i.e. breather

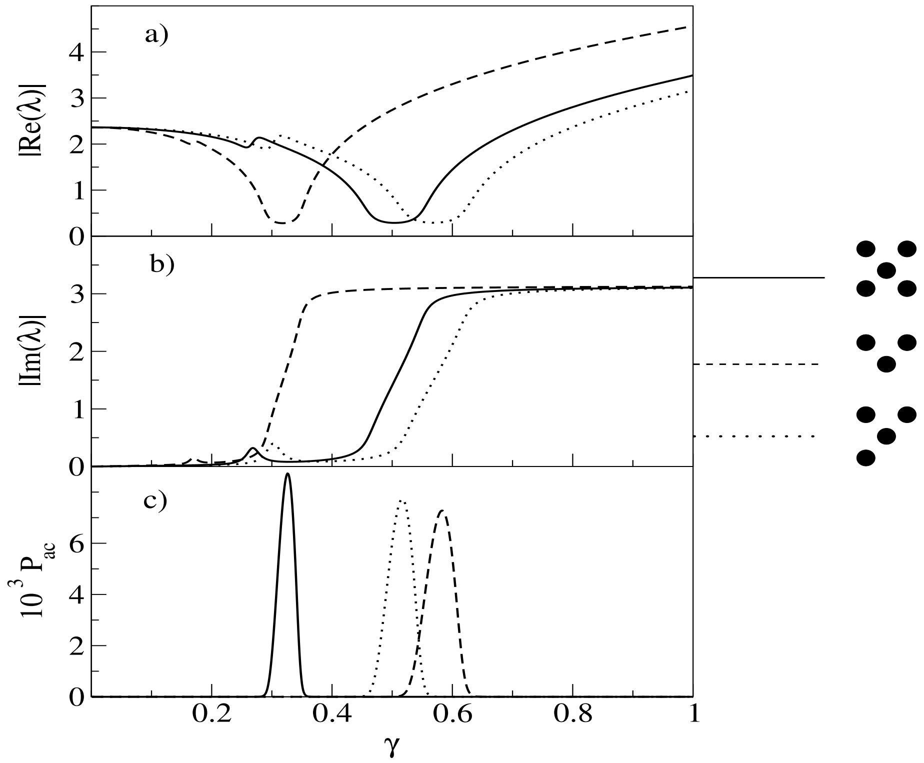

Figure 2.3: Dependence of (a) real part $Re(\lambda)$, (b) imaginary part $Im(\lambda)$, and (c) P_{ac} on γ for different types of breathers: solid line - up-down symmetry, dashed line - left-right symmetry, dotted line - no symmetry. The parameters are $\alpha = 0.1$, $\beta_L = 3.0$, $\eta = 0.35$ and $k = 1$.

tails appear with perfect up-down symmetry. This is at variance with the complex symmetry properties of the resistive breather center.

A nontrivial solution to the first two equations in (2.11) exists if

$$CD - \frac{2}{\beta_L} D \cosh\lambda - \frac{4}{\beta_L^2 \eta} + \frac{4}{\beta_L^2 \eta} \cosh\lambda = 0\ . \tag{2.13}$$

The dependence of the complex parameter λ on the breather frequency Ω is given by

$$\lambda = \ln(z + \sqrt{z^2 - 1})\quad , \tag{2.14}$$

with

$$z\ =\ \frac{4 - \beta_L^2 \eta CD}{4 - 2\beta_L \eta D}\ . \tag{2.15}$$

Note here that this expression can be obtained directly from Eqs. (1.35) by assuming that $q = i\lambda$ and substituting $\Omega^2 - i\alpha\Omega$ instead of $\omega_\pm^2$.

The real $Re(\lambda)$ part determines the spatial decay and imaginary $Im(\lambda)$ part - the spatial period of oscillations of Josephson phases in the breather tail. $Re(\lambda)$ and $Im(\lambda)$ strongly depend on the breather frequency that in turn, can be changed by varying the external dc bias γ. In Fig. 2.3(a,b) the real and imaginary parts of λ for three breather types (cf. Fig. 2.2) versus γ are plotted. The minima of the real part of λ correspond to resonances with linear EWs $\omega_+(q)$

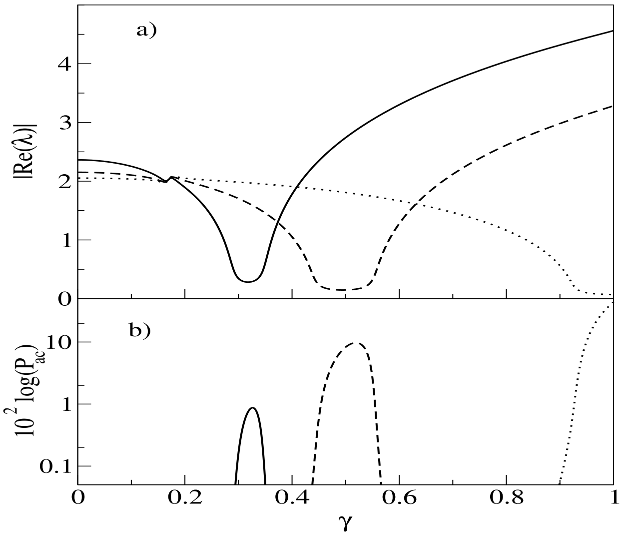

Figure 2.4: (a) $\Re(\lambda)$ and (b) P_{ac} versus γ for different values of the inductance of the cell: $\beta_L = 3$, solid line; $\beta_L = 1$, dashed line; $\beta_L = 0.2$, dotted line. All of these curves are for a left-right symmetry breather with $k = 1$.

and $\omega_-(q)$. Since the EW frequencies $\omega_+(q)$ decrease with increasing inductance of the cell , the position of the global minimum also depends strongly on β_L (see Fig.2.4(a)).

These resonances do not destroy the breather itself due to the presence of the damping term α, only the amplitudes of the Josephson phases in the tail become larger. The strength of the resonances can be measured by means of the time-average power P_{ac} of the libration of a junction at the edge of a JJL. The value of P_{ac} is determined by the average kinetic energy of the edge vertical junction (see also Appendix E)

$$P_{ac} = \frac{1}{2}\langle \dot{\phi}_l^{v^2} \rangle \quad l = -\frac{N}{2} \tag{2.16}$$

The typical dependencies of P_{ac} on the dc bias and the inductance of the cell for different types of breathers are presented in Figs. 2.3c, 2.4b.

2.3 Linear stability of breathers

The stability of periodic motion is analyzed with the help of the Floquet theory [2, 118]. Here we will show that the system under consideration can be reduced to an effective Hamiltonian one [87].

First of all, the phase-space flow around a given breather solution ϕ_n^b should be linearized. Linearization of system (1.26) is made by means of a small fluctuation ϵ_n around the breather $\phi_n = \phi_n^b + \epsilon_n$

$$\begin{aligned}
\ddot{\epsilon}_n^v + \alpha\dot{\epsilon}_n^v + X_n^v(t)\epsilon_n^v &= \frac{1}{\beta_L}(\triangle\epsilon_n^v + \nabla\epsilon_{n-1}^h - \nabla\tilde{\epsilon}_{n-1}^h) \\
\ddot{\epsilon}_n^h + \alpha\dot{\epsilon}_n^h + X_n^h(t)\epsilon_n^h &= -\frac{1}{\eta\beta_L}(\nabla\epsilon_n^v + \epsilon_n^h - \tilde{\epsilon}_n^h) \\
\ddot{\tilde{\epsilon}}_n^h + \alpha\dot{\tilde{\epsilon}}_n^h + \tilde{X}_n^h(t)\tilde{\epsilon}_n^h &= \frac{1}{\eta\beta_L}(\nabla\epsilon_n^v + \delta_n^h - \tilde{\epsilon}_n^h) ,
\end{aligned} \tag{2.17}$$

where $X_n(t) = \cos(\phi_n^b(t))$ are time-periodic coefficients determined by the given breather state.

The substitution

$$\begin{pmatrix} \epsilon_n^v \\ \epsilon_n^h \\ \tilde{\epsilon}_n^h \end{pmatrix} = e^{-\frac{1}{2}\alpha t} \begin{pmatrix} \kappa_n^v \\ \kappa_n^h \\ \tilde{\kappa}_n^h \end{pmatrix} \tag{2.18}$$

allows one to eliminate the dissipation

$$\begin{aligned} \ddot{\kappa}_n^v + B_n^v(t)\kappa_n^v &= \frac{1}{\beta_L}(\triangle\kappa_n^v + \nabla\kappa_{n-1}^h - \nabla\tilde{\kappa}_{n-1}^h) \\ \ddot{\kappa}_n^h + B_n^h(t)\kappa_n^h &= -\frac{1}{\eta\beta_L}(\nabla\kappa_n^v + \kappa_n^h - \tilde{\kappa}_n^h) \\ \ddot{\tilde{\kappa}}_n^h + \tilde{B}_n^h(t)\tilde{\kappa}_n^h &= \frac{1}{\eta\beta_L}(\nabla\kappa_n^v + \kappa_n^h - \tilde{\kappa}_n^h)\ , \end{aligned} \tag{2.19}$$

where $B_n(t) = \frac{1}{4}\alpha^2 + X_n(t)$. Introduction of new variables

$$z_n^v = \kappa_n^v \ , \ \ z_n^h = \sqrt{\eta}\kappa_n^h \ , \ \ \tilde{z}_n^h = \sqrt{\eta}\tilde{\kappa}_n^h \ , \tag{2.20}$$

produces the following system of equations

$$\begin{aligned} \ddot{z}_n^v + B_n^v(t)z_n^v &= \frac{1}{\beta_L}\triangle z_n^v + \frac{1}{\beta_L\sqrt{\eta}}(\nabla z_{n-1}^h - \nabla\tilde{z}_{n-1}^h) \\ \ddot{z}_n^h + B_n^h(t)z_n^h &= -\frac{1}{\eta\beta_L}(z_n^h - \tilde{z}_n^h) - \frac{1}{\beta_L\sqrt{\eta}}\nabla z_n^v \\ \ddot{\tilde{z}}_n^h + \tilde{B}_n^h(t)\tilde{z}_n^h &= \frac{1}{\eta\beta_L}(z_n^h - \tilde{z}_n^h) + \frac{1}{\beta_L\sqrt{\eta}}\nabla z_n^v\ . \end{aligned} \tag{2.21}$$

These equations describe a *Hamiltonian* system, namely

$$\dot{\vec{z}}_n = \frac{\partial\mathcal{H}}{\partial\vec{p}_n}\ , \quad \dot{\vec{p}}_n = -\frac{\partial\mathcal{H}}{\partial\vec{z}_n}\ , \tag{2.22}$$

where $\vec{z}_n = (z_n^v, z_n^h, \tilde{z}_n^h)$, $\vec{p}_n = (p_n^v, p_n^h, \tilde{p}_n^h)$ and the Hamiltonian $\mathcal{H}(\vec{z}_n, \vec{p}_n, t)$ is

$$\begin{aligned} \mathcal{H} \;=\; & \frac{1}{2}\sum_n [p_n^{v^2} + p_n^{h^2} + \tilde{p}_n^{h^2}] + \frac{1}{2}\sum_n [B_n^v z_n^{v^2} + B_n^h z_n^{h^2} + \tilde{B}_n^h \tilde{z}_n^{h^2}] \\ & + \frac{1}{2\beta_L}\sum_n (z_n^v - z_{n-1}^v)^2 + \frac{1}{2\beta_L\eta}\sum_n (z_n^h - \tilde{z}_n^h)^2 + \frac{1}{\beta\sqrt{\eta}}\sum_n z_n^v[z_{n-1}^h - \tilde{z}_{n-1}^h - z_n^h + \tilde{z}_n^h]\ . \end{aligned} \tag{2.23}$$

Since the particular Hamiltonian can be represented in a general quadratic form, the symplectic product of two different trajectories $\{\vec{p}_n(t), \vec{z}_n(t)\}$ and $\{\vec{p}_n^{\,\prime}(t), \vec{z}_n^{\,\prime}(t)\}$ does not change in time [2]

$$\mathcal{I} = \sum_n [\vec{p}_n^{\,\prime}(t)\vec{z}_n(t) - \vec{p}_n(t)\vec{z}_n^{\,\prime}(t)]\ . \tag{2.24}$$

Rewriting the set of equations (2.21) in the form

$$\begin{aligned} \delta\dot{\vec{z}}_n &= \frac{\partial^2\mathcal{H}}{\partial\vec{p}_n^{\,2}}\delta\vec{p}_n + \frac{\partial^2\mathcal{H}}{\partial\vec{p}_n\partial\vec{z}_n}\delta\vec{z}_n \\ -\delta\dot{\vec{p}}_n &= \frac{\partial^2\mathcal{H}}{\partial\vec{z}_n\partial\vec{p}_n}\delta\vec{p}_n + \frac{\partial^2\mathcal{H}}{\partial\vec{z}_n^{\,2}}\delta\vec{z}_n\ , \end{aligned} \tag{2.25}$$

and using the notation

$$\mathcal{J} = \begin{pmatrix} 0 & E \\ -E & 0 \end{pmatrix}\ , \tag{2.26}$$

where E is the identity matrix, leads to

$$\left(\begin{array}{c} \delta\dot{\vec{p}}_n \\ \delta\dot{\vec{z}}_n \end{array} \right) = \mathcal{J}^{-1}\nabla^2\mathcal{H} \left(\begin{array}{c} \delta\vec{p}_n \\ \delta\vec{z}_n \end{array} \right) , \tag{2.27}$$

where $\nabla^2\mathcal{H}$ is the *Hessian* of $\mathcal{H}$.

Following the Floquet theory, the map, which is obtained by integrating the equations (2.27) over one period T_b of the initial solution, should be analyzed

$$\left(\begin{array}{c} \delta\vec{p}_n(T_b) \\ \delta\vec{z}_n(T_b) \end{array} \right) = \mathbf{F}(T_b) \left(\begin{array}{c} \delta\vec{p}_n(0) \\ \delta\vec{z}_n(0) \end{array} \right) . \tag{2.28}$$

Since the form $\mathcal{J}$ is symplectic (2.24) , $\mathbf{F}(T_b)$ is symplectic too. As a result, the eigenvalues of $\mathbf{F}(T_b)$ have to fulfill the condition that if ν is an eigenvalue then $\frac{1}{\nu}$, ν^* and $\frac{1}{\nu^*}$ are also eigenvalues. These relations may be rewritten for the original $\epsilon_n(t)$ variables with corresponding Floquet eigenvalues μ. First of all, most eigenvalues will be located on a circle of radius

$$R(\alpha) = e^{\frac{-\alpha\pi}{\Omega}} , \tag{2.29}$$

in the complex plane, which is less than 1. Further, it follows that if μ is an eigenvalue then $\frac{e^{-\alpha T_b}}{\mu}$, μ^* and $\frac{e^{-\alpha T_b}}{\mu^*}$ are eigenvalues too and may be expressed in the general form

$$\mu = R(\alpha)\exp\left(\pm i\omega\frac{2\pi}{\Omega}\right) , \tag{2.30}$$

where Ω is the breather frequency and ω is some characteristic frequency. Stable breathers are characterized by all Floquet multipliers being located inside or on the unit circle (see Fig. 1.3 in Part I). Note that due to the periodicity of the breather state there is always one eigenvalue $\mu = 1$, whose eigenvector is tangent to the breather orbit. There is always, consequently, another eigenvalue $\mu = e^{-\alpha T_b}$ which is located on the positive real axis inside the unit circle.

The corresponding eigenvectors may be divided into two classes, namely those which are localized on a breather and those which are delocalized. Delocalized Floquet eigenstates simply correspond to the linear EWs with frequencies ω from the spectrum (1.35). The concrete form of localized eigenvectors and its frequencies ω_L has to be obtained numerically. The localized states are similar to the bound states of a potential well with the frequencies out of the spectrum (1.35).

2.4 Types of resonances

Stable breathers are characterized by all Floquet multipliers being located inside or on the unit circle. Instabilities occur after collisions of multipliers on the inner circle with radius (1.37) and a subsequent shift from this circle towards larger absolute values. In the dissipative case a finite change of the control parameter (dc bias γ) away from the collision is necessary in order for the corresponding Floquet eigenvalue(s) to cross and leave the unit circle.

It should be noted, that for Hamiltonian systems any collision and shift from the unit circle leads to an instability. A finite, even possibly weak dissipation may drastically change the instability patterns by selecting the strong instabilities (large detachments) over the weak instabilities (small detachments).

The collision means that two (or more) eigenvalues μ_1 and μ_2 coincide on the circle of radius (1.37). The equivalence $\mu_1 = \mu_2$ leads to the relation between phases

$$\omega_1\frac{2\pi}{\Omega} = \omega_2\frac{2\pi}{\Omega} + 2\pi m , \tag{2.31}$$

where m is integer number.

The first case is realized when the collision takes place on the positive real axis in the complex plane at +1. This implies that a multiplier is colliding with its complex conjugate partner. In (2.31) it means that $\omega_2 = 0$ and therefore

$$\omega = m\Omega , \tag{2.32}$$

for any integer number m. These are **primary resonances** of the breather frequency or its higher harmonics with any of the frequencies of the EEs.

The collision of an eigenvalue with its complex conjugated partner can also take place on the negative real axis in the complex plane at -1. This condition is realized when, formally $\omega_2 \frac{2\pi}{\Omega} = \pi$ or $\omega_2 = \frac{\Omega}{2}$

$$\omega = (\frac{1}{2} + m)\Omega \; . \tag{2.33}$$

These are **parametric resonances** of a breather state with EEs .

The third case is realized when the collision takes place away from the real axis. Then a multiplier has to collide with a different one, but not with its own complex conjugate partner. It follows that

$$\omega_1 \pm \omega_2 = m\Omega \; . \tag{2.34}$$

This is a **combination resonance**, as the breather frequency (or its multiple) has to match a sum (difference) of the frequencies of two different EE frequencies.

The collisions between delocalized Floquet multipliers can be studied analytically. But this is not a case for the localized ones, for which numerical calculations should be used. Especially the combination resonance may involve either two delocalized, two localized or one delocalized and one localized Floquet eigenvalues. In addition the above mentioned dissipation-induced selection of weak and strong instabilities will result in some possible collisions being harmless (leaving the breather stable) while others will turn out to be important for understanding breather instabilities.

2.5 Current-Voltage characteristics of breathers

The breather dynamics is studied by varying a control parameter (dc bias) in the direct numerical simulations of the set of equations (1.26). It gives the possibility to study the outcome of instabilities of breathers. Moreover, this scheme is close to the experimental setup and allows us to compare the results. The Newton scheme together with Floquet analysis are used in order to study the types of instabilities.

All simulations were carried out for JJLs with $N = 10$ cells and open boundary conditions by the means of the 4th order Runge-Kutta method. Time is measured in dimensionless time units. The initial value of the dc bias was $\gamma = 0.8$. The initial conditions can be obtained with the help of the derived expressions (2.5) that lead to the relaxation of the system into a particular breather state of left-right symmetry with one resistive vertical junction, as in Fig. 2.2b. After a waiting time of 500 time units, the next 500 time units are used to calculate the time averaged characteristics of the state. Then the dc bias γ is decreased by a tiny step of $\Delta\gamma = 0.0005$ and the whole procedure is repeated again. It was checked that the results do not change upon further increase of the waiting time. The tunable parameters for different simulations are the anisotropy η and the inductance of the cell β_L, while the dissipation $\alpha = 0.1$ was fixed.

There are three different ways to monitor the simulations. The first one is the $I - V$ characteristics, that is the dependence of the averaged voltage drop across the resistive vertical junction on the dc bias. Furthermore the power P_{ac} (2.16) of ac oscillations of the vertical junction at the edge of JJLs is used. Finally the time-resolved images (movies) of the full dynamical behavior of the ladder are considered to check visually whether the system still resides in the initially chosen breather state, or switches into another state.

Each figure consists of two parts. In the left hand parts the $I - V$ characteristics are shown (solid lines) together with the approximate results from subsection (2.3.1) (dotted lines). The vertically oriented dashed lines indicate the band edges of the linear EWs. In the right hand part of the figures the dependence of P_{ac} (solid lines) on the dc bias is shown together with the approximate analysis from subsection (6.1) (dashed lines) where appropriate.

The first example is the case of small β_L values. For $\beta_L = 0.2$ and $\eta = 1.15$ (Fig. 2.5) the breather is easily excited, and its frequency is located below $\omega_+(q)$. In the P_{ac} plot there

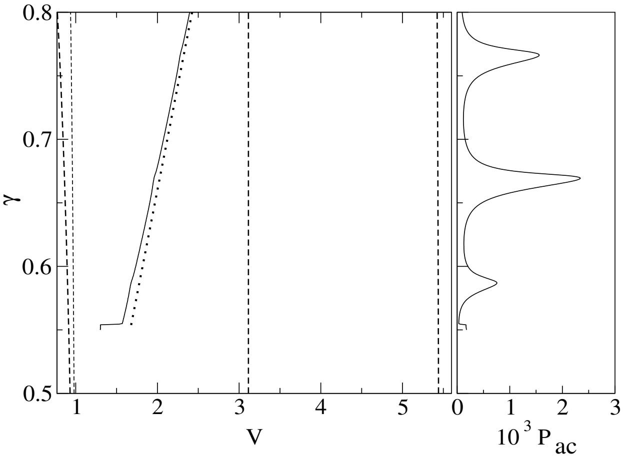

Figure 2.5: $I - V$ characteristics and the P_{ac} dependence on the dc bias current for $\alpha = 0.1$, $\beta_L = 0.2$, $\eta = 1.15$.

are peaks that are due to the resonance of the second and third harmonics of the breather with $\omega_+(q)$. These resonances are primary ones as discussed above. The series of observed peaks is related to the finite size of the system, and therefore to the resonant interaction of the breather with a discrete set of cavity modes (1.38). In order to test this assumption, the size of the system was increased and the predicted increase in the number of resonance peaks was observed. Close to the lowest possible current (around $\gamma = 0.55$) there is a switching to another breather state, which however has the same symmetry and spatial structure. Note that shortly after this switching (upon further lowering of the current) the breather is destroyed and the system switches to the superconducting ground state.

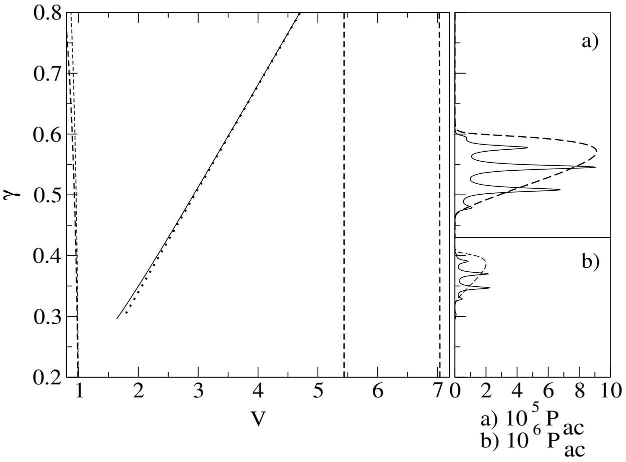

Figure 2.6: $I - V$ characteristics and the P_{ac} dependence on the dc bias current for $\alpha = 0.1$, $\beta_L = 0.2$, $\eta = 0.35$.

For lower values of the anisotropy $\eta = 0.35$ (Fig. 2.6) the resonances are again not detectable in the $I - V$ curve. However, the singularities in P_{ac} correspond to the primary resonance $2\Omega = \omega_+(q)$. Moreover, at the dc bias $\gamma \approx 0.35$ a weak third-order primary resonance $3\Omega = \omega_+(q)$ is detected in the breather tail. The dashed line in the right part of the figure is the prediction of P_{ac} using the approximate tail analysis. The approximate tail analysis is based on the assumption of a dense spectrum of EWs. Consequently the calculated P_{ac} presents an envelope of the numerically observed series of discrete peaks.

For the next simulation the inductance of the cell was increased to $\beta_L = 0.5$. Fig. 2.7 represents the results for $\eta = 1.15$. For the initial value of the dc bias $\gamma = 0.8$ the breather frequency is already located inside the $\omega_+(q)$ band of EWs, and this primary resonance is observed in the $I - V$ curve. Indeed, the slope of the $I - V$ curve is larger than the prediction (2.5) which does not take into account resonant interactions with EEs. With decreasing dc bias, the breather frequency is lowered and the above primary resonance disappears. However at lower current values the next primary resonances $2\Omega = \omega_+(q)$ occur and are observable, both in the breather tail and in the $I - V$ characteristics.

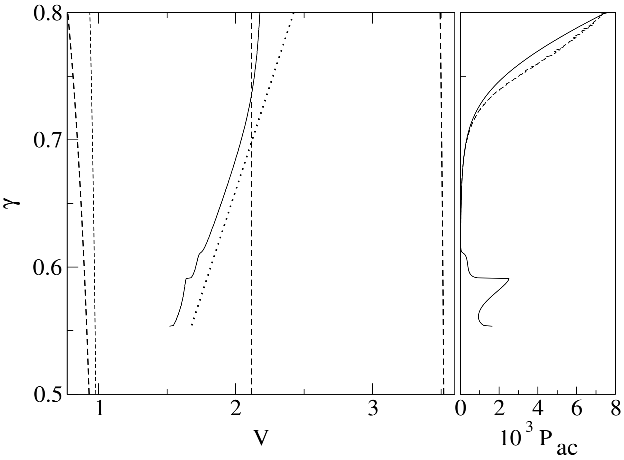

Figure 2.7: $I - V$ characteristics and the P_{ac} dependence on the dc bias current for $\alpha = 0.1$, $\beta_L = 0.5$, $\eta = 1.15$.

The primary resonance structures ($\Omega = \omega_+(q)$) in the large current domain are also observed for smaller values of the anisotropy parameter $\eta = 0.5$ (see Fig. 2.8). In this case, they manifest themselves through *resonant steps* in the $I - V$ curve. At lower values of the dc bias the primary resonances with $m = 2$ are observed.

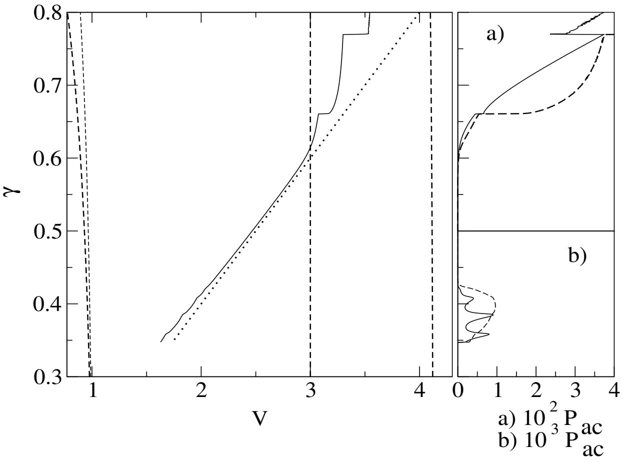

Figure 2.8: $I - V$ characteristics and the P_{ac} dependence on the dc bias current for $\alpha = 0.1$, $\beta_L = 0.5$, $\eta = 0.5$.

For $\beta_L = 1.0$ and $\eta = 0.5$ (Fig. 2.9) the breather frequency is located above $\omega_+(q)$ for large current values. Upon decreasing the dc bias there is a peculiar switching to a different breather state with the same spatial structure but a lower frequency located inside $\omega_+(q)$. The most interesting feature here is that shortly before the switching the breather frequency is clearly larger and outside of the $\omega_+(q)$ region. Upon further lowering of the dc bias primary resonances $\Omega = \omega_+(q)$ occur and corresponding resonant steps in $I - V$ curve.

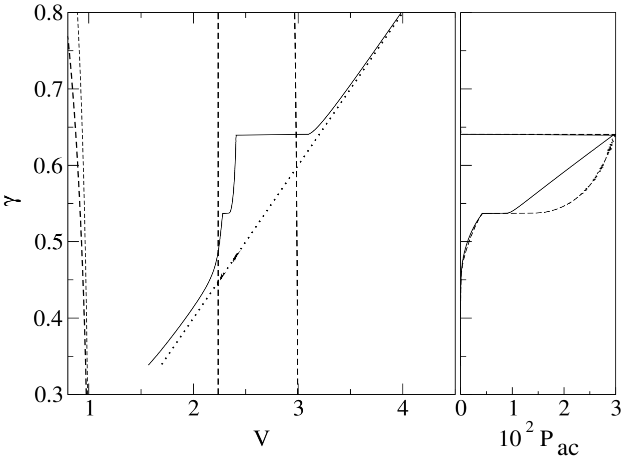

Figure 2.9: $I - V$ characteristics and the P_{ac} dependence on the dc bias current for $\alpha = 0.1$, $\beta_L = 1.0$, $\eta = 0.5$.

For $\beta_L = 3$ and $\eta = 0.5$ (Fig. 2.10) the breather frequencies are located again above ω_+ for large current values. Similar to the previous case there is a switching when the breather frequency is clearly outside (above) the branch $\omega_+(q)$. This brings the system into another breather state with the same spatial structure, but with a frequency again located above ω_+. This highly nonlinear state is then lost by switching to the superconducting ground state after further decrease of the dc bias.

An interesting observation is found for lower values of the anisotropy $\eta = 0.35$ (Fig. 2.11). For this case there is the switching at a breather frequency being located above $\omega_+(q)$. However the switching *increases* the voltage drop. The new state is of different internal structure, while all previous numerical results have been obtained for a breather with a structure as in Fig. 2.2b. After the switch the new breather state is characterized by *three* vertical junctions being in the resistive state. At the same time the symmetry is broken. In fact the new state exactly corresponds to the example given in Fig. 2.2d. Note that similar switchings (which lead to an increase of the number of resistive junctions) have been reported in early experimental studies [13]. Note here, that similar switchings with the increase of number of resistive junctions have been obtained in numerics in Ref. [52] for a rather different set of dynamic equations. Such switchings have not been found in extensive numerical simulations, in Ref. [114]. The reason for that is a rather large step of the dc bias decrease using in their simulations. The left-right symmetry breaking leads to new interesting features in the breather tails. The nonsymmetric breather has two times lower frequency than the voltage drop across the vertical junction. Thus the new breather frequency is inside the upper band $\omega_+(q)$, and a primary resonance is clearly observed in the P_{ac} dependence on γ.

At last the breather dynamics in the JJL with an extremely large inductance of the cell $\beta_L = 500$ was numerically simulated . There is no indication of resonances and instabilities. The reason for that is the weak dispersion of the linear EWs for such large values of β_L. This implies that interactions along the ladder are weak. The breather is continued to small current values until it switches to the superconducting state at the dc bias $\gamma = 0.22$ for $\eta = 0.35$. This particular value can be obtained similar to the standard theory of the retrapping current in a single small Josephson junction [114, 9]

$$\gamma_r = (1+2\eta)\frac{4\alpha}{\pi} \; . \tag{2.35}$$

This equation yields a value of 0.22 for the considered case, in good agreement with the numerical observation. Note that within this theory retrapping occurs purely due to energy considerations, not due to resonances (or instabilities).

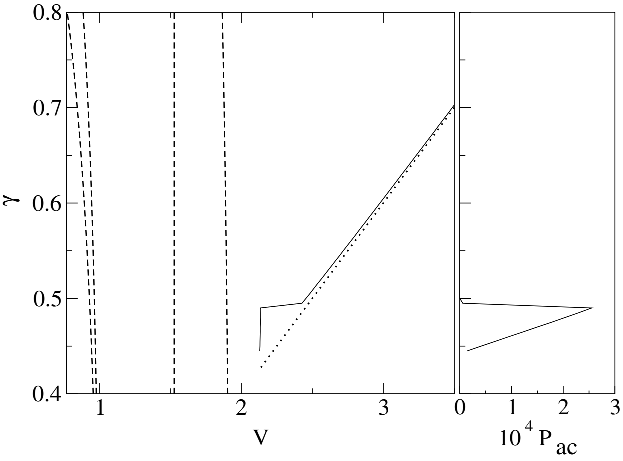

Figure 2.10: $I-V$ characteristics and the P_{ac} dependence on the dc bias current for $\alpha = 0.1$, $\beta_L = 3.0$, $\eta = 0.5$.

It is very important to notice that for cases with small or intermediate values of inductance of the cell (Fig. 2.5-2.11) the observed currents at which the breather state switches to the superconducting one exceed the expected retrapping values (1.19). This will be explained in the next section.

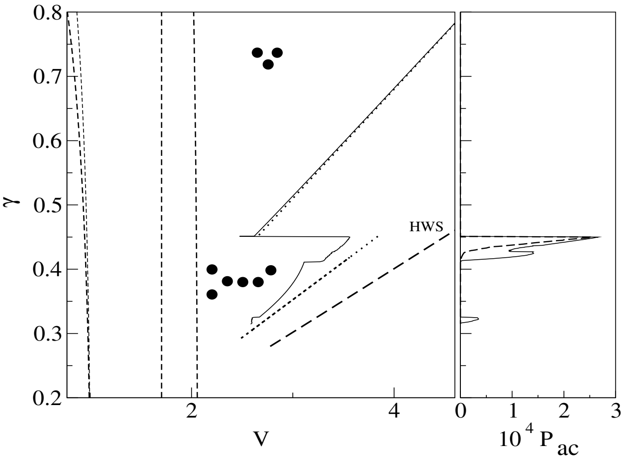

Figure 2.11: $I-V$ characteristics and the P_{ac} dependence on the dc bias current for $\alpha = 0.1$, $\beta_L = 3.0$, $\eta = 0.35$.

3 Evaluation of resonances

As was shown in the previous chapter there are three types of resonances, which are characterized by some relations between the frequency of a breather Ω and the spectrum of EEs. From numerical simulations in Fig.(2.5-2.11) it follows that not all resonances lead to the instability of a breather state due to the presence of the dissipation, while some others do. The aim of this chapter is to give a quantitative explanation of the observed resonances and switchings.

3.1 Primary resonances

Primary resonances are characterized by the condition $m\Omega = \omega$, where ω is some EE frequency.Various primary resonances were detected with *extended* EWs. The case $m = 1$, which corresponds to the breather frequency being located inside the $\omega_+(q)$ band, shows up with resonant steps in the $I - V$ curves (see, Figs. 2.5-2.11). The finite number of observed resonant steps is due to the discrete spectrum of the excited cavity modes. In addition we observe strong variations of the breather tail amplitudes.

Higher order primary resonances ($m = 2, 3$) are much less pronounced in the $I - V$ characteristics. They mainly lead to a weaker localization of the breather tail and can be clearly detected in the form of sharp peaks in the $P_{ac}(\gamma)$ dependence. Since the breather in our case has left-right symmetry, the only linear cavity modes which can be exited are symmetric (see section II). These modes are characterized by even values of k in the expression q_k(1.38).

The first case of the manifestation of a primary resonance is represented in Fig. 2.6. The value of the dc bias γ of each observed peak in $P_{ac}(\gamma)$ corresponds to the breather frequency $\Omega(\gamma)$. Then its multiples are compared with the discrete spectrum of linear mode frequencies of the ω_+ branch. The numbers are listed in Table 3.1. All observed resonances are due to symmetric linear modes (even $k = 2, 4, 6, 8, 10$) as expected.

The same method of analysis allows to conclude that the three peaks in Fig.2.6(b) (in decreasing order of dc bias) are due to the following resonances: $(m, k) = (2, 6); (2, 4); (3, 8)$. Similarly the shoulder and the peak in Fig. 2.7 are due to resonances with $(m, k) = (2, 10); (2, 8)$. Finally the resonances in Fig. 2.8 correspond to the values $(m, k) = (2, 8); (2, 6); (2, 4)$. Note

k	$\omega_+(q_k)$	2Ω	3Ω
1	5.475		
2	5.581	5.594	5.590
3	5.745		
4	5.949	5.947	5.945
5	6.174		
6	6.400	6.387	6.384
7	6.609		
8	6.788	6.769	6.772
9	6.923		
10	7.008	6.960	6.958

Table 3.1: Comparison of theoretical predictions of primary resonances with the numerical results from Fig. 2.6. First column: k. Second column: the spectrum of EWs $\omega_+(q_k)$ (cf. (1.38). Third column: 2Ω obtained from the peak positions of $P_{ac}(\gamma)$ in Fig. 2.6(a). Fourth column: 3Ω obtained from the peak positions of $P_{ac}(\gamma)$ in Fig. 2.6(b).

that in all of these cases the deviations between the theoretical and observed numbers are much less than the frequency difference between adjacent cavity modes.

Steps in the $I - V$ curve correspond to the case $m = 1$, when the breather switches to the *resonant* state, preserving its spatial structure and time periodicity. If instead of decreasing the dc bias γ it will be increasing, these steps will produce hysteresis loops due to the coexistence of different states of the same breather for a given value of the current γ (normal and resonant).

3.2 Parametric resonances

The switching from a breather state to the superconducting state for small and intermediate values of β_L will be discussed here. There are three possibilities which can lead to such a switching of a DB. The first one is due to an instability of a breathers. The second one is due to the disappearing of a breather as a solution. And the last one is due to the large sadden changing of a control parameter, which lead to a sadden changing of the phase space and a given trajectory may now belongs to the basin of attraction of another breather. The Floquet analysis results show that *all* above switchings are due to an *instability* of the breather. In terms of Floquet multipliers, all of these instabilities are due to a collision of two *localized* Floquet multipliers on the negative real axis. The breather state continues to exist as a solution to the dynamical equations for lower current values, but it is unstable. Note that the so-called retrapping mechanism instead (as for a single junction) uses the critical *current* value as a criterion for retrapping. This argument is based purely on energy considerations and does not take into account any resonance mechanism. This is not surprising, as a single junction has no other degrees of freedom it may resonate with. Below the retrapping current, the resistive state disappears in this case. So the switching from a breather state to the superconducting one as observed in the simulations is usually driven by *resonances* with localized EEs (frequency matching) and is *not* due to energy effects (current value matching).

3.3 Combination resonances

Here the nature of the switchings of the breather for intermediate β_L values when the breather frequency is located *above* the branch $\omega_+(q)$ will be discussed. These switchings are again due to an instability. It is characterized by Floquet multipliers colliding away from the real axis. As was discussed above this corresponds to a combination resonance. The numerical Floquet analysis shows that one of the two participating multipliers is a *localized* one (which bifurcates from the lower branch $\omega_-(q)$)., while the second one belongs to the delocalized spectrum of $\omega_+(q)$. The Floquet multiplier which finally leaves the unit circle is a *localized* one. So again the instability of the breather is driven by a localized perturbation. In Fig. 3.1 the dependence of the arguments and absolute values of all relevant Floquet multipliers is shown for the breather of Fig. 2.11. For convenience the complex conjugate multipliers are not plotted and the arguments are restricted to $0 \leq arg(\mu) \leq \pi$. The narrow band $\omega_-(q)$ and broad band $\omega_+(q)$ are nicely observed. The degenerate band ω_0 is located slightly above $\omega_-(q)$. This band does not interact with other multipliers when crossing them, as expected from our analytical considerations. The two separated arguments which are located *below* the $\omega_-(q)$ band have *localized* eigenvectors.

In the plot of the absolute values we observe the predicted values $\mu = 1$ and $e^{-\alpha T_b}$. The multipliers which correspond to lines between these two states generally reside on the circle with radius (2.29). Many of them depart from this circle due to collisions. At current values of $0.55 < \gamma < 0.7$ there is a parametric resonance $2\Omega = \omega_+(q)$, which belong to the set of weak resonances and does not evolve into a global instability. However it is possible that a slight variation of control parameters (e.g. decreasing the damping α) might change these resonances into strong ones. Then one can expect sudden instabilities of the breather state at these large current values. In this case the global instability is realized when one of the localized multipliers collides with the $\omega_+(q)$ band around $\gamma = 0.48$. Subsequent lowering of the current leads to a fast escape of this multiplier from the unit circle and to the observed switching.

The importance of localized EEs for the destabilization of a breather is simply due to the localized nature of the latter. It is hard (if not impossible) for a breather to generate a

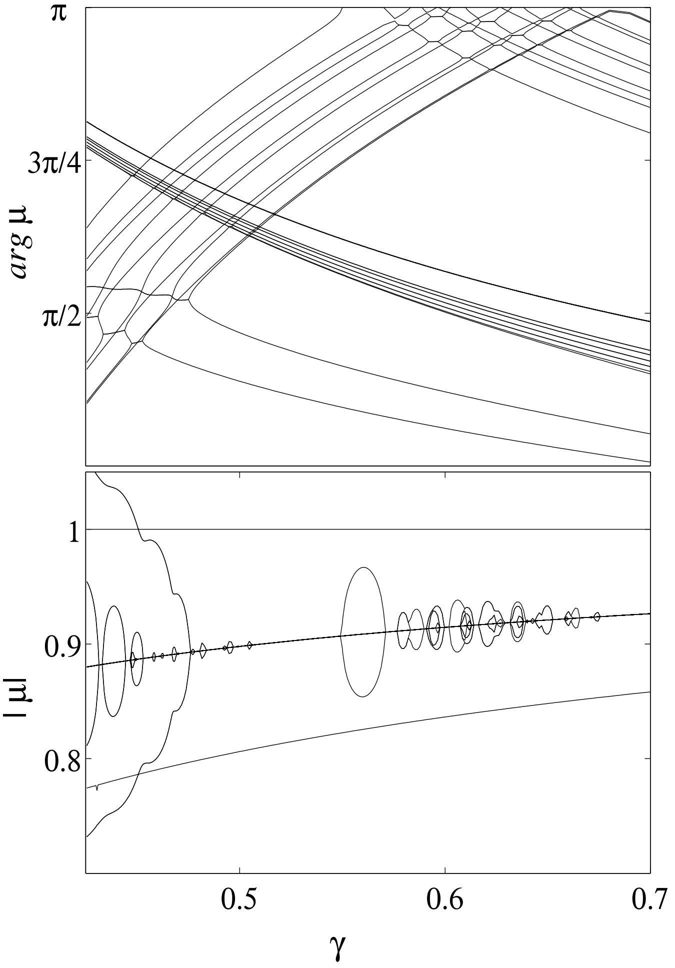

Figure 3.1: Arguments and absolute values of Floquet multipliers versus γ for the breather state in Fig. 2.11.

parametric instability through extended EWs alone, as these excitations are damped out far from the breather center. In contrast localized EEs do not travel away from the breather center. These modes can be effectively excited by the breather, leading to an instability of the latter.

Motivated by the above findings the $I-V$ characteristics of the HWS was investigated upon lowering the current. We remind that in this state *all* vertical junctions are resistive and *all* horizontal ones are superconducting. Usually it is assumed that the HWS loss is again due to a standard retrapping mechanism. It is important that any numerical simulation of such a process is done with the addition of some weak noise, because the processor will otherwise perform a perfect simulation of a single junction repeated $N+1$ times. The chosen parameters are $\beta_L = 3$ and $\eta = 0.35$. The $I-V$ characteristic is shown by a thick dashed line in Fig. 2.11. The expected retrapping current $4\alpha/\pi = 0.127$ is clearly not reached. Instead, the HWS switches to the superconducting state at $\gamma = 0.273$. At the same time it follows from equations (1.26) that the HWS exists as a solution down to the retrapping current of a single Josephson junction, i.e. down to $\gamma = 0.127$! So in this case it is possible to conclude that the numerically observed loss of the HWS at $\gamma = 0.273$ is *due to an instability.* The HWS continues to exist as a solution down to the standard retrapping current, but it is *unstable.* This novel result is very important, since very often the current value of the HWS loss in the absence of a magnetic field is used to estimate different parameters of the system *assuming* that the HWS is behaving similar to a single Josephson junction.

To understand the nature of the observed instability of the HWS its Floquet multipliers are plotted in Fig. 3.2. As in the previous plot, there are weak parametric resonances of the upper EW band at current values $\gamma \sim 0.38$ which do not evolve into a global instability. The observed instability is driven by a combination resonance at $\gamma = 0.273$. Since the HWS is an extended state, all Floquet multipliers are also extended. The combination resonance is due to the collision of two Floquet multipliers belonging to the two EW branches $\omega_{\pm}(q)$ with $q = \pi$ (it should be noted here that the EW spectrum of the HWS is different from that of the superconducting state and can be obtained by putting $\gamma = 1$ in (1.35)). Indeed for the present case, the frequency of the HWS at the instability equals 2.73, while the value of the combination $\omega_-(\pi)+\omega_+(\pi) = 2.69$. For current values $\gamma \sim 0.18$ the HWS is becoming *stable* again. However around $\gamma = 0.17$ another even stronger instability due to parametric resonance sets in, which brings the HWS to the next instability well above the expected retrapping current.

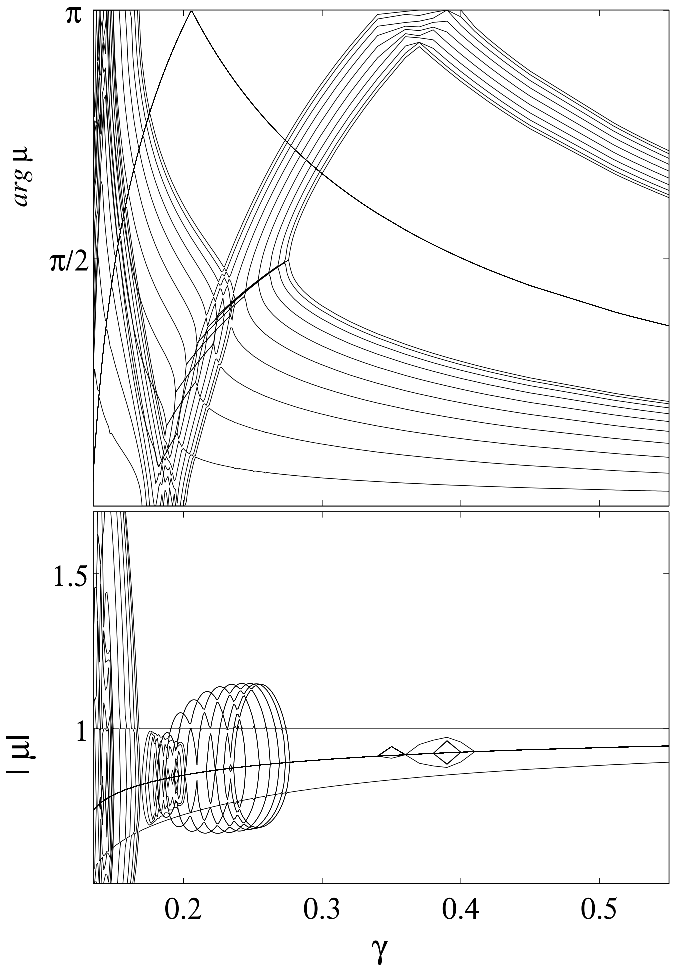

Figure 3.2: Arguments and absolute values of Floquet multipliers versus γ for the HWS in Fig. 2.11.

4 Other possible localized states

Far from any resonances the breather state is absolutely periodic with the period $T = 2\pi/\Omega$. As was shown above, close to the (primary) resonant region, a breather can switch to the *resonant* state when the amplitudes of ac libration of the Josephson phases are increased. This is still a periodic state with strong higher harmonics (which match the resonant condition $\omega_q = m\Omega$). But it is possible also to switch to an *aperiodic* state which is characterized at least by *two* frequencies Ω_1 and Ω_2.

4.1 Commensurate dynamics

In real experiments there is always noise. In order to test the influence of small fluctuations on the $I - V$ curves all simulations were repeated in the presence of small noise with amplitude $\approx 10^{-8}$. All obtained results are stable *except* the switching outcome in Fig. 2.11 . While this switching occurs at the same current value, the breather state is changed. In particular it switches to the left-right symmetry breather with three junctions being in the resistive state. Thus there may be extreme sensitiveness of the outcoming breather structure (including its symmetries) to small fluctuations. This implies that the boundaries of the volumes of attraction of different attractors (breathers) are entangled in a very peculiar way. We can reliably predict the switching position, but not the outcome of the switching.

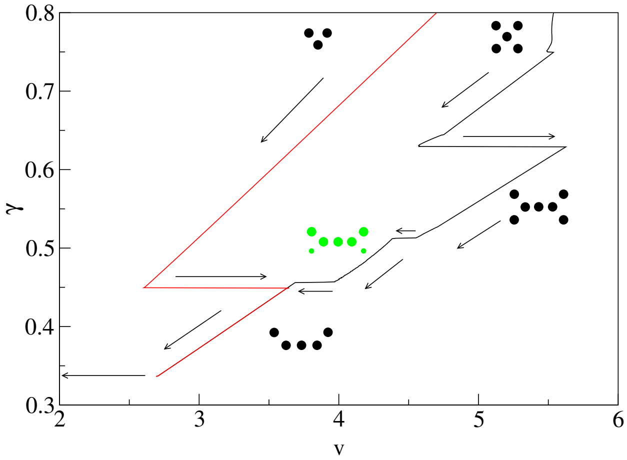

Figure 4.1: $I - V$ characteristics for $\alpha = 0.1$, $\beta_L = 3.0$, $\eta = 0.35$ in the presence of small noise and for different types of breathers. One can observe the different outcome ot the switching compared to Fig. 2.11 and the novel breather state with commensurate ratio of voltage drops across horizontal junctions (green circles).

The novel breather state (green circles) is periodic with commensurate ratio between average voltage drop across up and down horizontal junctions $2\phi^h = 3\tilde{\phi}^h$. The possibility of existence of such a state was predicted in [13].

Another initial state with up-down symmetry also shows the switching to this commensurate state, which may serve as a proof that this state is quite general. But it still was not observed in experiments.

4.2 Incommensurate resonant breather

All symmetry considerations aboved concern the symmetry of the average voltage drop distribution across the junctions. The symmetries of the time-resolved dynamics may be lower. Indeed, if we take a breather with 'up-down' symmetry with one vertical junction being in resistive state, it is possible to find such values of parameters when there are *two* breathes with the same dc voltage drop for some interval of dc bias γ and, therefore, they have the identical slope in $I-V$ curve, but different relative phase shifts of horizontal junctions at the core $\langle \phi_0^h + \tilde{\phi}_0^h \rangle$: for one of them it equals to π for another to $-\pi$.

In Fig. 4.2 the $I-V$ curves for these two states are represented for the case when $\alpha = 0.0025$, $\beta_L = 0.378$ and $\eta = 0.49$. Two curves coincide up to the resonant value of the dc bias γ. After that they switch to slightly different states and continue to be roughly similar.

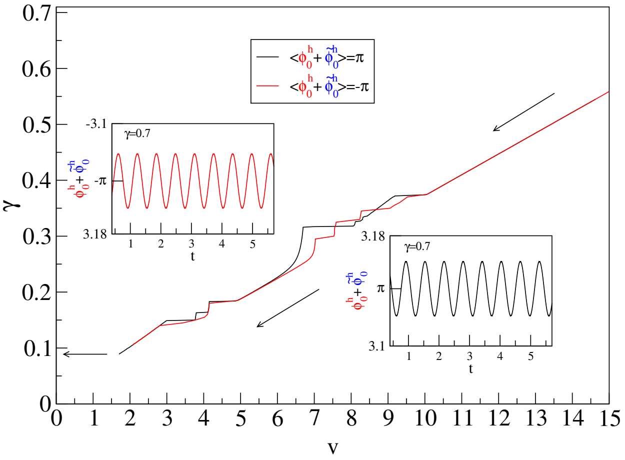

Figure 4.2: $I-V$ characteristic for two breathers, which initially possess the same average voltage drop distribution, but different average phase shifts between horizontal junctions. The two $I-V$ curves look quite similar except for the resonant region.

The Floquet analysis shows that the breather with full dynamical 'up-down' symmetry (zero phase shift) exists but becomes unstable for such chosen parameters. These other two states are stable at the same time. The equivalence of an average voltage drop distribution implies that these two states possess the same energy.

It is possible to estimate numerically the value of the barrier between the two stable states by means of an external white noise. The aim is to find such a value of the amplitude of the noise A_{noise} when the switching between these state will arise. For weak noise with amplitude $A_{noise} \approx 10^{-5}$ there are just small oscillations around of this state with typical frequency $\omega \approx 0.02\omega_{pl}$.

For moderate noise $A_{noise} = 0.175 \cdot 10^{-3}$ there are switchings and the small barrier between these states can be estimated as

$$U_0 \approx E_J \left(\frac{\alpha(1+\eta)}{\gamma} \right)^2 \ll E_J \, , \tag{4.1}$$

where $E_J = \frac{\hbar I_c}{2e}$ is the energy of a small Josephson junction.

The most interesting fact is that both states switch to the state with *incommensurate* (aperiodic) dynamics, which corresponds to the part of the $I-V$ curve on Fig. 4.2 with different (nonresonant) slope then for large value of dc bias γ. In order to analyze this phenomenon it is enough to consider one of these states (e.g. with $\langle \phi_0^h + \tilde{\phi}_0^h \rangle = \pi$).

The switching happens due to a primary resonance $\omega_{q_l} = \Omega$ between the breather and EW's for $\gamma \approx 0.38$. Thus in the region of the dc bias current $0.31 < \gamma < 0.38$ the up-down symmetry of

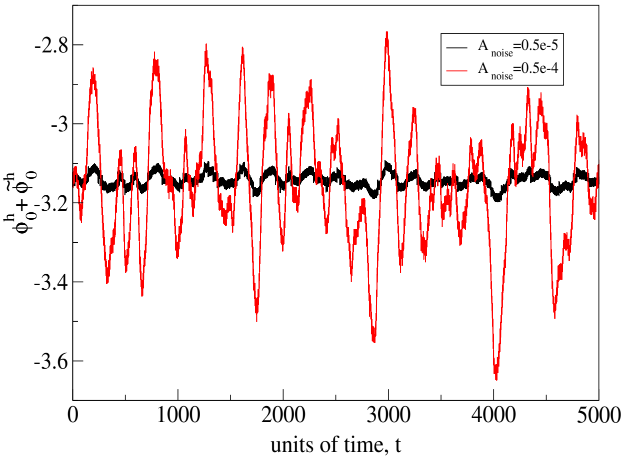

Figure 4.3: Time evolution of the phase shift between resistive junctions of DB for small amplitude noise and fixed value of dc bias $\gamma = 0.7$. For such noise there is no switching between two states.

the dc voltage pattern is violated and a novel resonant breather like state with incommensurate (aperiodic) dynamics appears. Indeed, as the system jumps to this state there are at least two incommensurate frequencies, namely $\Omega_1 \simeq 3.4$ and $\Omega_2 \simeq 5.3$. Moreover, with decreasing dc bias the value of Ω_1 practically does not change, in contrast to Ω_2. A closer look at the I-V curves of the horizontal junctions (see Fig. 4.5b) also shows that the upper (lower) horizontal junctions display the resonant (non-resonant) behavior. Thus we can conclude that this novel incommensurate breather-like state can be viewed as a coexistence of resonant and non-resonant junction behavior in the JJL. It should be noted here that similar aperiodic breather states were found in a wide range of parameters $\beta_L \simeq 1$ and $\eta \leq 1$.

By making use of a dc analysis [115, 88], i.e. neglecting ac components of the Josephson current, it is found that the voltage jumps ΔV_h and $\Delta\tilde{V}_h$ of the non-resonant and resonant horizontal junctions have to satisfy the relationship:

$$\Delta V_h = \frac{\Delta\tilde{V}_h}{1+2\eta} \tag{4.2}$$

Moreover, the presence of the incommensurate resonant breather state is characterized by a lower resistance $\propto (\alpha(2\eta+1))^{-1}$ as compared to the non-resonant case. Indeed, the simulations show that the dc voltage jump of the lower horizontal junctions is approximately two times smaller than the corresponding dc voltage jump of the upper horizontal junctions, in full accordance with the dc analysis.

In order to characterize an incommensurate breather state more precisely the Fourier transform was applied to the time dependent voltage $\dot{\phi}_1^v(t)$ of the vertical junction (see Fig. 4.6), which is in the superconducting state and the closest one to the core of the breather. If the breather state is the periodic one , i. e. for large (see Fig. 4.6a) and small (see Fig. 4.6c) values of dc bias current, the Fourier transform contains the breather frequency Ω and higher harmonics. However, in the intermediate region of the dc bias as the breather displays incommensurate dynamics, the Fourier transform becomes more rich (see Fig. 4.6b). There are two different harmonics Ω_1 and Ω_2, and the various combination frequencies $m\Omega_1 + n\Omega_2$, where n and m are integers. The incommensurate breather-like state was also observed in experiments in Nb-based Josephson junction ladders (see Fig. 4.7). The measured $I-V$ curve qualitatively looks similar to the current-voltage characteristic obtained in numerical simulations. In spite of small differences, such as a tiny voltage difference between upper and lower horizontal junction in the bias region above the incommensurate state, the last one was observed under various experimental conditions, which were partly influenced by magnetic fields.

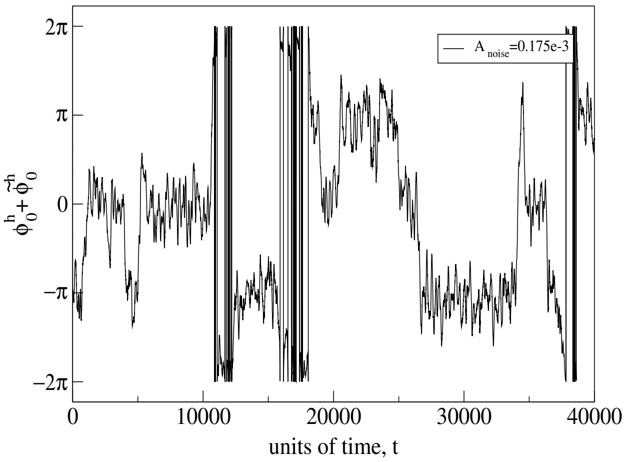

Figure 4.4: Time evolution of the phase shift between resistive junctions of a DB for moderate noise and fixed value of dc bias $\gamma = 0.7$. There are switchings between the two states.

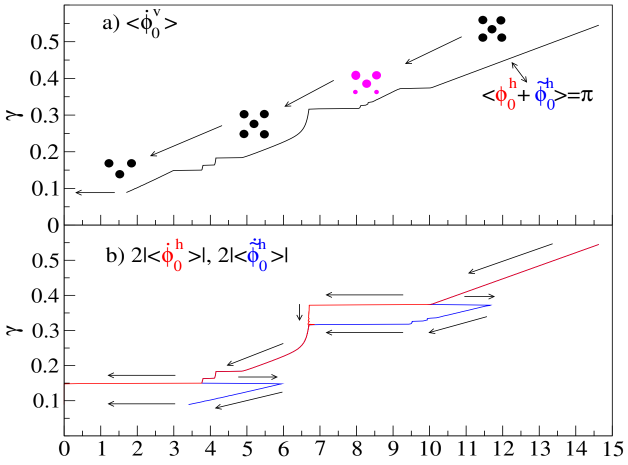

Figure 4.5: $I-V$ curve for one of the DBs from Fig. 4.2, namely for the case $\langle \phi_0^h + \tilde{\phi}_0^h \rangle = \pi$. In the upper figure (a) $I-V$ curve for the vertical resistive junction is shown, and in the down (b), for the upper (blue) and down (red) horizontal junctions in the resistive state. The doubled value of the averaged voltage drop for the horizontal junction is used in the plot.

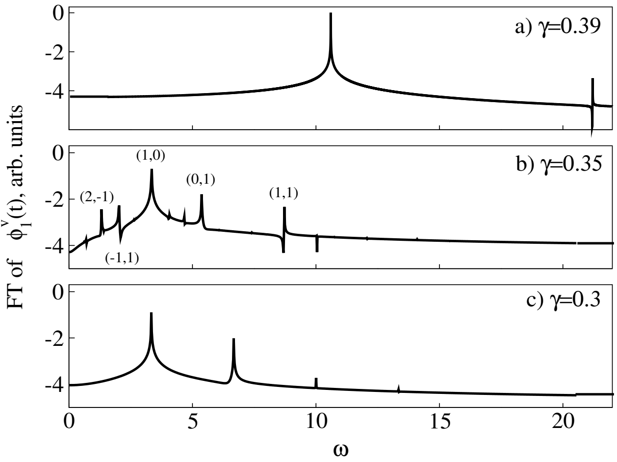

Figure 4.6: The Fourier transform (FT) of the ac voltage $\dot{\phi}_1^v(t)$. Three different values of dc bias current are shown and the logarithmic scale for FT was used.

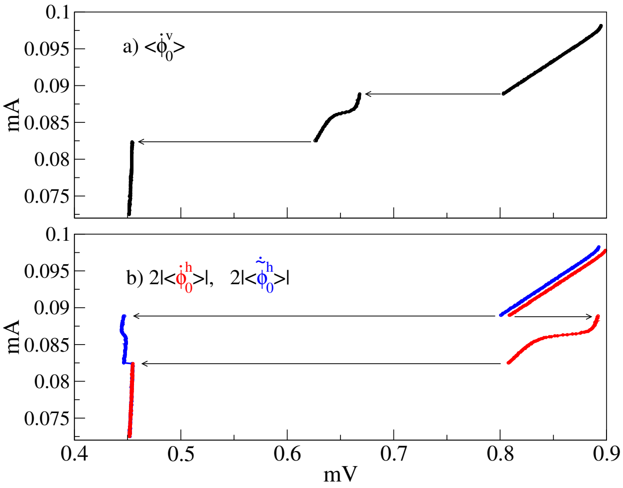

Figure 4.7: Measured *I*-*V* curves of an initially symmetric breather state created at a dc bias of $\gamma = 0.4$: (a) voltage drop across vertical junction, (b) voltage drops across upper (thin solid line) and lower (dashed line) left horizontal junctions. The breather state with incommensurate voltages is formed for $0.34 < \gamma < 0.37$.

Summary of Part II

By using symmetry considerations the classification of DBs in JJLs was done. Far from any resonances the frequency of the breathers is determined only by the parameters of the system. Close to resonances the dynamics of DBs becomes highly nonlinear. The presence of dissipation gives the possibility to tune DBs into resonances. There are three types of resonances: primary, parametric and combinational. In primary and parametric resonances only frequencies of DBs and plasmons take part. In the case of combinational resonance, the frequency of a localized mode, generated by the DB is crucial. These resonances allow to study the interaction between DBs and plasmons by the inverse spectroscopy method. For weak resonances breathers preserve their stability. They manifest themselves through the increasing of the amplitude of ac librations in the breather tails. Thus, this phenomenon allows to identify the resonant excitations with the cavity modes of the system. Strong resonances destroy the stability of DBs and result in the switchings to other stable states. It can be a DB again, HWS or superconducting state. For some range of parameters, the switching to aperiodic spatially localized states was observed. All these results are in a very good agreement with experimental data. Finally, the instability of HWS is studied. The dynamics of HWS does not coincide with the one of SJJ. The spatial extension leads to the resonance with plasmons. Recently this was confirmed experimentally.

Conclusion

The concept of DBs is still under development due to an increasing number of experimental observations. Many open questions remain: mobility of discrete breathers [34, 79, 85], targeted energy transfer [71] are only few of them.

In the present work the interaction between discrete breathers and small amplitude plane waves is studied by means of spectroscopic methods. In Hamiltonian lattices, where plane waves can freely propagate, the *transport spectroscopy* method was used. A DB corresponds to a local time-periodic scattering potential. Time periodicity allows to decompose DB into a set of open and closed channels. The most interesting question concerns the role of closed channels. The transmission coefficient was computed for acoustic and optical Hamiltonian systems on the basis of a generalized numerical scheme (see Appendix A.3). Numerical results show that the presence of closed channels leads, in general, to a suppression of the transmission. But there is still a possibility to observe *perfect transmission*. It exists due to local levels, generated by a breather, and is similar to resonant transmission by static scattering potentials. The presence of closed channels manifests itself only in a renormalization of the position of the resonance. *Perfect reflection* was observed as well. A detailed analysis of this phenomenon shows that the role of closed channels is of crucial importance. It has a resonant behavior and is similar to the Fano resonance in atomic systems, but it does not affect the stability of breathers. This is the main difference between static and time-periodic scattering potentials and thus this phenomenon can be used by experimentalists in order to examine the presence of DBs in the system.

Some results for one-channel scattering processes, which were discussed here, can be applied to heat conductivity (phonon transport) in 1D systems [99, 72, 73]. By thermalizing the lattice a spontaneous creation of DBs is possible [39, 117, 51, 100]. As scattering centers they will affect the conductivity. But the interaction between nonlinear phonons and DBs and many-channels scattering set ups should be taken into account. Both of them are inelastic processes and, therefore, can destroy the breather, during interactions.

The next possible task is the scattering with many open channels, in systems with several phonon bands and generalization to higher lattice dimensions.

In dissipative systems plane waves can not freely propagate. They will decay in space. But DBs can generate extended states in the tails at the resonances. It allows to apply the *inverse spectroscopy* method. This method was used in order to study the interaction between plasmons and DBs in Josephson junction ladders.

First of all the classification of diversity of DBs was done by using symmetry considerations. The obtained approximations for the frequency of DB far from any resonances can be used as initial conditions for the desired type of breather. Their stability is checked with the help of Floquet theory. The analysis of Floquet multipliers gives three resonant conditions which may lead to the loosing of stability of DBs and consequent switchings (jumps) to other states. Depending on the DB internal symmetry, these new states could be periodic (superconducting, HWS, resonant DB) or aperiodic, but still localized. The case when two DBs with different phase shifts between resistive junctions exist, but with the same time-average structure (with the same energy), was the issue of special interest. They both switch to the aperiodic states which were also observed in the experiment. By applying external white noise the height of effective barrier is estimated. Finally, the instability of HWS is studied. The dynamics of HWS does not coincide with the SJJ one. The spatial extension leads to the resonance with the plasmons and was recently observed in experiments.

A resonant DB can be used as generator of microwave radiation. A straightforward application is to study the scattering of waves by DBs in JJLs, by putting two breathers into a ladder and tuning on of them into a resonance. The tuning is possible by a local change of the dc bias. Following the above consideration about the Fano resonance, one can conclude that the suppression of the transmission should be also observed in such systems. It could be used for constructing a tunable frequency filter.

In general, besides the existence of DBs, nonlinear systems possess other interesting phenomena as well. And all methods, investigated here, can be used also to study some of these phenomena. Below, several applications to different topics will be briefly mentioned.

Discrete breathers in one-dimensional Hamiltonian lattices are *time-reversal* states. Therefore, it does not matter in the scattering problem from which side plane waves are sent into the breather. The transmission from left to right T^{LR} is equal to the transmission from right to left T^{RL}. If the time-reversal symmetry of time-periodic scattering potential is violated then these two transmissions can be different $T^{LR} \neq T^{RL}$. This situation can be realized in quantum systems with local potential under external electric ac field [28], for example, and it is known as a quantum pump effect [14, 109]. As a result the directed nonzero current is possible.

The generation of dc current from an external ac force with zero mean is a well known *rectification* or *ratchet* phenomenon in classical systems [10, 63, 96]. Usually it was observed in the motion of the particle in spatial periodic and asymmetric potential under periodic ac force with one harmonics. The symmetry analysis shows that it is possible to observe generation of dc currents in periodic and *symmetric* potentials, but with a proper choice of ac force with *two* harmonics [44]. This symmetry consideration was applied to spatially distributed systems. It was shown that if in the system there is a nonzero topological charge it possible to observe ratchet phenomena [45, 97]. This statement can be checked experimentally on the Josephson junction annular array with a trapped flux inside, and in the presence of an ac bias. In order to generate a dc current of the flux the ac bias with two harmonics should be applied.

On more interesting result of rectification phenomena is the zeroth harmonic generation in spin systems [40, 38]. By applying a dc magnetic field along the z direction and an ac magnetic field in the $x-z$ plane, based on symmetry analysis, it is possible to observe *static* magnetization along the y direction. The setup is similar to an NMR one, just the ac field is tilted in the $x-z$ plane with nonzero angle to the x axis.

In Appendix D the Fano-Anderson one particle model is discussed. It can be used to describe the zero-bias and zero-temperature conductance of electrons through a *quantum dot*. In 1D there are two different structures: *substitutional* and *side* dot configurations. In substitutional configurations there is a Kondo resonance and in a side dot configuration a Fano resonance [65, 15, 113]. Experimentally it was shown that by varying the strength of coupling between left and right leads of a quantum dot it is possible to observe the transition from Kondo to Fano resonance [53].

Electrons possess a spin. Therefore, there are two sorts of electrons in the Fano-Anderson model. For a zero magnetic field the Fano resonance for spin up and spin down takes place at the same energy and two spin-resolved transmission curves coincide. In the presence of a nonzero magnetic field these curves will be shifted and the zeros as well. It leads to the idea of *spin-polarized* conductance [119, 6, 101]. To be more precise the interaction of electrons inside the dot should be taken into account. It can be done by adding a Hubbard interaction [80, 58]. Numerical results show that the Fano resonance survives for each spin-resoled transmission [57]. There are just renormalizations of it's position and width [65]. As conclusion, it gives the possibility to construct spin filters based on the Fano resonance phenomenon on a side dot configuration.

Appendix A Numerical methods

A.1 Newton method

There are several methods for obtaining a DB state up to some precision. All of them use the fact that the DB is a periodic orbit. The Newton scheme is based on the phase space representation of the DB and gives a rather good precision. In the phase space a DB is a loop or a closed trajectory. In the intersection with some hyperplane it yields a finite set of points, in the analogy with Poincare section. If the initial conditions are chosen in this plane $\{\vec{x}(0), \dot{\vec{x}}(0)\}$ after one period T_b they will return to this plane again and reproduce the initial state $\{\vec{x}(T_b), \dot{\vec{x}}(T_b)\} = \{\vec{x}(0), \dot{\vec{x}}(0)\}$. But if the initial conditions are not exactly on the loop (perturbed a bit) $\{\vec{x}^{\epsilon}(0), \dot{\vec{x}}^{\epsilon}(0)\} = \{\vec{x}(0), \dot{\vec{x}}(0)\} + \vec{\epsilon}$ then after one period they will not coincide with themselves $\{\vec{x}^{\epsilon}(T_b), \dot{\vec{x}}^{\epsilon}(T_b)\} \neq \{\vec{x}^{\epsilon}, \dot{\vec{x}}^{\epsilon}(0)\}$. In other words, the periodic orbits with period T are the zeros of the following operator

$$\mathcal{N}(\vec{x}(0), \dot{\vec{x}}(0)) = \begin{pmatrix} \vec{x}(0) \\ \dot{\vec{x}}(0) \end{pmatrix} - \begin{pmatrix} \vec{x}(T) \\ \dot{\vec{x}}(T) \end{pmatrix} \tag{A.1}$$

In order to find zeros numerically, it is possible to expand the expression for $\mathbf{N}$ into a Taylor series up to the first order

$$\vec{N}(\vec{X}) = \vec{N}(\vec{X}^0) + \mathbf{M}(\vec{X} - \vec{X}^0) \tag{A.2}$$

where $\vec{X} = \{\vec{x}, \dot{\vec{x}}\}$ and

$$M_{nm} = \frac{\partial N_n}{\partial X_m}|_{\vec{X}^0} = \frac{\partial X_n(T)}{\partial X_m}|_{\vec{X}^0} - \delta_{nm} \tag{A.3}$$

is the matrix of the first derivatives of $\mathcal{N}$. This equation (A.2) can be considered as an equation for initial conditions $\vec{X}$. Taking the initial guess $\vec{X}^0$ with $\vec{N}(\vec{X}^0) \neq 0$ it is possible to obtain a better approximation $\vec{X}$ using the condition that $\vec{N}(\vec{X})$ should be be equal to zero

$$\vec{X} = \vec{X}^0 - \mathbf{M}^{-1}\vec{N}(\vec{X}^0) \tag{A.4}$$

and repeat (A.4) until $\|\vec{N}\|$ will be smaller than 10^{-15}.

This method allows to obtain different types of DB with high accuracy using a good initial approximation. Such an approximation can be obtain from the anticontinuous limit, from the given DB by slightly varying control parameter (frequency, coupling, etc.). In the case of Josephson junction ladders, DBs are attractors. Using the approximation for the frequencies of different types of DBs (2.6-2.8) it is better to integrate the system for some amount of time, when the tragectory will approach the attractor with some accuracy, and only then to use a Newton scheme, just to increase the accuracy.

High accuracy of DB allows to study its stability by the Floquet method.

A.2 Stability analysis

The analysis of stability is done by using the Floquet theory. The first step is to compute the Floquet matrix

$$\begin{pmatrix} \vec{\epsilon}(T_b) \\ \dot{\vec{\epsilon}}(T_b) \end{pmatrix} = \mathbf{F} \begin{pmatrix} \vec{\epsilon}(0) \\ \dot{\vec{\epsilon}}(0) \end{pmatrix} \tag{A.5}$$

where $\{\vec{\epsilon}, \dot{\vec{\epsilon}}\}$ are small fluctuations around the DB (1.8). The computation of $\mathbf{F}$ is similar to $\mathbf{M}$, indeed

$$\mathbf{F} = \mathbf{M} + \mathbf{E} \tag{A.6}$$

where $E_{nm} = \delta_{nm}$. It means that it is possible to take a DB $\vec{X}^b(0)$, which was obtained by a Newton scheme, perturb it in some direction $X_i'(0) = X_i^b(0) + \epsilon_i$ and then integrate over one period T_b, which gives

$$F_{ji} = \frac{1}{\epsilon_i}(X_j'(T_b) - X_j^b(T_b)) \tag{A.7}$$

After that, one should obtain the eigenvalues of $\mathbf{F}$. It is a general real matrix, therefore the eigenvalues will be complex, in general. The DB solution is stable if the absolute value of all eigenvalues is less then 1. Due to the time periodicity of the DB there is always one eigenvalue which equal to $+1$.

A.3 Transmission coefficient

To compute the transmission coefficient a numerical scheme was developed, which generalizes the one given in Ref. [19] (which relies on a spatial reflection symmetry of the breather and thus of the scattering potential). At variance with Ref. [19] this scheme is capable of dealing with any (perhaps spatially nonsymmetric) time-periodic scattering potential.

Let us look for solutions of Eq. (1.8) which correspond to zeroes of the operator

$$\mathcal{G}(\vec{\epsilon}(0), \dot{\vec{\epsilon}}(0)) = \begin{pmatrix} \vec{\epsilon}(0) \\ \dot{\vec{\epsilon}}(0) \end{pmatrix} - e^{i\omega_q T_b} \begin{pmatrix} \vec{\epsilon}(T_b) \\ \dot{\vec{\epsilon}}(T_b) \end{pmatrix} \tag{A.8}$$

on a lattice with $2N+1$ sites labelled $-N, (-N+1), ..., -1, 0, 1, ...(N-1), N$. The incoming wave is fed from the left, and the transmitted wave is leaving the system to the right. The boundary condition at the right end is $\epsilon_{N+1} = e^{-i\omega_q t}$, which implies that the transmitted wave will have amplitude 1. With a given boundary condition at the left end $\epsilon_{-N-1} = (A + iB)e^{-i\omega_q t}$, where A and B are real numbers, one may find the zeroes of Eq. (A.8) using a standard Newton routine. Due to the linearity of the equations of motion in ϵ an arbitrary initial guess and one Newton step are needed to converge to the zeroes. In practice due to roundoff errors an additional Newton step may be required.

However with arbitrary A and B we will not realize the scattering case in general. This is due to the fact that all extended Floquet states of an infinite system are twofold degenerated because time reversal symmetry holds far from the breather center. To succeed a second Newton procedure which uses A and B as free parameters was added, such that the solution on site N becomes $\epsilon_N = e^{-iq - i\omega_q t}$, ensuring that we realize a single transmitted travelling wave of amplitude one at the right end of the system. After the Newton procedures are completed, the transmission coefficient is given by

$$T_q = \frac{4\sin^2 q}{|(A + iB)e^{-iq} - \zeta_{-N}|^2}. \tag{A.9}$$

While the Bloch functions ζ_n are in general time-dependent close to the breather center, they will be time-independent complex numbers at large distance from the breather. It should be note that the computation operates at the machine precision, and we obtain results which are size independent, i.e. with the above described boundary conditions we emulate an infinite system. The discrete breather solution itself has to be obtained beforehand using standard numerical procedures [18].

The enumerator in (A.9) vanishes at the extremal values of ω_q, i.e. at $q = 0$ and $q = \pi$. If the denominator is finite at these values of q, the transmission will also vanish. This is indeed the generic case for a quadratic dependence of the spectrum ω_q on q around these points. Exceptions are expected for acoustic chains.

Another peculiar point is that if upon changing some control parameter, e.g. the breather frequency, a localized Floquet eigenstate attaches to or disattaches from the extended Floquet spectrum, the transmission coefficient will be exactly $t = 1$ for the q-value which corresponds to the edge of the spectrum ω_q, i.e. $q = 0$ or $q = \pi$ [19, 68].

Appendix B Conservation of the momentum $\tilde{J}$

Let us multiply both sides of the linear equation

$$\begin{aligned} \ddot{\epsilon}_n &= -W''[\hat{x}_n(t) - \hat{x}_{n-1}(t)](\epsilon_n - \epsilon_{n-1}) \\ &\quad + W''[\hat{x}_{n+1}(t) - \hat{x}_n(t)](\epsilon_{n+1} - \epsilon_n) - V''[\hat{x}_n(t)]\epsilon_n \end{aligned} \tag{B.1}$$

by ϵ_n^* and take the imaginary part

$$\mathrm{I}m(\ddot{\epsilon}_n \epsilon_n^*) = W''[\hat{x}_n(t) - \hat{x}_{n-1}(t)]\mathrm{I}m(\epsilon_{n-1}\epsilon_n^*) + W''[\hat{x}_{n+1}(t) - \hat{x}_n(t)]\mathrm{I}m(\epsilon_{n+1}\epsilon_n^*) \ . \tag{B.2}$$

The left hand side can be rewritten as

$$\mathrm{I}m \ddot{\epsilon}_n \epsilon_n^* = \mathrm{I}m \frac{d}{dt} \dot{\epsilon}_n \epsilon_n^* \tag{B.3}$$

and after averaging Eqs.(B.2) over time, one gets

$$\langle W''[\hat{x}_n(t) - \hat{x}_{n-1}(t)]\mathrm{I}m(\epsilon_n^* \epsilon_{n-1})\rangle = \langle W''[\hat{x}_{n+1}(t) - \hat{x}_n(t)]\mathrm{I}m(\epsilon_{n+1}^* \epsilon_n)\rangle \equiv -\tilde{J} \tag{B.4}$$

that the momentum $\tilde{J}$ is independent of the lattice site n.

Appendix C Time-averaged scattering potentials of breathers

C.1 Acoustic breather

It is enough to take into account the oscillations of two lattice sites in the center of a DB only. These oscillations evolve exactly in antiphase with large amplitudes. The effective Hamiltonian is written as

$$E = \frac{\dot{x}_1^2}{2} + \frac{\dot{x}_2^2}{2} + \frac{1}{4}(x_1^4 + x_2^4 + (x_1 - x_2)^4) \tag{C.1}$$

and with $x_1 = -x_2$, leads to a single oscillator problem with energy

$$E = \dot{x}^2 + \frac{9}{2}x^4. \tag{C.2}$$

The frequency of oscillation (the breather frequency) is given by

$$\frac{1}{\Omega_b} = \frac{2}{\pi}\int_0^{x_m} \frac{dx}{\sqrt{E - \frac{9}{2}x^4}}, \tag{C.3}$$

where $x_m = \sqrt[4]{\frac{2E}{9}}$. After integration gives

$$\Omega_b = \frac{2\pi\sqrt[4]{\frac{9E}{2}}}{B(\frac{1}{4}, \frac{1}{2})}, \tag{C.4}$$

where $B(x, y)$ is the B-function [54]. Next the value of $X = \sqrt{3\langle x^2\rangle}$ can be computed. It is possible to express $\langle x^2\rangle$ in terms of the energy

$$\langle x^2\rangle = \frac{2\Omega_b}{\pi}\int_0^{x_m} \frac{x^2 dx}{\sqrt{E - \frac{9}{2}x^4}}. \tag{C.5}$$

After some algebra one obtains $\langle x^2\rangle = \sqrt{\frac{2E}{9}}\frac{B(\frac{1}{2},\frac{3}{4})}{B(\frac{1}{4},\frac{1}{2})}$ and

$$X = \sqrt{\frac{2}{3\pi}}\Omega_b. \tag{C.6}$$

C.2 Acoustic rotobreather

In order to calculate the time-averaged off-diagonal hopping terms the central site will be taken into account which is in a rotational state, denoted by ϕ, and two nearest neighbor oscillators (denoted by α_1 and α_2). The total mechanical momentum is conserved. By using the symmetry it is possible to put $\alpha_1 = \alpha_2 \equiv \alpha$. The energy of such a system is

$$E = \dot{\alpha}^2 + \frac{\dot{\phi}^2}{2} + 2(1 - \cos(\phi - \alpha)). \tag{C.7}$$

The two equations of motion are given by

$$\begin{aligned} \ddot{\phi} &= -2\sin(\phi-\alpha), \\ \ddot{\alpha} &= \sin(\phi-\alpha). \end{aligned} \tag{C.8}$$

Introducing new variables $u = \phi + 2\alpha$ and $w = \phi - \alpha$ we rewrite the system (C.8) as

$$\begin{aligned} \ddot{u} &= 0, \\ \ddot{w} &= -3\sin w. \end{aligned} \tag{C.9}$$

The relevant energy part is

$$\tilde{E} = \frac{\dot{w}^2}{2} + 3(1-\cos w). \tag{C.10}$$

Now the average coupling between rotational and oscillatory states for large frequencies can be computed

$$\epsilon = \langle \cos w \rangle = \frac{\Omega_b}{2\pi\sqrt{2\tilde{E}}} \int\limits_0^{2\pi} \frac{\cos w \; dw}{\sqrt{1-\frac{3(1-\cos w)}{\tilde{E}}}}. \tag{C.11}$$

Because $\tilde{E} \approx \frac{\Omega_b^2}{2}$, it gives

$$\epsilon \approx \frac{\Omega_b}{2\pi\sqrt{2\tilde{E}}} \int\limits_0^{2\pi} (1 + \frac{3(1-\cos w)}{2\tilde{E}}) \cos w \; dw \tag{C.12}$$

which leads to

$$\epsilon = -\frac{3\Omega_b}{4\sqrt{2}\tilde{E}^{3/2}} \tag{C.13}$$

and finally to

$$\epsilon = -\frac{3}{2\Omega_b^2}. \tag{C.14}$$

Appendix D Fano-Anderson model

In order to understand how the Fano resonance appears in the transmission line it is useful to analyze the so-called Fano-Anderson model [80]. This is a simplest model were the observation of the perfect reflection is possible.

The Hamiltonian of the system

$$H = \sum_i C(\phi_i \phi_{i-1}^\dagger + c.c) + E\varphi\varphi^\dagger + \epsilon(\phi_0\varphi^\dagger + c.c). \tag{D.1}$$

The first term in (D.1) describes the tight-binding with the hopping C between nearest sites. The second term is the *additional* level with energy E and the third term represents the coupling between the system and additional level.

The Schrödinger equation gives the following set of equations

$$\begin{aligned} i\dot{\phi}_n &= C(\phi_{n-1} + \phi_{n+1}) + \epsilon\varphi\phi_n\delta_{n0} \ , \\ i\dot{\varphi} &= E\varphi + \epsilon\phi_0 \ . \end{aligned} \tag{D.2}$$

When $\epsilon = 0$ the system (D.2) consists of the pure chain with hopping with energy spectrum $\omega_q = -2C\cos q$ and an additional level with energy E. The level E is chosen such that it lies inside the spectrum $|E| < 2C$. This system possesses one conducting channel and for such condition any energy from the spectrum freely propagates with perfect transmission.

For the case $\epsilon \neq 0$ there is one local defect at $n = 0$ in the propagating channel. Due to the gauge invariance of the Schrödinger equation (D.2) it is possible to eliminate the time dependence and to introduce new variables

$$\begin{aligned} \phi_n &= A_n e^{i\omega_q t} \ , \\ \varphi &= B e^{i\omega_q t} \ . \end{aligned} \tag{D.3}$$

The eqs.(D.2) in the ansatz (D.3) become

$$\begin{aligned} -\omega_q A_n &= C(A_{n-1} + A_{n+1}) + \epsilon B\delta_{n0} \\ -\omega_q B &= EB + \epsilon A_0 \ . \end{aligned} \tag{D.4}$$

From the second equation in (D.4) it is possible to eliminate B as $B = -\frac{\epsilon A_0}{\omega_q - E}$ and then substitute it into the first one

$$-\omega_q A_n = C(A_{n-1} + A_{n+1}) - \frac{\epsilon^2 A_0}{\omega_q + E}\delta_{n0} \ . \tag{D.5}$$

Note here, that the system (D.5) possesses *the resonant* scattering potential. It means that the potential depends on the incoming energy. And moreover, if the energy of the additional level is inside the spectrum $|E| < 2C$, there is a q_F such that $E = -\omega_{q_F}$ and the denominator of the second term in the rhs of (D.5) vanishes. The potential becomes infinite and therefore there is perfect reflection exactly for this value of incoming energy.

As before the transmission coefficient is computed by means of the matrix approach. Due to locality of the defect it is enough to take into account only one matrix, namely

$$\begin{pmatrix} a & -1 \\ 1 & 0 \end{pmatrix} , \tag{D.6}$$

$$a = -\frac{\omega_q}{C} - \frac{\epsilon^2}{C(\omega_q + E)}.$$

By using formula (1.22) it is possible to obtain the transmission coefficient

$$T = \frac{4\sin^2 q}{|ae^{-iq} - 2|^2} \ . \tag{D.7}$$

Again when $\omega_q + E = 0$ then $a \to \infty$ and, therefore, the transmission goes to zero $T = 0$. There is no shift of the position of the zero due to the locality of coupling between the system and the additional level. But when the coupling is nonlocal, a shift of the position of total reflection takes place.

After some algebra the transmission coefficient (D.7) can be written as

$$T = \left[1 + \frac{1}{4\sin^2 q} \frac{\epsilon^4}{C^2(E + \omega_q)^2}\right]^{-1} \ . \tag{D.8}$$

Using this expression (D.8) it is possible to estimate the width of resonant total reflection. If $\frac{\epsilon^2}{2C^2} \ll \sin q$ then $T \approx 1$ and only for $q = q_F$ the transmission vanishes $T(q_F) = 0$. As usual the width of the resonance is measured at the half of height. In our case it corresponds to $T = \frac{1}{2}$ or

$$\frac{\epsilon^4}{4C^2(E + \omega_q)^2 \sin^2 q} = 1 \ . \tag{D.9}$$

In addition to this the spectrum ω_q should be expanded into a Taylor series around q_F

$$\omega_q \approx \omega_{q_F} + \frac{d\omega_q}{dq}(q_F)\delta q \ , \tag{D.10}$$

Substituting (D.10) into (D.9) and keeping in mind that $\omega_{q_F} = -E$ and $\frac{d\omega_q}{dq} = 2C\sin q$ leads to

$$\frac{\epsilon^4}{16C^4 \sin^4 q_F} = (\delta q)^2 \tag{D.11}$$

or

$$\delta q = \frac{\epsilon^2}{4C^2 \sin^2 q_F} \ . \tag{D.12}$$

The real width is just twice of the expression (D.12)

$$\Delta q = \frac{\epsilon^2}{2C^2 \sin^2 q_F} \ . \tag{D.13}$$

The typical dependence of the transmission coefficient T versus wave number q is shown in Fig. D.1 There is an exact zero at $q_F = \frac{\pi}{2}$. Others zeros at the band edges are due to violating of the translation invariance by the presence of the defect.

Note here, that this consideration is valid for the continuous case as well, when the continuous Schrödinger equation is considered with a δ-like resonant potential.

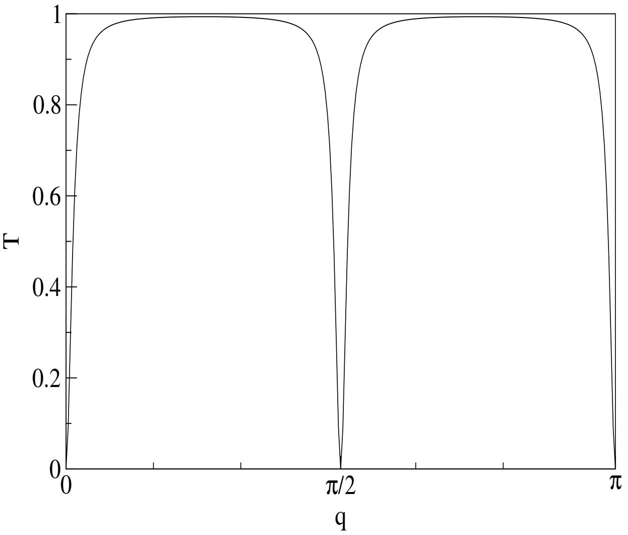

Figure D.1: Transmission coefficient versus wave number. The parameters are $q_F = \frac{\pi}{2}$, $C = 10.$ and $\epsilon = 4$. (they will be used later).

Appendix E Power of ac librations

In order to obtain an expression for the kinetic energy, the system of equations (2.11) can be written in a matrix form:

$$\hat{M}\vec{v} = 0 \; . \tag{E.1}$$

Here, $\vec{v}$ is an unknown vector

$$\vec{v} = \begin{pmatrix} A_v \\ A_h^- \end{pmatrix} \; , \tag{E.2}$$

and $\hat{M}$ is a 2×2 matrix

$$\hat{M}(\lambda) = \begin{pmatrix} m_{11}(\lambda) & m_{12}(\lambda) \\ m_{21}(\lambda) & m_{22}(\lambda) \end{pmatrix} \; , \tag{E.3}$$

where $m_{11}(\lambda) = C - \frac{2}{\beta_L}\cosh\lambda$, $m_{12}(\lambda) = -\frac{2}{\beta_L}(1 - e^{-\lambda})$, $m_{21}(\lambda) = -\frac{1}{\beta_L \eta}(1 - e^{\lambda})$, and $m_{22}(\lambda) = D$. A nonzero solution exists if the determinant of $\hat{M}$ vanishes: $\det \hat{M}(\lambda_0) = 0$. The value of λ_0 was obtained above (2.14).

The components of the vector $\vec{v}$ satisfy the condition:

$$A_v = -\frac{m_{22}}{m_{21}} A_h^- \; . \tag{E.4}$$

To determine the components A_v and A_h^- separately an additional condition should be imposed at the breather center. This condition is not known exactly due to the complex dynamics in the resistive breather center. Nevertheless the ac librations in the breather tails are weakly depending on it. One of the simplest normalization conditions is

$$|A_v|^2 + |A_h^-|^2 = 1 \; . \tag{E.5}$$

Substitution of (E.4) into (E.5) gives

$$\begin{aligned} A_h^- &= \frac{|m_{21}|^2}{\sqrt{|m_{21}|^2 + |m_{22}|^2}} \\ A_v &= -\frac{m_{22}\overline{m}_{21}}{\sqrt{|m_{21}|^4 + |m_{22}|^2 |m_{21}|^2}} \; . \end{aligned} \tag{E.6}$$

Due to the up-down symmetry in the breather tail, the dynamics of Josephson phases at the edge of the JJL can be written in the form

$$\begin{aligned} \varphi_n^v &= -\frac{Re(m_{22}\overline{m}_{21}) e^{Re(\lambda_0)n} \cos(Im(\lambda_0)n + \Omega t)}{\sqrt{|m_{21}|^4 + |m_{22}|^2 |m_{21}|^2}} + \frac{Im(m_{22}\overline{m}_{21}) e^{Re(\lambda_0)n} \sin(Im(\lambda_0)n + \Omega t)}{\sqrt{|m_{21}|^4 + |m_{22}|^2 |m_{21}|^2}} \; , \\ \varphi_n^h &= \frac{|m_{21}|^2 e^{\Re(\lambda_0)n} \cos(\Im(\lambda_0)n + \Omega t)}{\sqrt{|m_{21}|^2 + |m_{22}|^2}} ; . \end{aligned} \tag{E.7}$$

The final expression for the average kinetic energy for $n < 0$ is written as

$$\frac{1}{2}\left\langle \dot{\varphi}_n^{v^2} \right\rangle = \frac{\Omega^2 |m_{22}\overline{m}_{21}|^2 e^{Re(\lambda_0)2n}}{4(|m_{21}|^4 + |m_{22}|^2 |m_{21}|^2)} \; . \tag{E.8}$$

Bibliography

[1] A. A. Andronov, A. A. Vitt, and S. E. Chajkin, *Theory of oscillators*, New York, Dover Publ., 1987.

[2] V. I. Arnold, *Mathematical Methods of Classical Mechanics*, Springer, Berlin, 1989.

[3] S. Aubry, *Breathers in nonlinear lattices: existence, linear stability and quantization*, Physica D, 103 (1997), p. 201.

[4] S. Aubry and G. Kopidakis, *Aspects of discrete breathers and new directions*, Proceedings of NATO Advanced Research Workshop "Nonlinearity and Disorder: Theory and Applications"// cond-mat/0102162, (2001).

[5] S. Aubry, G. Kopidakis, and V. Kadelburg, *Variational proof for hard discrete breathers in some classes of hamiltonian dynamical systems*, Discrete and Continuous Dynamical Systems - Series B, 1 (2001), p. 271.

[6] Y. Avishai and Y. Tokura, *Resonant electron transmission through a finite quantum spin chain*, Phys. Rev. Lett., 87 (2000), p. 197203.

[7] P. F. Bagwell and R. K. Lake, *Resonances in transmission through an oscillating barrier*, Phys. Rev. B, 46 (1992), p. 15329.

[8] D. Bambusi, *Exponential stability of breathers in hamiltonian networks of weakly coupled oscillators*, Nonlinearity, 9 (1996), p. 433.

[9] A. Barone and G. Paterno, *Physics and Applications of the Josephson Effect*, Wiley, New York, 1982.

[10] R. Bartussek, P. Hänggi, and J. G. Kissner, *Periodically rocked thermal ratchets*, Europhys. Lett., 28 (1994), p. 459.

[11] A. Benabdallah, M. V. Fistul, and S. Flach, *Breathers in a single plaquette of josephson junctions: existence, stability and resonances*, Physica D, 159 (2001), p. 202.

[12] P. Binder, D. Abraimov, and A. V. Ustinov, *Diversity of discrete breathers observed in a josephson ladder*, Phys. Rev. E, 62 (2000), p. 2858.

[13] P. Binder, D. Abraimov, A. V. Ustinov, S. Flach, and Y. Zolotaryuk, *Observation of breathers in josephson ladders*, Phys. Rev. Lett., 84 (2000), p. 745.

[14] P. W. Brouwer, *Scattering approach to parametric pumping*, Phys. Rev. B, 58 (1998), p. R10135.

[15] B. R. Bulka and P. Stefanski, *Fano and kondo resonance in electronic current through nanodevices*, Phys. Rev. Lett., 86 (2001), p. 5128.

[16] X. D. Cao and B. A. Malomed, *Soliton-defect collisions in the nonlinear schrödinger equation*, Phys. Lett. A, 206 (1995), p. 177.

[17] P. Caputo, M. V. Fistul, A. V. Ustinov, B. A. Malomed, and S. Flach, *Cavity resonances in josephson ladders*, Phys. Rev. B, 59 (1999), p. 14050.

[18] T. Cretegny and S. Aubry, *Spatially inhomogeneous time-periodic propagating waves in anharmonic systems*, Phys. Rev. B, 55 (1997), p. R11929.

[19] T. Cretegny, S. Aubry, and S. Flach, *1d phonon scattering by discrete breathers*, Physica D, 199 (1998), p. 73.

[20] J. Cuevas, F. Palmero, J. F. R. Archilla, and F. R. Romero, *Moving discrete breathers in a klein-gordon chain with an impurity*, J. Phys. A: Math. Gen., 35 (2002), p. 10519.

[21] B. Dey, M. Eleftheriou, S. Flach, and G. P. Tsironis, *Shape profile of compact-like discrete breathers in nonlinear dispersive lattice systems*, Phys. Rev. E, 65 (2001), p. 017601.

[22] J. Dorignac and S. Flach, *Tunneling of quantum rotobreathers*, Phys. Rev. B, 65 (2002), p. 214305.

[23] J. Edler and P. Hamm, *Self-trapping of the amide i band in a peptide mode crystal*, J. Chem. Phys., 117 (2002), p. 2415.

[24] N. K. Efremidis, S. Sears, D. N. Christodoulides, J. W. Fleischer, and M. Segev, *Discrete solitons in photorefractive optically induced photonic lattices*, Phys. Rev. E, 66 (2002), p. 046602.

[25] H. S. Eisenberg, Y. Silberberg, R. Morandotti, A. R. Boyd, and J. S. Aitchison, *Discrete spatial optical solitons in waveguide arrays*, Phys. Rev. Lett., 81 (1998), p. 3383.

[26] U. Fano, *Effects of configuration interaction on intensities and phase shifts*, Phys. Lett., 124 (1961), p. 1866.

[27] M. V. Fistul, S. Flach, and A. Benabdallah, *Magnetic-field-induced control of breather dynamics in a single plaquette of josephson junctions*,

[28] M. V. Fistul, A. E. Miroshnichenko, and S. Flach, *Ac field induced quantum ratchet effect in tunnel junctions: tunneling with a broken symmetry*, Phys. Rev. B, 68 (2003), 153107.

[29] M. V. Fistul, A. E. Miroshnichenko, S. Flach, M. Schuster, and A. V. Ustinov, *Incommensurate dynamics of resonant breathers in josephson junction ladders*, Phys. Rev. B, 65 (2002), p. 174524.

[30] M. V. Fistul and J. B. Page, *Penetration of dynamic localized states in dc-driven josephson junction ladders by discrete jumps*, Phys. Rev. E, 64 (2001), p. 036609.

[31] S. Flach, *Conditions on the existence of localized excitations in nonlinear discrete systems*, Phys. Rev. E, 50 (1994), p. 3134.

[32] S. Flach, *Existence of localized excitations in nonlinear hamiltonian lattices*, Phy. Rev. E, 51 (1995), p. 1503.

[33] S. Flach and V. Fleurov, *Tunnelling in the nonintegrable trimer - a step towards quantum breathers*, J Phys. - Condes. Mat., 9 (1997), p. 7039.

[34] S. Flach and K. Kladko, *Moving discrete breathers?*, Physica D, 127 (1999), p. 61.

[35] S. Flach, K. Kladko, and S. Takeno, *Acoustic breathers in two-dimensional lattices*, Phys. Rev. Lett., 79 (1997), p. 4838.

[36] S. Flach, A. E. Miroshnichenko, and M. V. Fistul, *Wave scattering by discrete breathers*, Chaos, 13 (2003), p. 596.

[37] S. Flach, A. E. Miroshnichenko, V. Fleurov, and M. Fistul, *Fano resonances with discrete breathers*, Phys. Rev. Lett., 90 (2003), p. 084101.

[38] S. Flach, A. E. Miroshnichenko, and A. A. Ovchinnikov, *Ac-driven quantum spins: resonant enhancement of transverse dc magnetization*, Phys. Rev. B, 65 (2002), p. 104438.

[39] S. Flach and G. Mutschke, *Slow relaxation and phase space properties of a conservative system with many degrees of freedom*, Phys. Rev. E, 49 (1994), p. 5018.

[40] S. Flach and A. Ovchinnikov, *Static magnetization induced by time-periodic fields with zero mean*, Physica A, 292 (2001), p. 268.

[41] S. Flach and M. Spicci, *Rotobreather dynamics in underdamped josephson junction ladders*, J. Phys.: Condens. Matter, 11 (1999), p. 321.

[42] S. Flach and C. R. Willis, *Discrete breathers*, Phys. Rep., 295 (1998), p. 181.

[43] S. Flach, C. R. Willis, and E. Olbrich, *Integrability and localized excitations in nonlinear discrete systems*, Phys. Rev. E, 49 (1994), p. 836.

[44] S. Flach, O. Yevtushenko, and Y. Zolotaryuk, *Directed current due to broken time-space symmetry*, Phys. Rev. Lett., 84 (2000), p. 2358.

[45] S. Flach, Y. Zolotaryuk, A. E. Miroshnichenko, and M. V. Fistul, *Broken symmetries and directed collective energy transport*, Phys. Rev. Lett., 88 (2002), p. 184101.

[46] J. W. Fleischer, M. Segev, N. K. Efremidis, and D. N. Christodoulides, *Observation of two-dimensional discrete solitons in optically induced nonlinear photonic lattices*, Nature, 422 (2003), p. 147.

[47] J. W. Fleisher, T. Carmon, and M. Segev, *Observation of discrete solitons in ooptically induced real time waveguide array*, Phys. Rev. Lett., 90 (2003), p. 023902.

[48] V. Fleurov, R. Schilling, and S. Flach, *Tunneling of a quantum breather in a one-dimensional chain*, Phys. Rev. E, 58 (1998), p. 339.

[49] L. M. Floria, J. L. Marin, P. J. Martinez, F. Falo, and S. Aubry, *Intrinsic localisation in the dynamics of a josephson junction ladder*, Europhys. Lett., 36 (1996), p. 539.

[50] K. Forinash, M. Peyrard, and B. Malomed, *Interaction of discrete breathes with impurity modes*, Phys. Rev. E, 49 (1994), p. 3400.

[51] O. Gendelman and A. Savin, *Normal heat conductivity of the one-dimensional lattice with periodic potential of nearest-neighbor interaction*, Phys. Rev. Lett., 84 (2000), p. 2381.

[52] R. T. Giles and F. V. Kusmartsev, *Chaotic transient in the switching of rotobreathers*, Phys. Lett. A, 287 (2001), p. 289.

[53] J. Göres, D. Goldhaber-Gordon, S. Heemeyer, M. A. Kastner, H. Shtrikman, D. Mahalu, and U. Meirav, *Fano resonances in electronic transport through a single-electron transistor*, Phys. Rev. B, 62 (2000), p. 2188.

[54] I. S. Gradshteyn and I. M. Ryzhik, *Table of integrals, series, and products*, Acad. Pr., New York, 2000.

[55] G. Grimaldi, G. Filatrella, S. Pace, and U. Gambardella, *Flux distribution and critical currents in a one-dimensional row of a josephson junction square lattice*, Phys. Lett. A, 223 (1996), p. 463.

[56] S. A. Gurvitz and Y. B. Levinson, *Resonant reflection and transmission in a conducting channel with a single impurity*, Phys. Rev. B, 47 (1993), p. 10578.

[57] K. Hallberg, S. Flach, A. E. Miroshnichenko, and M. Titov, *Spin filters with fano dots*, unpublished.

[58] A. C. Hewson, *he Kondo Problem to Heavy Fermions*, Cambridge University Press, Cambridge UK, 1993.

[59] T. Iizuka, H. Amie, T. Hasegawa, and C. Matsuoka, *Numerical studies on scattering of the nls soliton due to an impurity*, Phys. Lett. A, 220 (1996), p. 97.

[60] T. Iizuka and M. Wadati, *Scattering of envelope solitons by a nass impurity in nonlinear lattices*, J. Phys. Soc. Jpn, 61 (1992), p. 4244.

[61] G. James, *Centre manifold reduction for quasilinear discrete systems*, J. Nonlinear Sci., 13 (2003), p. 27.

[62] G. James and P. Nobel, *Breathers on diatomic FPU chains with arbitrary masses*, preprint, University of Toulouse, 2002.

[63] F. Jülicher, A. Ajdari, and J. Prost, *Modelling molecular motors*, Rev. Mod. Phys., 69 (1997), p. 1269.

[64] G. Kalosakas, K. O. Rasmussen, and A. R. Bishop, *Delocalizing transition of the bose-einstein condensates in optical lattices*, Phys. Rev. Lett., 89 (2002), p. 030402.

[65] K. Kang, S. Y. Cho, J. J. Kim, and S. C. Shin, *Anti-kondo resonance in transport through a quantum wire with a side-coupled quantum dot*, Phys. Rev. B, 63 (2001), p. 113304.

[66] C. S. Kim and A. M. Satanin, *Coherent resonant transmission in temporally periodically driven potential wells: the fano mirror*, J.Phys.: Condens. Matter, 10 (1998), p. 10587.

[67] S. Kim, C. Baesens, and R. S. MacKay, *Phonon scattering by localized equilibria of nonlinear nearest-neighbor chain*, Phys. Rev. E, 56 (1997), p. R4955.

[68] S. W. Kim and S. Kim, *The structure of eigenmodes and phonon scattering by discrete breathers in the discrete nonlinear schrödinger chain*, Physica D, 141 (2000), p. 91.

[69] S. W. Kim and S. Kim, *Fano resonances in translationally invariant nonlinear chains*, Phys. Rev. B, 63 (2001), p. 212301.

[70] Y. S. Kivshar and B. A. Malomed, *Dynamics of solitons in nearly integrable systems*, Rev. Mod. Phys., 61 (1989), p. 763.

[71] G. Kopidakis, S. Aubry, and G. P. Tsironis, *Targeted energy transfer through discrete breathers in nonlinear systems*, Phys. Rev. Lett., 87 (2001), p. 165501.

[72] S. Lepri, R. Livi, and A. Politi, *Heat conduction in chains of nonlinear oscillators*, Phys. Rev. Lett., 78 (1997), p. 1896.

[73] S. Lepri and R. Livi and A. Politi, *On the anomalous thermal conductivity of one-dimensional lattices*, Europhys. Lett., 43 (1998), p. 271.

[74] W. Li and L. E. Reichl, *Floquet scattering a time-periodic potential*, Phys. Rev. B, 60 (1999), p. 15732.

[75] K. K. Likharev, *Dynamics of Josephson Junctions and Circuits*, Gordon and Breach, New York, 1986.

[76] R. Livi, M. Spicci, and R. S. MacKay, *Breathers on a diatomic fpu chain*, Nonlinearity, 10 (1997), p. 1421.

[77] R. S. MacKay and S. Aubry, *Proof of existence of breathers for time-reversible or hamiltonian networks of weakly coupled oscillators*, Nonlinearity, 7 (1994), p. 1623.

[78] R. S. MacKay and J. A. Sepulchre, *Stability of discrete breathers*, Physica D, 119 (1998), p. 148.

[79] R. S. MacKay and J. A. Sepulchre, *Effective hamiltonian for travelling discrete breathers*, J Phys. A Math. Gen., 35 (2002), p. 3985.

[80] G. D. Mahan, *Many-particle physics*, New York, Plenum Press, 1993.

[81] D. Mandelik, H. S. Eisenberg, Y. Silberberg, R. Morandotti, and J. S. Aitchison, *Observation of mutually trapped multiband optical breather in waveguide arrays*, Phys. Rev. Lett., 90 (2003), p. 253902.

[82] J. L. Marin and S. Aubry, *Breathers in nonlinear lattices: numerical calculation from the anticontinuous limit*, Nonlinearity, 9 (1996), p. 1501.

[83] J. L. Marin and S. Aubry, *Finite size effects on instabilities of discrete breathers*, Physica D, 119 (1998), p. 163.

[84] J. L. Marin, S. Aubry, and L. M. Floria, *Intrinsic localized modes: Discrete breathers. existence and linear stability*, Physica D, 113 (1998), p. 283.

[85] J. L. Marin, F. Falo, P. J. Martinez, and L. M. Floria, *Discrete breathers in dissipative lattices*, Phys. Rev. E, 63 (2001), p. 066603.

[86] D. F. Martinez and L. E. Reichl, *Transmission properties of the oscillating δ-function potential*, Phys. Rev. B, 64 (2001), p. 245315.

[87] P. J. Martinez, L. M. Floria, J. L. Marin, S. Aubry, and J. J. Mazo, *Floquet stability of discrete breathers in anisotropic josephson junction ladders*, Physica D, 119 (1998), p. 175.

[88] A. E. Miroshnichenko, S. Flach, M. V. Fistul, Y. Zolotaryuk, and J. B. Page, *Brearhers in josephson junction ladders: resonances and electromagnetic waves spectroscopy*, Phys. Rev. E, 64 (2001), 066601.

[89] A. E. Miroshnichenko, S. Flach, and B. Malomed, *Resonant scattering of solitons*, Chaos, 13 (2003), p. 874.

[90] P. M. Morse and H. Feshbach, *Methods of Theoretical Physics*, McGraw-Hill, New York, 1953.

[91] P. Müller and A. V. Ustinov, *The physics of superconductors*, Springer, Berlin, 1997.

[92] J. U. Nöckel and A. D. Stone, *Resonances line shapes in quasi-one-dimensional scattering*, Phys. Rev. B, 50 (1994), p. 17415.

[93] M. Peyrard, *The pathway to energy localization in nonlinear lattices*, Physica D, 119 (1998), p. 184.

[94] F. Pignatelli and A. V. Ustinov, *Observation of breather-like states in a single josephson cell*, Phys.Rev. E, 67 (2003), p. 036607.

[95] P. J. Price, *Transmission and reflection peaks in multichannel ballistic transport*, Phys. Rev. B, 48 (1993), p. 17301.

[96] P. Reimann, *Brownian motors: noisy transport far from equilibrium*, Phys. Rep., 361 (2002), p. 57.

[97] M. Salerno and Y. Zolotaryuk, *Soliton ratchetlike dynamics by ac foces with harmonic mixing*, Phys. Rev. E, 65 (2002), p. 056603.

[98] M. Sato, B. E. Hubbard, A. J. Sieverse, B. Ilic, D. A. Czaplewski, and H. G. Craighead, *Observation of locked intrinsic localized vibrational modes in a micromechanical oscillator array*, Phys. Rev. Lett., 90 (2003), p. 044102.

[99] A. V. Savin and O. V. Gendelman, *On the finite thermal conductivity of a one-dimensional rotator lattice*, Phys. Solid State, 43 (2001), p. 355.

[100] A. V. Savin and L. I. Manevitch, *Discrete breathers in a polyethylene chain*, Phys. Rev. B, 67 (2003), p. 144302.

[101] D. Schmeltzer, A. R. Bishop, A. Saxena, and D. L. Smith, *Spin-polarized conductance induced by tunneling through a magnetic impurity*, Phys. Rev. Lett., 90 (2003), p. 116802.

[102] M. Schuster, P. Binder, and A. V. Ustinov, *Observation of breather resonances in josephson ladders*, Phys. Rev. E, 65 (2002), p. 016606.

[103] U. T. Schwarz, L. Q. English, and A. Sievers, *Experimental generation and observation of intrinsic localized spin wave modes in an antiferromagnet*, Phys. Rev. Lett., 83 (1999), p. 223.

[104] A. C. Scott, J. C. Eilbeck, and H. Gilhoj, *Quantum-lattice solitons*, Physica D, 78 (1994), p. 194.

[105] J. A. Sepulchre and R. S. MacKay, *Localized oscillations in conservative or dissipative networks of weakly coupled autonomous oscillators*, Nonlinearity, 10 (1997), p. 679.

[106] A. Sievers and J. Page, *Dynamical Properties of Solids VII Phonon Physics*, Elseiver, Amsterdam, 1995.

[107] S. Strogatz, *Nonlinear Dynamics and Chaos: with Applications to Physics, Biology, Chemistry and Engineering*, Addison-Wesley, Reading, MA, 1994.

[108] B. Swanson, J. Brozik, S. Love, G. Strouse, A. Shreve, A. Bishop, W. Z. Wang, and M. Salkola, *Observation of intrinsically localized modes in a discrete low-dimensional material*, Phys. Rev. Lett., 82 (1999), p. 3288.

[109] M. Switkes, C. M. Marcus, K. Campman, and A. C. Gossard, *An adiabatic quantum electronic pump*, Science, 283 (1999), p. 1905.

[110] S. Takeno and M. Peyrard, *Nonlinear modes in coupled rotator models*, Physica D, 92 (1996), p. 140.

[111] E. Tekman and P. F. Bagwell, *Fano resonances in quasi-one-dimensional electron waveguuides*, Phys. Rev. B, 48 (1993), p. 2553.

[112] P. Tong, B. Li, and B. Hu, *Wave transmission, phonon localization, and heat conduction of a one-dimensional frenkel-kontorova chain*, Phys. Rev. B, 59 (1999), p. 8639.

[113] M. E. Torio, K. Hallberg, A. H. Ceccatto, and C. R. Proetto, *Kondo resonances and fano antiresonances in transport through quantum dots*, Phys. Rev. B, 65 (2002), p. 085302.

[114] E. Trias, J. J. Mazo, A. Brinkman, and T. P. Orlando, *Discrete breaters in josephson ladders*, Physica D, 156 (2001), p. 98.

[115] E. Trias, J. J. Mazo, and T. P. Orlando, *Discrete breathers in nonlinear lattices: experimental detection in a josephson array*, Phys. Rev. Lett., 84 (2000), p. 741.

[116] A. Trombettoni and A. Smerzi, *Discrete solitons and breathers with bose-einstein condensates*, Phys. Rev. Lett., 86 (2001), p. 2353.

[117] G. P. Tsironis and S. Aubry, *Slow relaxation phenomena induced by breathers in nonlinear lattices*, Phys. Rev. Lett., 77 (1996), p. 5225.

[118] S. Watanabe, H. S. J. van der Zant, S. H. Strogatz, and T. P. Orlando, *Dynamics of circular arrays of josephson junctions and the discrete sine-gordon equation*, Physica D, 97 (1996), p. 429.

[119] S. Yamada, T. Kikutani, N. Aoki, H. Hori, and G. Tatara, *Magnetic domain dependent quantum transport through a ferromagnetic dot embedded in a semiconductor quantum wire*, Phys. Rev. Lett., 81 (1998), p. 5422.

Acknowledgements

First of all, I am grateful to Prof. Peter Fulde, the founding director of the Max Planck Institute for the Physics of Complex Systems. In this wonderful place I had the opportunities to meet virtually and actually many famous physicists.

I would like to express my sincere appreciation to my supervisor Dr. Sergej Flach for his wise guidance. By using his astuteness, he was almost always right during hot discussions inside our group and it was very instructive to take part in or even observe them from outside.

I want to thank Mikhail Fistul, Yaroslav Zolotaryuk, Jerome Dorignac, Alexander A. Ovchinnikov and Abdelhadi Benabdallah for a friendly atmosphere in our team and fruitful discussions.

Part of this work has been done in a closed collaboration with the experimental group from Erlangen. Prof. Alexey Ustinov, Marcus Schuster and Francesca Pignatelli deserve a special thank for providing us target setting and experimental data. A much exciting process was the reaching of a consensus on explanation and comparison of numerical and experimental data.

Prof. Victor Fleurov, Prof. Konstantin Kikoin and Prof. Boris Malomed are gratefully thanked for their valuable remarks.

Due to the European Union network 'LOCNET', I had occasions to be acquainted with Prof. Robert MacKay, Prof. Serge Aubry, Prof. Michal Peyrard, Prof. George Tsironis, Prof. Mario Floria and many others , who are the experts in the topic of this work. Discussions with them stimulated my scientific researches.

The financial support for this work has been provided by the Deutsche Forschungsgemeinschaft FL200/8-1.

This work would not be done without support of my wife. In spite of my usual absence, she has gifted to me a second son. I am very grateful to her.

Versicherung

Hiermit versichere ich, daß ich die vorliegende Arbeit ohne unzulässige Hilfe Dritter und ohne Benutztung anderer als der angegebenen Hilfsmittel angefertigt habe; die aus fremden Quellen direkt oder indirekt übernommenen Gedanken sind als solche kenntlich gemacht. Die Arbeit wurde bisher werder im Inland noch in Ausland in gleicher oder ähnlicher Form einer anderen Prüfungsbehörde vorgelegt.

Diese Arbeit wurde unter der Betreuung von Herrn Priv.-Doz. Dr. Sergej Flach am Max-Planck-Institut für Physik komplexer Systeme, Dresden, angefertigt. Die Promotionsordnung der Technischen Universität Dresden wird anerkannt.

Dresden, 2.07.2003.